

**DISPERSION-MANAGED BREATHING-MODE
SEMICONDUCTOR MODE-LOCKED RING LASER: EXPERIMENTAL STUDY,
NUMERICAL SIMULATIONS AND APPLICATIONS**

by

BOJAN RESAN
B.C. University of Zagreb, Croatia, 1997
M.S. Ecole Nationale Supérieure de Physique de Strasbourg, France, 1998
M.S. University of Central Florida, 2001

A dissertation submitted in partial fulfillment of the requirements
for the degree of Doctor of Philosophy
in the College of Optics and Photonics / CREOL & FPCE
at the University of Central Florida
Orlando, Florida

Fall Term
2004

Major Professor: Peter J. Delfyett, Jr.

© 2004 Bojan Resan

ABSTRACT

A novel dispersion-managed breathing-mode semiconductor mode-locked ring laser is developed. The “breathing-mode” designation derives from the fact that intracavity pulses are alternately stretched and compressed as they circulate around the ring resonator. The pulses are stretched before entering the semiconductor gain medium to minimize the detrimental strong integrating self-phase modulation and to enable efficient pulse amplification. Subsequently compressed pulses facilitate bleaching the semiconductor saturable absorber. The intracavity pulse compression ratio is higher than 50. Down chirping when compared to up chirping allows broader mode-locked spectra and shorter pulse generation owing to temporal and spectral semiconductor gain dynamics. Pulses as short as 185 fs, with a peak power of ~230 W, and a focused intensity of ~4.6 GW/cm² are generated by linear down chirp compensation and characterized by SHG-FROG method. To our knowledge, this is the highest peak power and the shortest pulse generation from an electrically pumped all-semiconductor system. The very good agreement between the simulated and the measured results verifies our understanding and ability to control the physical mechanisms involved in the pulse shaping within the ring cavity. Application trends such as continuum generation via a photonic crystal fiber, two-photon fluorescence imaging, and ultrafast pulse source for pump-probe experiments are demonstrated.

ACKNOWLEDGMENTS

I would like to express my deepest gratitude to my advisor Prof. Peter J. Delfyett, Jr. for his great support, wise advices and guidance. His spirit and stimulating scientific remarks kept on inspiring me throughout our research.

It was a great pleasure to be part of the Ultrafast Photonics Group at CREOL. I enjoyed working with my lab-coworker Luis Archundia-Berra including numerous passionate discussions and continuous exchange of ideas. I am thankful to Sangyoun Gee and Chris DePriest for many helpful instructions, group members Kyungbum Kim, Robert Stegeman, Erica Wells, Shinwook Lee, Myoung-Taek Choi, Wangkuen Lee, Franklyn Quinlan, Sarper Ozharar, Hossein Izadpanah, and Ji-Myoung Kim, and alumni Mike Mielke, Tolga Yilmaz, Jennifer Evans, and Eric Park for a friendly collaborative atmosphere.

Thanks to many CREOL friends and overall CREOL as a very good organized College with excellent faculty and staff, a wonderful working atmosphere is created enabling a successful research.

I am sincerely grateful to Profs. George I. Stegeman, Patrick L. LiKamWa, and Alfons Schulte, members of my Dissertation Committee, for their interest, efforts and suggestions for the dissertation improvement.

To my parents *Ana* and *Dušan*, brother *Gordan* and wife *Mirna*

TABLE OF CONTENTS

LIST OF TABLES	viii
LIST OF FIGURES	ix
CHAPTER 1: INTRODUCTION	1
1.1. Motivation and previous work review	1
1.2. Dissertation goals and overview	4
CHAPTER 2: PHYSICAL AND MATHEMATICAL CONCEPTS INVOLVED IN THE ULTRAFAST PULSE GENERATION, PROPAGATION AND CHARACTERIZATION	7
2.1. Definitions	7
2.2. Physical effects defining mode locking and pulse shaping	9
2.3. Ultrafast pulse measurement techniques	12
CHAPTER 3: EXPERIMENTAL CHARACTERIZATION OF THE LASER WORKING REGIME AND INTRACAVITY PULSE PROPAGATION	17
3.1. Mode locking elements: the SOA and the SA	17
3.2. Typical CW and nondispersion-managed mode-locking laser operation.....	22
3.3. Intracavity dispersion management and breathing mode laser operation	27
CHAPTER 4: NUMERICAL SIMULATIONS OF THE DISPERSION-MANAGED BREATHING-MODE SEMICONDUCTOR MODE-LOCKED RING LASER.....	40
4.1. Explanation of numerical simulations algorithm and parameters.....	40
4.2. Laser mode locking build-up	45
4.3. Injection locking of the ring laser	50
CHAPTER 5: THE PROPER CHOISE OF CHIRPING AND EXTERNAL CAVITY COMPRESSION TO PULSE DURATION OF 185 FS.....	52
5.1. External compression of up-chirped pulses down to bandwidth limit	52
5.2. Preference for down chirping owing to the spectral and temporal pulse shaping	55
5.3. FROG measured 185 fs pulses from down-chirped dispersion-managed breathing-mode ring laser	59
5.4. Numerical simulations of the pulse generation by down chirping of the dispersion- managed breathing-mode semiconductor ring laser	65

CHAPTER 6: APPLICATION TRENDS.....	71
6.1. Continuum generation via photonic crystal fiber.....	71
6.2. Two-photon fluorescence imaging.....	78
6.3. Ultrashort pulse source for pump-probe experiments	81
CHAPTER 7: CONCLUSION AND FUTURE WORK SUGGESTIONS.....	86
7.1. Summary and conclusion of the dissertation	86
7.2. Discussion of future possibilities	89
APPENDIX A: THE COMPUTER CODE FOR NUMERICAL SIMULATIONS OF THE UP-CHIRPED DISPERSION-MANAGED BREATHING-MODE SEMICONDUCTOR RING LASER MODE LOCKING BUILDUP (Mathcad)	97
APPENDIX B: THE COMPUTER CODE FOR NUMERICAL SIMULATIONS OF THE UP-CHIRPED DISPERSION-MANAGED BREATHING-MODE SEMICONDUCTOR RING LASER LOCKING UP TO EXTERNALLY INJECTED GAUSSIAN PULSES (Mathcad) ...	105
APPENDIX C: THE COMPUTER CODE FOR CALCULATION OF THE PULSE BANDWIDTH-LIMITED AUTOCORRELATION FROM A MEASURED OPTICAL POWER SPECTRUM (Mathcad)	112
LIST OF REFERENCES	115

LIST OF TABLES

Table 1: List of parameters used for simulations of the dispersion-managed breathing-mode mode-locked semiconductor ring laser.....	44
Table 2: Important properties of the PCF used for continuum generation.	74

LIST OF FIGURES

Figure 1: Comparison of the ultrafast laser families.....	2
Figure 2: Self-phase modulation due to integrating nonlinearity in semiconductors.....	11
Figure 3: Setup for second-harmonic generation (a) intensity autocorrelation and (b) frequency-resolved optical gating (FROG).....	13
Figure 4: Schematic of a generic FROG algorithm.....	16
Figure 5: Structure of the SOA device emitting around 830 nm.....	17
Figure 6: The SOA spontaneous emission spectrum.....	19
Figure 7: The power versus driving current (L-I curve) of the SOA spontaneous emission.....	19
Figure 8: The SOA spontaneous emission reflected from the SA shows the wavelength position of the excitonic saturable absorption band.....	20
Figure 9: Three types of semiconductor laser mode locking: (a) active, (b) passive, and (c) hybrid.....	22
Figure 10: Setup for CW or mode-locked operation of the external-cavity semiconductor ring laser without dispersion management.....	24
Figure 11: L-I curve of the CW operating external-cavity semiconductor ring laser.....	25
Figure 12: Typical output spectrum for passively mode-locked laser without dispersion management.....	26
Figure 13: Typical output pulse second-harmonic intensity autocorrelation for passively mode-locked laser without dispersion management.....	27
Figure 14: Experimental layout of (bottom) dispersion-managed mode-locked semiconductor σ -ring cavity laser and (top) diagnostics.....	28

Figure 15: Geometrical sketch of the double-pass grating-pair dispersion compensator acting as a compressor or stretcher.....	28
Figure 16: Spectral changes when dispersion introduced by element 1 is varied and dispersion introduced by element 2 is constant.....	31
Figure 17: Laser output pulse second-harmonic autocorrelation FWHM versus introduced dispersions by element 1 and 2.....	32
Figure 18: Laser output spectral FWHM versus introduced dispersions by element 1 and 2.....	33
Figure 19: Hybirdly mode-locked sigma cavity semiconductor laser (bottom) with 4 outputs for pulse evolution characterization and (top) diagnostics	34
Figure 20: Optical power spectra: (a) after the gain media, (b) before the SA, (c) after the SA, and (d) before the gain media. Experimental error is 0.2 nm	35
Figure 21: Principle of the pulse temporal intensity profile measurement via two-pulse intensity autocorrelation – sampling of a broad pulse with a much narrower one.	36
Figure 22: Crosscorrelation traces from the four key cavity points: pulses (a) after the cavity gain element, (b) before the SA, (c) after the SA, and (d) before the gain element.	38
Figure 23: Algorithm for dispersion-managed mode-locked ring laser simulations.....	42
Figure 24: Normalized laser output pulse after the gain media and temporal filter with FWHM = 131 ps.	42
Figure 25: Normalized laser output pulse spectrum after the gain media and spectral filter with FWHM = 7.6 nm.....	43
Figure 26: Build-up of the mode-locked stretched pulse temporal intensity profile after the gain media from random noise input.	46
Figure 27: Formation of the mode-locked stretched pulse spectral profile after the gain media. 46	
Figure 28: Mode-locked spectrum evolution of the intracavity compressed pulse after the SA. 47	
Figure 29: Comparison of (dashed) simulated and (solid) measured (a) stretched pulse spectrum after the SOA, and (b) compressed pulse spectrum after the SA.....	48
Figure 30: Comparison of (dashed) simulated and (solid) measured stretched pulse temporal intensity profile after the SOA.....	48
Figure 31: Comparison of (dashed) simulated and (solid) measured compressed pulse temporal intensity profile after the SA.....	49

Figure 32: Locking-up of the laser stretched pulses after the SOA to the external-cavity injected Gaussian pulses.....	51
Figure 33: Comparison of the bandwidth-limited calculated (dashed) and the measured (solid) autocorrelations of the externally compressed up-chirped output pulses after the intracavity SOA.....	53
Figure 34: PICASO retrieved temporal intensity (FWHM = 274 fs) and phase of the externally compressed up-chirped output pulses after the intracavity gain element.....	54
Figure 35: The wavelength position of the SOA spontaneous emission spectrum, the SA excitonic absorption band and a mode-locked laser spectrum.	56
Figure 36: Illustration of the SOA temporal and spectral response to the incident up- and down-chirped pulses.	56
Figure 37: Externally compressed pulse autocorrelation and spectral FWHM versus introduced dispersion by element 2 along the map diagonal.	58
Figure 38: The experimental setup of (bottom) hybridly mode-locked dispersion-managed breathing-mode semiconductor ring laser and (top) diagnostics with additional RF-modulated external SOA and SHG-FROG pulse characterization.	59
Figure 39: Comparison of the measured (solid line) and calculated bandwidth-limited (dashed) autocorrelation from the externally compressed down-chirped laser output pulse.	61
Figure 40: The measured compressed down-chirped laser (solid) spectrum and (dashed) FROG retrieved spectral phase.	62
Figure 41: The measured autocorrelation from the externally compressed down-chirped laser output pulse in log-scale demonstrating SNR of 20 dBs.....	63
Figure 42: The SHG-FROG (left) experimentally measured and (right) retrieved trace. The FROG error was 0.006 with 128x128 grid size.	64
Figure 43: The SHG-FROG retrieved pulse (solid) temporal intensity of FWHM = 185 fs and (dashed) corresponding phase.....	64
Figure 44: The simulated (solid) spectral filter of FWHM = 13.4 nm and (dashed) the normalized steady-state output pulse spectrum after the gain media.....	66
Figure 45: Simulated formation of the mode-locked stretched pulse spectral profile after the gain media in the down chirping regime of the breathing mode.....	67

Figure 46: Comparison of (solid) the simulated and (dashed) the measured stretched pulse spectrum after the SOA	68
Figure 47: Comparison of (dashed) the simulated and (solid) the FROG retrieved compressed pulse temporal intensity.....	69
Figure 48: Experimental setup for supercontinuum generation and detection. DMBM laser – dispersion-managed breathing-mode laser, PCF – photonic crystal fiber, and OSA – optical spectrum analyzer.	73
Figure 49: The SEM image of the PCF cross-section.....	73
Figure 50: Laser output spectrum after amplification and compression, incident to the PCF....	75
Figure 51: The autocorrelation of the compressed laser output pulse incident to the PCF.	75
Figure 52: Comparison of the laser pulse spectra before and after 1 m long PCF.....	77
Figure 53: Comparison of the laser pulse spectra before and after 26 m long PCF.	77
Figure 54: Schematic of the experimental setup for two-photon fluorescence observation.	79
Figure 55: The chemical structure of the organic dye sample.	80
Figure 56: Photograph of the two-photon fluorescence from the organic dye sample. The right photograph is zoomed out part with the blue light from the left photograph.....	81
Figure 57: The experimental layout of the pump-probe experiment studying the SOA gain dynamics for input ultrafast multiwavelength pulses.....	83
Figure 58: The fs-scale time resolved gain dynamics of the SOA amplifying multiwavelength ultrafast pulses.	84
Figure 59: The adaptive feedback pulse recompression from a continuum generated via the PCF and the dispersion-managed mode-locked semiconductor laser system.	90
Figure 60: The fiberized version of the dispersion-managed breathing-mode semiconductor mode-locked ring laser. CFBG – chirped fiber Bragg grating; PCF – photonic crystal fiber.	93
Figure 61: The fiberized version of the dispersion-managed breathing-mode semiconductor mode-locked ring laser employing one CFBG operating in the reflection mode. OI - optical isolator.	93

CHAPTER 1: INTRODUCTION

1.1. Motivation and previous work review

Many types of laser systems producing pulses in the femtosecond time scale, referred as ultrafast lasers, have been developed since the early 1970's. Currently, ultrafast lasers can be divided in three main families: solid-state, fiber, and diode laser systems, as illustrated in the Figure 1. Solid-state laser systems by far outperform any other laser system in terms of the shortest duration and highest peak power pulse generation, reaching TW peak power and less than 3 fs or even recently attosecond pulse durations. They consist of diode lasers pumping Nd:YAG laser which pumps finally laser crystal, usually Ti:Sapphire. The two-step pumping process results in physical dimension of a few meters in size and costs ranging from 100 to 150 thousands dollars, for commercial ultrafast lasers systems. The physical size and cost make these lasers inappropriate for many commercial applications. The second family is fiber lasers systems, which consists of diode lasers directly pumping the fiber gain media. The elimination of one of the pumping steps significantly decreases the size and cost and increases the overall efficiency. State of the art fiber lasers generate pulses of duration less than 35 fs. Recently, fiber lasers have become commercially available for 60-80 thousands dollars, delivering approximately 100 fs pulses from a “shoe-box” size footprint. Electrically pumped, all-semiconductor laser systems could be defined as the third family as they do not require any

external optical pumping and therefore their overall wall-plug efficiency is theoretically the highest possible. Electrical current is directly injected in the semiconductor media providing optical gain in the laser cavity to generate femtosecond pulses. These lasers can be made in a size comparable to microelectronic chips, since semiconductor media possess large small signal gain. In addition, these lasers can take advantage of the mature semiconductor manufacturing technology that exists today. All-semiconductor electrically pumped ultrafast lasers are not yet commercially available. It is believed that if the technology is sufficiently developed, semiconductor ultrafast lasers could cost a few thousand dollars. In numerous research and industrial applications, there is a need for compact, low-cost, low-noise, high-power, ultrashort pulse sources. Obviously, mode-locked semiconductor lasers are very attractive candidates due to their small size, cost-effectiveness and excellent wall-plug efficiency.

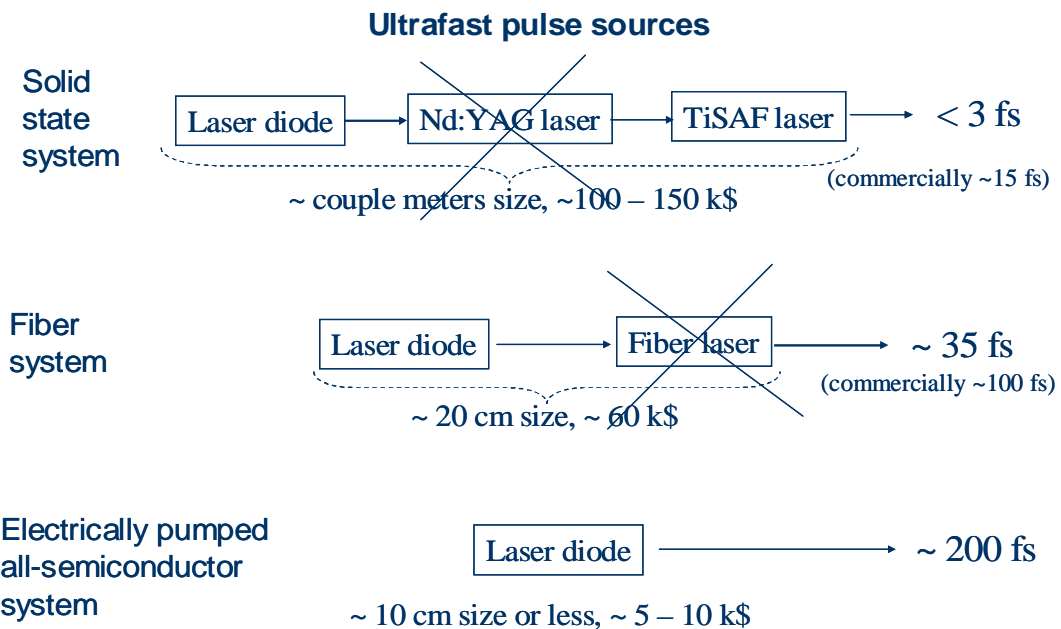


Figure 1: Comparison of the ultrafast laser families.

During the last two decades, extensive effort has been devoted to investigate the ultrafast behavior of semiconductors [1] and semiconductor lasers. Pioneering work with external-cavity semiconductor mode-locked lasers was performed in the mid 1980s [2]. Research in this field is still very active, owing to the various applications including optical signal processing [3], wavelength division multiplexing (WDM), optical time division multiplexing (OTDM) [4], wavelength switching [5], optical clock recovery [6], [7], low-noise, high-bit rate optical sampling [8], optical interconnects [9], [10], frequency metrology [11], biomedical imaging and treatment [12] – [14], material processing, to name a few.

Disadvantages of ultrafast semiconductor lasers such as limited output power and the attainable pulse duration no shorter than few hundred femtoseconds are still obstacles for wider industrial applications. Semiconductor material has high gain, high nonlinearity and actually high integrating self-phase modulation (SPM), compared to instantaneous SPM present in solid-state laser crystals such as Ti:Sapphire or Nd:YAG. Strong integrating SPM in the semiconductor gain media impresses highly nonlinear chirp along the propagating pulse. This impedes efforts to generate pulses compressible to below approximately 500 fs. One approach to overcome this nonlinear chirp is to use a saturable absorber (SA) along with a fixed amount of positive group velocity dispersion (GVD) introduced by intracavity elements [15]. In such a scheme, the pulse is stretched by intracavity GVD and the leading part is absorbed by the SA. The residual pulse contains predominantly linear positive chirp, which can be compensated with an external-cavity compressor providing linear negative chirp. Dispersion management was extensively investigated previously in pulse propagation through fibers [16]-[20] and recently in fiber lasers [21]-[23]. Ultrashort pulse generation from Ti:Sapphire laser has been modeled by

the use of dispersion-managed long-distance nonlinear pulse propagation [24]. An intracavity tunable GVD semiconductor laser was investigated with one dispersion compensation element in one side of the linear external cavity [25]. However, much shorter pulses were reported without intracavity introduced GVD, using linear and nonlinear chirp compensation [26], [27]. Nonlinear chirp compensation is not generally an attractive option for broad adoption in the research and industrial communities owing to the additional complexity required by these techniques.

1.2. Dissertation goals and overview

In this work, we employ an intracavity dispersion management scheme to minimize the detrimental effect of SPM by utilizing a chirped pulse amplification (CPA) concept. Our approach is to use two intracavity tunable GVD elements to adjust the pulse widths appropriately for a SA and a cavity gain element. The pulse is temporally stretched prior to the semiconductor optical amplifier (SOA) as an intracavity gain element in order to decrease SPM as well as extract additional energy. Subsequently, the pulse is compressed to more easily saturate the SA. When the pulse alternately experiences temporal stretching and compression while propagating within the ring cavity, the laser is said to operate in the “breathing mode”. The thesis goal is to develop such a novel, robust ultrafast semiconductor laser that will generate linearly chirped pulses and address both of the main disadvantages of mode-locked semiconductor lasers. Linear chirping minimizes the SPM and therefore pulses are compressible to much shorter durations. Additionally, the generated stretched pulses are much more efficiently amplified inside and outside of the laser cavity.

The second chapter of this dissertation describes the most influential physical and mathematical concepts involved in the pulse generation, propagation and characterization from an ultrafast semiconductor laser. The nonlinear saturable gain and absorption are the key physical effects in the medium to establish mode locking of the laser. Together with dispersion and self-phase modulation they shape the temporal and spectral pulse profile. The intensity autocorrelation, crosscorrelation and spectrogram are shown to be extremely useful mathematical concepts and experimental techniques for pulse characterization and are used by all ultrafast optic researchers worldwide.

Chapter three elucidates the experimental characterization of the laser working regime and intracavity pulse propagation. As the main mode-locking elements, the specific device structure of the SOA and the SA are explained in more detail, including their emission and absorption properties. The CW and mode-locked working regime of a nondispersion-managed semiconductor laser are shown. The dispersion-managed ring laser setup is explained and the laser working regime is investigated with respect to varying introduced dispersions. Spectral and temporal pulse evolution measurements at four key cavity points demonstrate the novel laser operating mode. The concept of the breathing mode of laser operation is identified.

In chapter four numerical simulations of the laser mode locking build-up and laser injection locking are presented. The algorithm of simulations and parameters are discussed and compared with previous works from the literature. Mode locking build-up and injection locking 3D plots are illustrated and the steady state solutions are compared with experimentally measured results.

Chapter five demonstrates the critical nature of the choice of up or down (positive or negative) chirping in the dispersion-managed semiconductor mode-locked ring laser. Up chirped

pulses are externally compressed to within 10% of the bandwidth limit, but the generated spectra are narrow due to the temporal and spectral interplay of the SOA and the SA. On the contrary, down chirping produces optical spectra that are three times broader and pulses as short as 185 fs are achieved. The ultrashort pulses are characterized with the second-harmonic generation frequency-resolved optical gating (SHG-FROG) method.

In chapter six, possible applications of the developed laser are discussed. First, the generated pulse spectrum is coherently broadened by use of photonic crystal fiber (PCF) after an external compression stage. Coherent spectrum of 35 nm is measured after propagation through 26 meters of the PCF. Subsequent amplification of the coherently broadened spectrum by an additional SOA and pulse recompression is discussed. Second, a potential application of two-photon imaging is highlighted. Externally compressed laser pulses are focused in an organic dye sample and two-photon fluorescence is observed. Finally, the laser can be used in other research experiments as a source of ultrashort pulses. For example, it has been used in our lab for a series of pump-probe experiments investigating ultrafast dynamics of multiwavelength semiconductor mode-locked lasers.

The seventh chapter summarizes the experiments, simulations and concludes the dissertation. Some suggestions for future work and possible directions in the field will be discussed. Several appendixes in the end offer additional details about the computer codes used throughout the dissertation.

CHAPTER 2: PHYSICAL AND MATHEMATICAL CONCEPTS INVOLVED IN THE ULTRAFAST PULSE GENERATION, PROPAGATION AND CHARACTERIZATION

2.1. Definitions

In the scalar approximation, the electric field is treated as linearly polarized light simplifying the vector character of any real light. Ignoring additionally the spatial portion of the field, the temporal dependence could be written as:

$$e(t) = \frac{1}{2} \sqrt{I(t)} e^{-i[w_0 t - f(t)]} + c.c. \quad (1)$$

where t is time in the pulse reference frame, w_0 is a carrier angular frequency, and $I(t)$ and $f(t)$ are the time-dependent intensity and phase of the pulse. For our purposes, when the pulse is longer than few fs (electric field oscillates more than few cycles under the pulse envelope), we do not need to carry along the carrier frequency phase term in the calculations. In the standard analytical signal approximation, we could ignore the complex conjugate part, c.c., and write the complex amplitude of the wave as:

$$E(t) = \sqrt{I(t)} e^{if(t)} \quad (2)$$

$E(t)$ is the simplified electric field without the rapidly varying factor with carrier frequency and multiplied by 2. Further it will be used in such form if not specified otherwise.

The pulse field in the frequency domain is the Fourier transform of the time-domain field, $E(t)$:

$$E(w) = \int_{-\infty}^{\infty} E(t) e^{iwt} dt \quad (3)$$

Also, the inverse Fourier transform is:

$$E(t) = \frac{1}{2\pi} \int_{-\infty}^{\infty} E(w) e^{-iwt} dw \quad (4)$$

Thus, the optical spectrum is $S(w) = |E(w)|^2$. The temporal phase, $f(t)$, contains frequency versus time information, and the pulse instantaneous angular frequency is defined as:

$$w_{inst}(t) = w_0 + \frac{df(t)}{dt} \quad (5)$$

Change of the instantaneous angular frequency (second term in Equation 5) is usually referred to as chirp. Similarly, the spectral phase contains time versus frequency information and we define the group delay versus frequency as:

$$t_{group}(w) = -\frac{df(w)}{dw} \quad (6)$$

2.2. Physical effects defining mode locking and pulse shaping

In semiconductor media, for an incident pulse of a few picoseconds in duration or longer, carrier heating and other faster processes on the femtosecond scale may be neglected. From the density matrix approach, one can derive the following expression for the output pulse intensity from a thin nonlinear saturable gain or absorption element [28]:

$$I(t) = I_{in}(t) \frac{e^{\frac{2s}{hw} \int_{-\infty}^t I_{in}(t') dt'}}{e^{-a} - 1 + e^{\frac{2s}{hw} \int_{-\infty}^t I_{in}(t') dt'}} \quad (7)$$

where $I_{in}(t)$ is the incident pulse, $I(t)$ is the pulse after propagation through the medium, s is the interaction (amplification or absorption) cross section and $a = s \Delta g^e z$ is the absorption or amplification coefficient depending on whether the equilibrium population inversion Δg^e is positive or negative. The saturation parameter s gives the ratio of the pulse energy E_p , (not to be

confused with the pulse electric field amplitude) to the saturation energy E_{sat} of the nonlinear element as follows:

$$s = \frac{2s}{\hbar w} \int_{-\infty}^{\infty} I_{in}(t') dt' = \frac{E_P}{E_{sat}} \quad (8)$$

From the wave equation, in the frequency domain one can easily derive the following equation describing the propagation of the pulse through the dispersive media with linear dispersion [28]:

$$E(w, z) = E(w, 0) e^{i \frac{\partial^2 k}{\partial w^2} w^2 z} \quad (9)$$

where E is the amplitude of the pulse spectrum at angular frequency w . The pulse starts to interact with the medium with the GVD parameter $k'' = \frac{\partial^2 k}{\partial w^2}$ at $z = 0$ and acquires a spectral phase while propagating for a length z . Depending on the spectral phase of the input pulse at $z = 0$, the output pulse can experience broadening or shortening in the time domain. GVD can be also expressed in units ps/(nm cm). The transformation relation from the k'' parameter is the following:

$$\frac{\Delta t}{L \Delta I} = 2p \frac{c}{I^2} k'' \quad (10)$$

The integrating nonlinearity in semiconductors causes strong SPM. A light pulse propagating through the semiconductor media varies the carrier density and therefore the index of refraction. The index change increases proportionally to the saturable gain decrease. Thus, the instantaneous frequency variation is proportional to the negative of the pulse intensity profile and is highly dependent on the temporal pulse width [26], [29]. The consequence is nonlinear chirp impressed along the pulse, which is difficult to compensate. The situation is sketched in Figure 2 for the gain impulse response function $h(t)$ that is much slower than a Gaussian input pulse duration of approximately 2 ps.

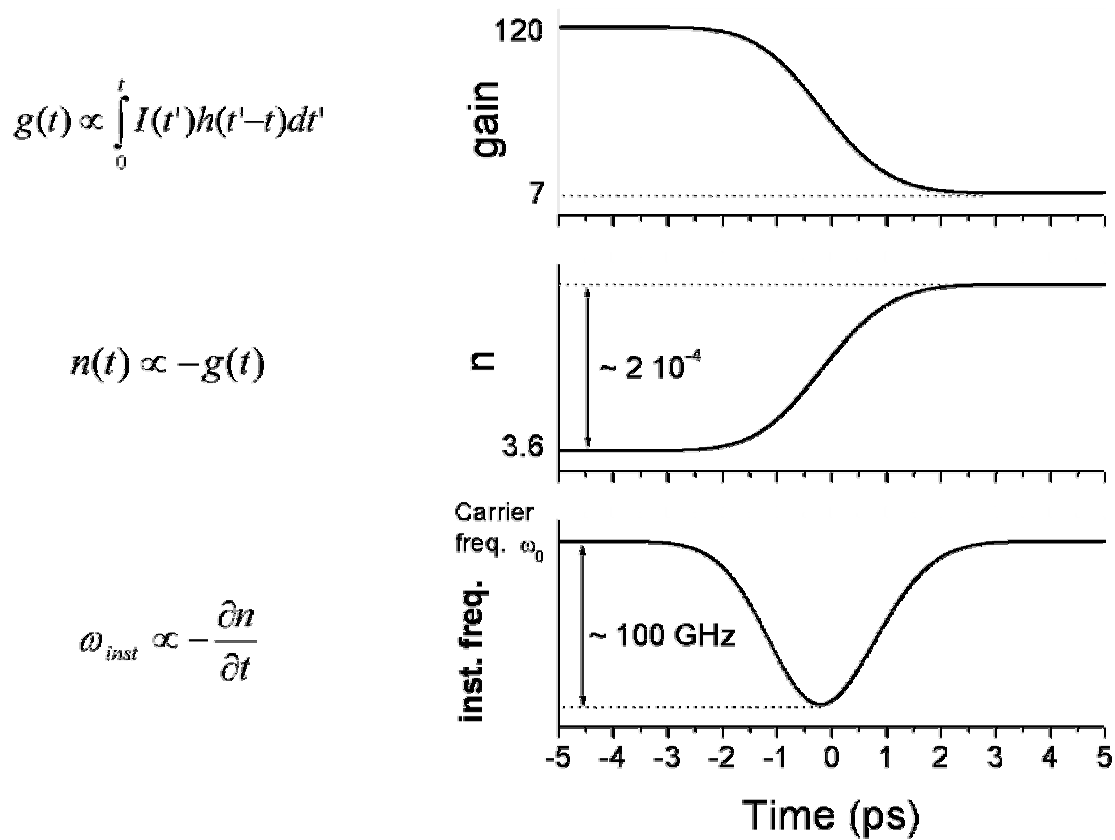


Figure 2: Self-phase modulation due to integrating nonlinearity in semiconductors.

These dynamics can be expressed as:

$$E_{SPM}(t) = E_{in}(t)e^{in_{INT} \int_{-\infty}^t I_{in}(t')dt'} \quad (11)$$

where $E_{in}(t)$ and $I_{in}(t)$ are the input pulse field and intensity, E_{SPM} is the output field with impressed SPM, and n_{INT} is a phenomenologically introduced nonlinear index of refraction (integrating SPM coefficient).

It is important to note that different books, scientific papers and software (like mathcad, matlab, mathematica etc.) use different signs in the definition of the electrical field phase term and the Fourier transformation. There is no unique convention. Therefore, one must be very careful and stick to one definition from the beginning and carry it out through the derivation of the formulae for the dispersion and the self-phase modulation terms in order to avoid misleading conclusions and results.

2.3. Ultrafast pulse measurement techniques

For a long time the puzzling question was how to measure ultrafast laser pulses when they are the fastest phenomena in the nature made by human hands. It is hard to imagine the measurement of something that is faster than anything else. Still, laser scientists came to the conclusion to measure ultrafast pulses by the use of themselves. The concept is to correlate the

ultrafast pulse by itself or some variation of itself. The simplest way is to measure the pulse second-harmonic intensity autocorrelation. The general setup is shown in Figure 3.

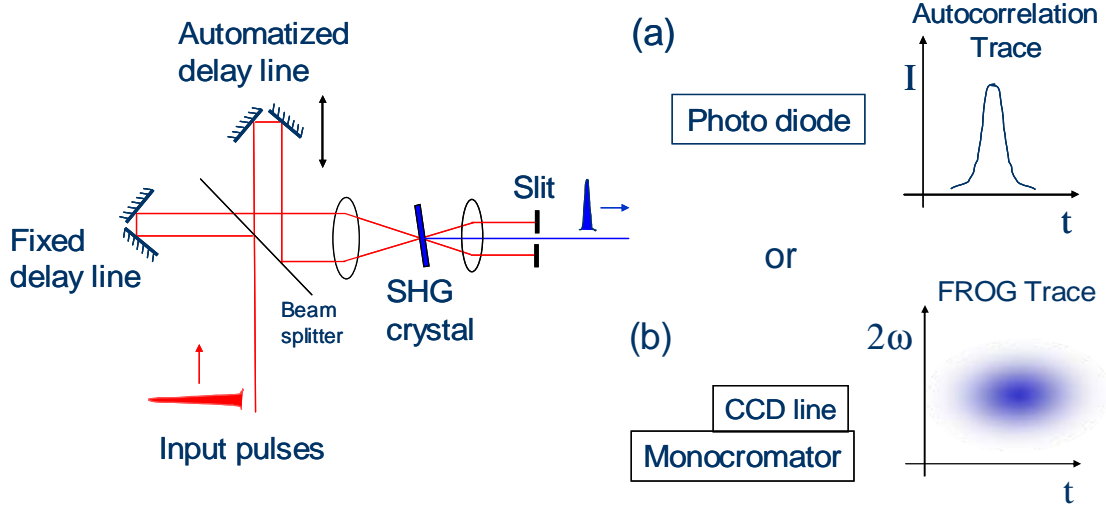


Figure 3: Setup for second-harmonic generation (a) intensity autocorrelation and (b) frequency-resolved optical gating (FROG).

It is basically a Michelson interferometer with the output focused in a second-harmonic generation (SHG) crystal. In our case, the beams are crossed in the crystal, which is usually referred to as the noncollinear, or background free geometry [28]. A SHG crystal will produce a signal at twice the frequency of input light with a field that is given by [30]:

$$E_{sig}^{SHG}(t,t) \propto E(t)E(t-t) \quad (12)$$

where t is the delay time between the interferometer arms and $E(t)$ is the input field. The field has an intensity that is proportional to the product of the intensities of the two input pulses:

$$I_{sig}^{SHG}(t, t) \propto I(t)I(t-t) \quad (13)$$

Since detectors are too slow to resolve $I_{sig}^{SHG}(t, t)$ (even the fastest electronics have approximately a 20 picosecond response time compared to fs pulse durations), the measurement produces the time integral:

$$A(t) \propto \int_{-\infty}^{\infty} I(t)I(t-t)dt \quad (14)$$

Equation (14) is the mathematical definition of the autocorrelation of function $I(t)$. In optics it is referred to as the intensity autocorrelation, to denote the difference from the field autocorrelation. When two different pulses (functions) are correlated, we measure the crosscorrelation:

$$C(t) \propto \int_{-\infty}^{\infty} I_1(t)I_2(t-t)dt \quad (15)$$

In the case that one pulse is much shorter than the other (e.g. compared to $I_2(t)$, $I_1(t)$ approaches the delta function $d(t)$), by means of crosscorrelation, we actually measure the exact temporal profile of the longer pulse $I_2(t)$:

$$C(t) \propto \int_{-\infty}^{\infty} I_1(t) I_2(t-t) dt \approx \int_{-\infty}^{\infty} d(t) I_2(t-t) dt = I_2(t) \quad (16)$$

However, a useful technique for pulse characterization is to measure the spectrogram, known in the ultrafast community as the frequency resolved optical gate or the FROG trace. For the SHG-FROG, the trace is given by [30]:

$$I_{FROG}^{SHG}(w, t) = \left| \int_{-\infty}^{\infty} E(t) E(t-t) e^{-iwt} dt \right|^2 \quad (17)$$

The SGH-FROG trace is essentially spectrally resolved set of intensity autocorrelations. From the measured FROG trace, the FROG pulse retrieval algorithm provides us the unique solution for the ultrafast pulse temporal profile [31], if the measurement is properly performed and there is no excessive noise.

Several FROG pulse-retrieval algorithms exist, and the best possible computer program for pulse retrieval would incorporate all of them, switching from one to another if one stagnates. A common feature of most FROG algorithms is that they are based on the iterative-Fourier-transform algorithm commonly used in phase retrieval problems and schematically shown in Figure 4.

Starting with an initial guess for the field $E(t)$, a signal field $E_{sig}(t, t)$ is generated using Equation (12). This field is then Fourier transformed with respect to t in order to generate the signal field $E_{sig}(w, t)$ in the frequency domain. The measured FROG trace $I_{FROG}(w, t)$ is then used to generate an improved signal field $E'_{sig}(w, t)$.

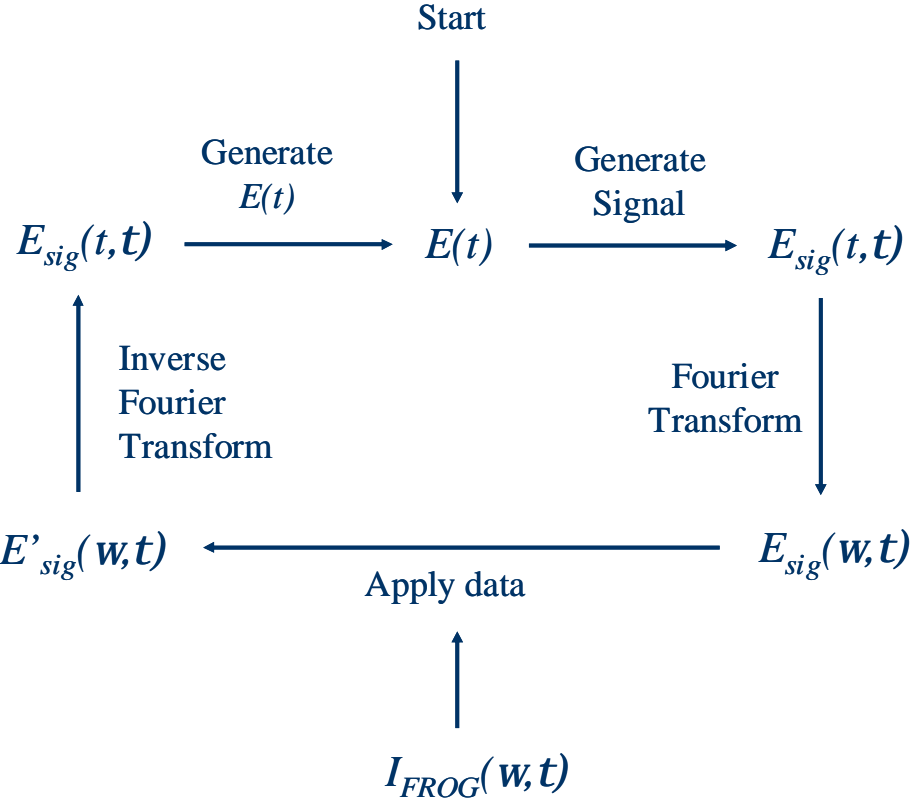


Figure 4: Schematic of a generic FROG algorithm.

Since the squared magnitude of $E_{sig}(w, t)$ should be equal to $I_{FROG}(w, t)$, this step nearly always involves simply replacing the magnitude of $E_{sig}(w, t)$ with the square root of the measured trace to generate $E'_{sig}(w, t)$. $E'_{sig}(w, t)$ is then transformed back into the time domain by applying the inverse Fourier transform. In the last step of the cycle, the modified signal field $E'_{sig}(t, t)$ is used to generate a new guess for $E(t)$ and the process is repeated. Ideally, each iteration of the algorithm generates a better guess, which eventually approaches the correct complex electric field. The most powerful algorithm, commonly used in commercial software is the generalized projections algorithm [30].

CHAPTER 3: EXPERIMENTAL CHARACTERIZATION OF THE LASER WORKING REGIME AND INTRACAVITY PULSE PROPAGATION

3.1. Mode locking elements: the SOA and the SA

External cavity mode-locked semiconductor lasers use diode chips as a laser cavity gain media. Throughout this research a 0.5 mm long, angle-striped and antireflection-coated semiconductor optical amplifier (SOA) was the gain media. The device structure is sketched in Figure 5. The active region is a GaAs/AlGaAs multiple-quantum well (MQW) structure with broadened waveguide design [32] emitting light around 830 nm.

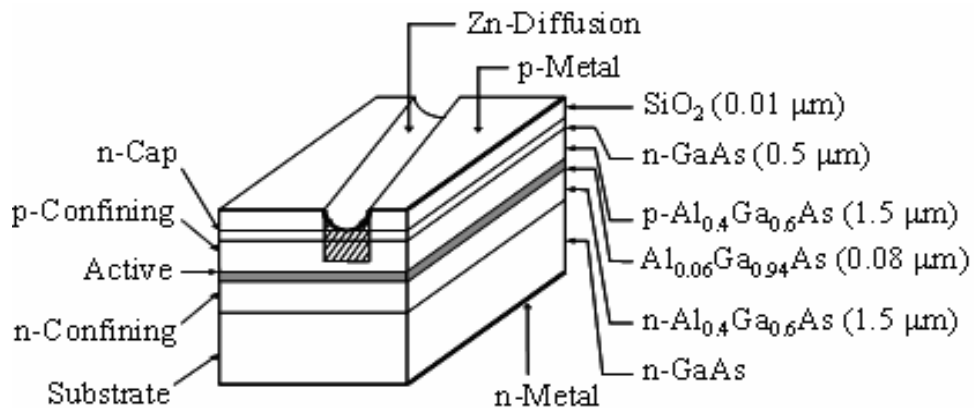


Figure 5: Structure of the SOA device emitting around 830 nm.

The most challenging task in making an SOA from a properly layered semiconductor wafer is suppressing the Fabry-Perot modulation in the output spectrum. Considering the large semiconductor small signal gain, the reflectivity R should be reduced to the order of 10^{-5} , which is a very stringent requirement to achieve with antireflection (AR) coatings. Therefore, in addition to AR coatings, the gain stripe is inclined from the normal to the SOA's emitting facets. Angle striping of approximately 7 degrees minimizes the reflected light from the facet that could be injected back into the active region. Optical wave guiding is enabled by a narrow corridor of gain, produced by current injection adjacent to the positive-contact stripe, within the active region. The stripe width is typically 3 microns in order to provide single transverse spatial mode emission from such a gain-guided device. The device output emitting area is 3 μm wide and 1 μm high causing astigmatism and high divergence in the output beam. Lenses with a numerical aperture of 0.5 and 1 mm working distance (Melles-Griot triplet, model 06GLC002) were used to collimate and refocus the beams. The devices are mounted positive side (p-side) down onto the copper stud maximizing the thermal flow into the heat sink mount.

Figure 6 presents the spontaneous emission spectrum (FWHM = 25 nm) of the 0.5 mm long SOA device. There is no significant Fabry-Perot modulation of the spontaneous emission spectrum. With a high-resolution optical spectrum analyzer (model ANDO AQ6317B, 0.02 nm resolution at 830 nm) a spectral modulation of a few percent is observed, which is within the tolerance for good mode locking.

The output power from both sides of the SOA device versus the injected current is plotted in Figure 7. The power exponentially increases with driving current, as expected.

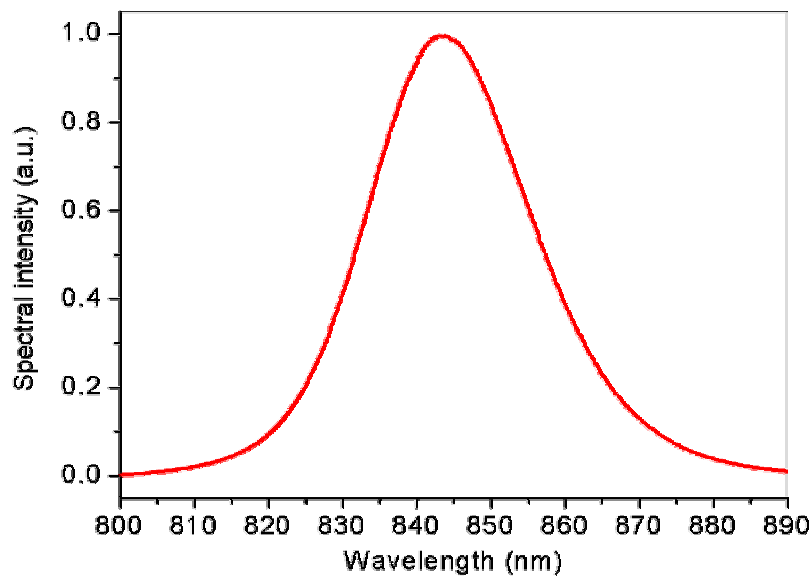


Figure 6: The SOA spontaneous emission spectrum.

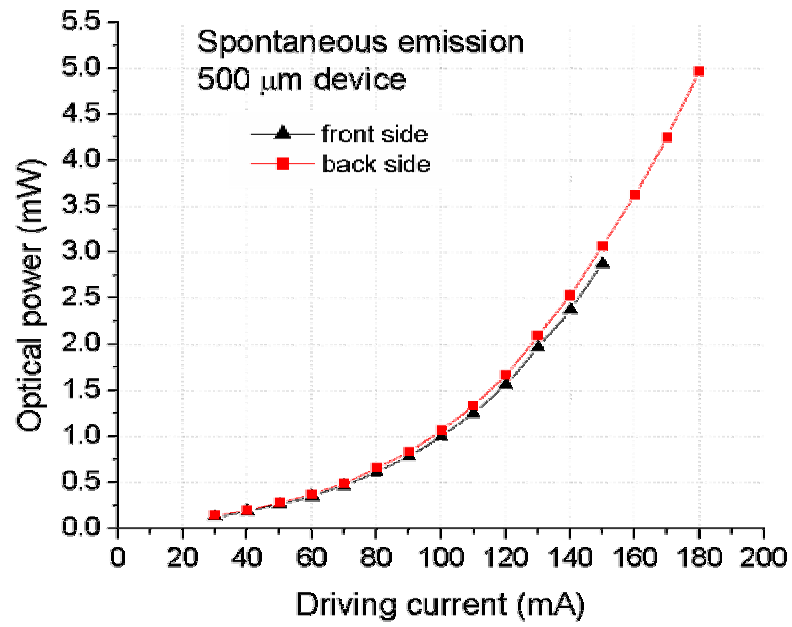


Figure 7: The power versus driving current (L-I curve) of the SOA spontaneous emission.

No observed knee or threshold suggests that coatings are good and the diode does not lase. A small, acceptable difference in the front and back output powers can be attributed to the nonequal AR coatings, nonuniformities in the SOA waveguide region and nonperfect chip mounting and alignment.

The passive mode locking element used throughout this dissertation is a chirped semiconductor saturable absorber mirror (SA). The SA consists of 50 stacks of GaAs quantum wells with chirped thicknesses of 7/7.5/8 nm, separated by 10 nm $\text{Al}_{0.3}\text{Ga}_{0.7}\text{As}$ barriers. The structure was removed from the growth substrate using a standard lift-off process and deposited on the surface of a gold mirror [33], [34]. The SA excitonic saturable absorption band is depicted in Figure 8.

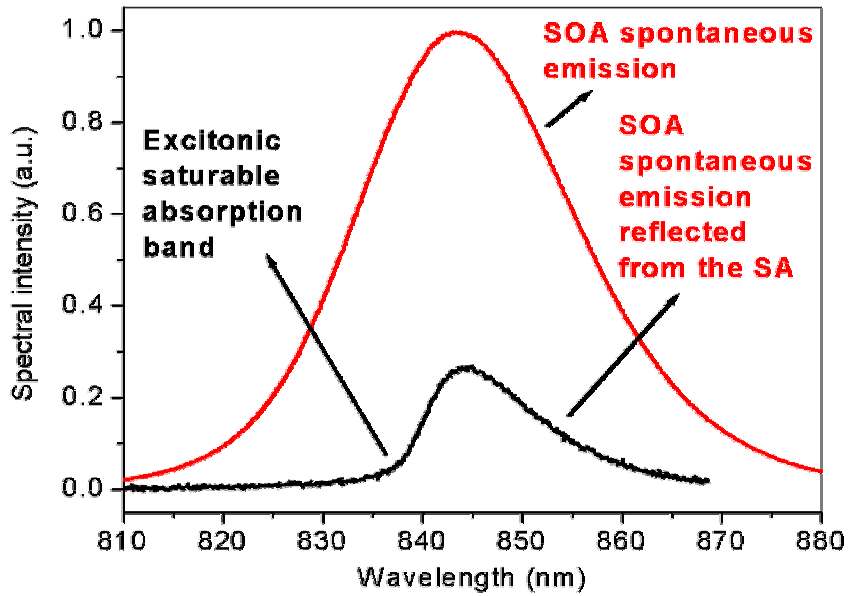


Figure 8: The SOA spontaneous emission reflected from the SA shows the wavelength position of the excitonic saturable absorption band.

Changing or chirping the quantum well thickness from 7 to 8 nm allows for a broader excitonic absorption spectrum, without ripples caused by heavy and light holes absorption [34]. Broad excitonic spectra are crucial to support broad mode-locked laser spectra in efforts to generate ultrashort pulses. The quantum well design enhances excitonic absorption and makes it observable even at room temperatures [35], [36]. In bulk semiconductors, excitons can only be observed at very low temperature, reducing their interest for practical devices. The physical reason why the MQW absorption can saturate more readily is that the saturation is due to the screening of excitons by free carriers – a mechanism qualitatively distinct from the filling of conduction and valence-band states in the GaAs material [33]. In order to achieve the slow saturable absorber mode locking [37], two conditions must be satisfied by the saturable absorber material. The saturation intensity of the saturable absorber must be lower than that of the saturable gain media and the recovery time of the SA must be shorter than that of the gain media. The first condition is accomplished by employing excitonic absorption nonlinearity of MQWs which has approximately 10 times lower saturation intensity than the one required to saturate bulk GaAs, as explained above. The normal recovery time of the excitons is approximately 30 ns compared to the much faster SOA recovery time of approximately 1 ns. Therefore an additional step in the SA fabrication is needed to satisfy the second mode locking condition. When protons bombard a semiconductor material, they create defects in the lattice acting as recombination centers and reducing the recovery time. Generally, higher density of implanted protons decreases the SA recovery time [38]. Protons with 200 keV energy and the density of $10^{13}/\text{cm}^2$, are implanted to reduce the recovery time of the SA used for our experiments to 150 ps [39]. Low temperature growth of the GaAs/AlGaAs MQWs is reported to reduce the SA

recovery time down to 1 ps [40]. In addition, care must be taken to focus the incident beam tight enough to the SA to enable the effect of recovery time reduction via carrier diffusion [33].

3.2. Typical CW and nondispersion-managed mode-locking laser operation

Three types of semiconductor laser mode locking could be distinguished with respect to the performance. Figure 9 illustrates active, passive and hybrid mode locking with the simplest cavities constructed around the SOA, as an example.

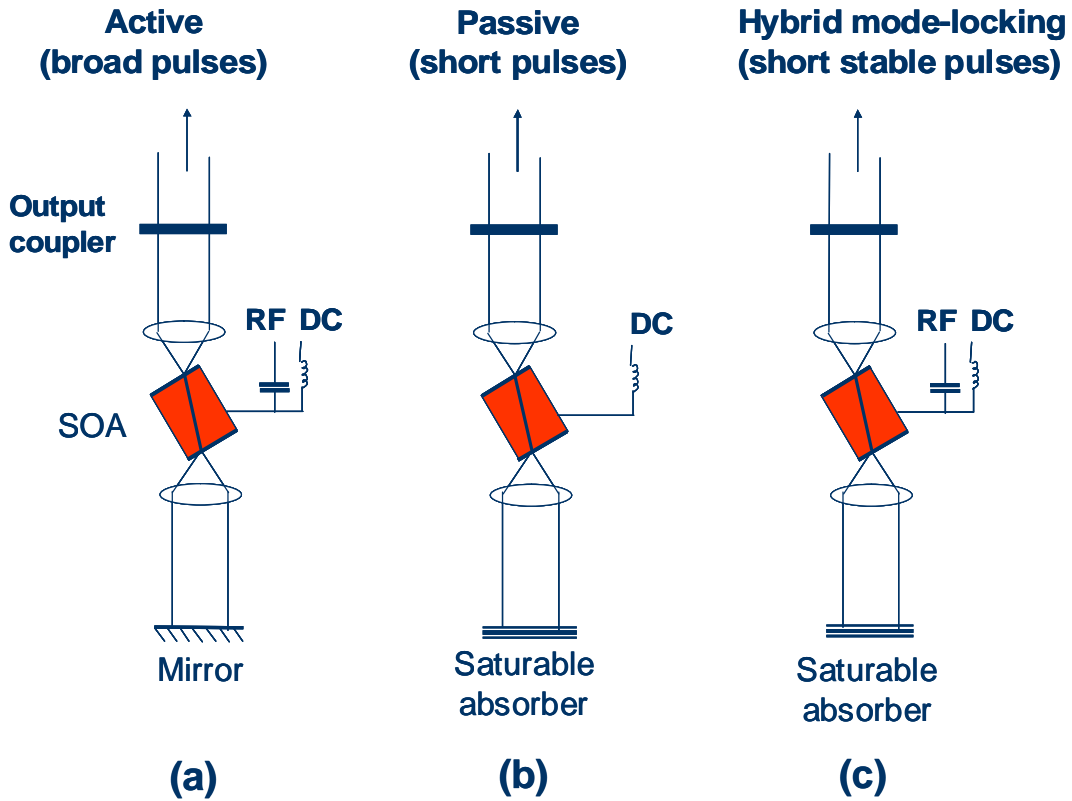


Figure 9: Three types of semiconductor laser mode locking: (a) active, (b) passive, and (c) hybrid.

In active mode locking the radio frequency (RF) power modulates the SOA additionally to DC biasing, with the frequency matching the laser cavity resonant frequency or its higher harmonic. The laser resonator is formed with two mirrors surrounding the SOA, one being partially transparent. The duration of the generated pulses is in the range of tens of ps. If one mirror (e.g. back mirror) is replaced with a saturable absorber and no RF is applied, passive mode locking is established. As explained in the previous section, passive mode locking can generate fs-range pulses [33], [37] using the SA with a recovery time of approximately 200 ps (referred to in the literature as a slow saturable absorber). The pulse train repetition rate of the passively mode-locked laser will be defined by the SOA recovery time. However, the pulse train of the passively mode-locked laser exhibits more amplitude and timing jitter [26]. Hybrid mode locking combines advantages of passive and active mode locking. Fs-range pulses are produced by the interaction of the SA with the saturable gain of the SOA and, additionally, amplitude and time jitter are suppressed with the applied RF. In our experiments in this chapter, the laser is passively mode-locked for characterization while the cavity length is tuned by moving gratings in compressors. Later on, in following chapters grating positions and cavity length are fixed and laser is hybridly mode-locked to increase the stability.

Prior to investigating the mode-locked laser operation, it is important to check the laser in the continuous wave (CW) mode of operation. The ring semiconductor laser setup is presented in Figure 10. For CW laser operation, a mirror is used in the place of the SA. An optical isolator permits propagation only in the counterclockwise direction inside the cavity. Since the SA is designed for normal incidence (SA to be placed in the same cavity in following experiments), a sigma-shape ring cavity is realized by an optical circulator comprising wave plates and a polarizing beam-splitter. The pellicle is a 2 micron thin nylon membrane with a partial

reflectivity of 4% for a 45 degrees incident angle, at 830 nm. The low reflectivity pellicle is used as a laser output, since the lowest cavity loss is desirable. With the further incorporation of compressors and the SA in the cavity (next section of the dissertation), the total loss increases to more than 90%. With the high cavity loss, the SOA has to be driven with higher current that can lead to a significant shortening of the SOA operational lifetime. Therefore, to increase the SOA and the laser operational lifetime, the loss should be minimized and the laser cavity should be very carefully aligned.

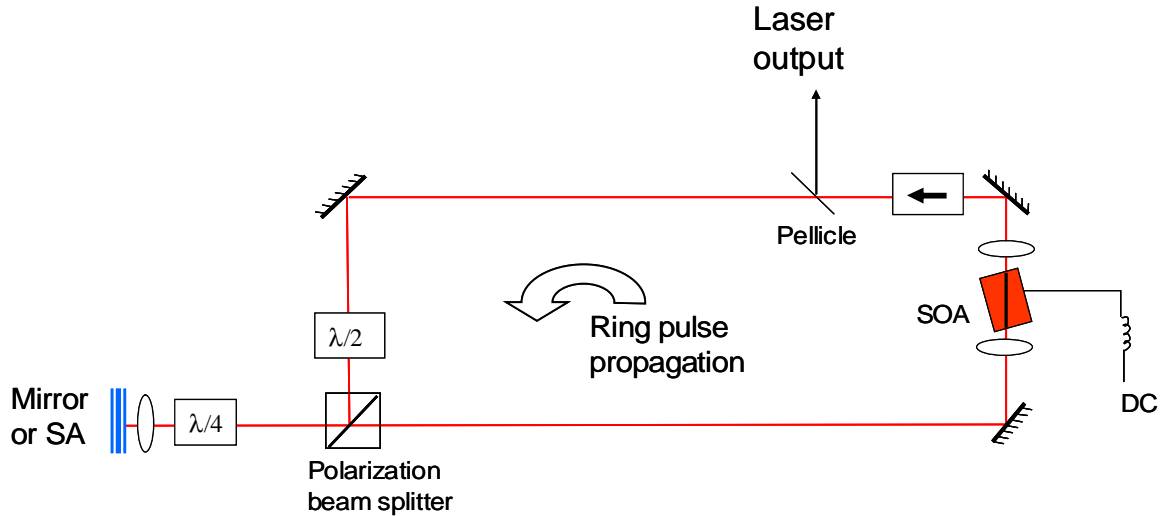


Figure 10: Setup for CW or mode-locked operation of the external-cavity semiconductor ring laser without dispersion management.

The L-I curve of the CW external-cavity semiconductor ring laser is shown in Figure 11. A low CW laser threshold of only 65 mA driving current is obtained. The output power increases linearly up to 180 mA of drive current without rollover and there are no mode-hopping kinks.

After aligning the CW ring cavity for the lowest threshold and the proper wavelength, the mirror is replaced with the SA for passive mode locking. The CW laser operation wavelength should be adjusted to match the excitonic absorption wavelength of the SA. The wavelength tuning of the CW laser is performed using two effects. First, using chromatic aberration of the triplet lens focusing the beam to the SA, the beam can be tuned to different wavelengths. Second, the beam focused back to the SOA could be slightly redirected with the last ring mirror to make use of the SOA waveguide chromatic dispersion. More than 30 nm of wavelength tuning was possible for CW laser operation.

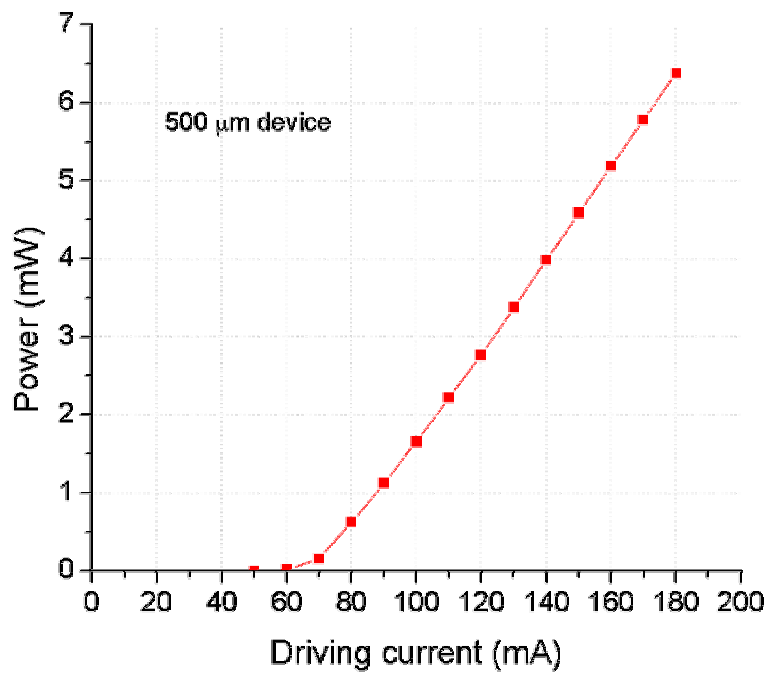


Figure 11: L-I curve of the CW operating external-cavity semiconductor ring laser.

Without dispersion management a typical passive mode-locked laser output spectrum and pulse second-harmonic intensity autocorrelation are presented in Figures 12 and 13. It should be

mentioned that the high frequency noise in Figure 12 is from the CCD camera used with the monochromator in the measurement. The spectrum is quite narrow owing to the wavelength mismatch of the SOA gain peak around 850 nm and the SA excitonic absorption band around 835 nm.

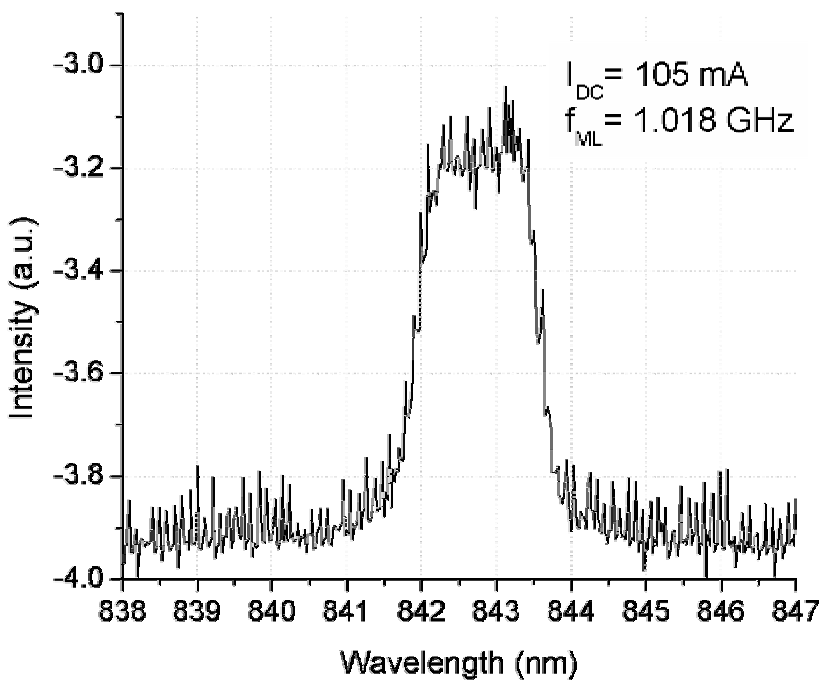


Figure 12: Typical output spectrum for passively mode-locked laser without dispersion management.

The laser output pulses are broad, 1.2 ps assuming a sech^2 pulse temporal profile, with significant wings from secondary pulses caused by strong cubic spectral phase. Cubic spectral phase and quadratic chirp are impressed on the laser output pulse by the strong integrating SPM as described with Figure 2. To avoid this and generate much shorter pulses, we introduce dispersion management.

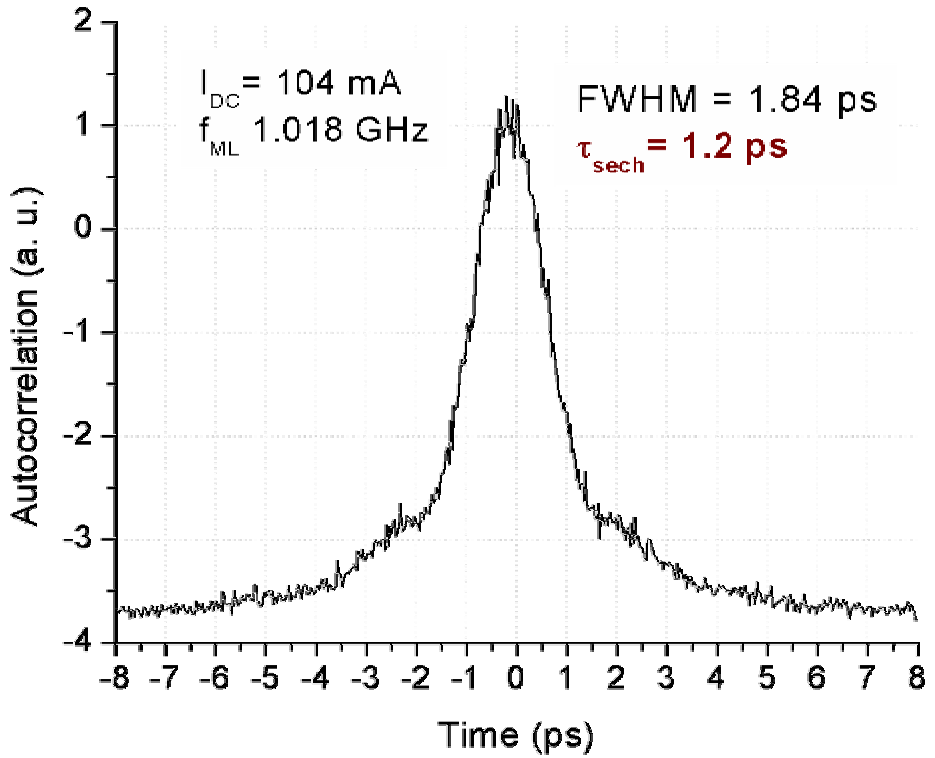


Figure 13: Typical output pulse second-harmonic intensity autocorrelation for passively mode-locked laser without dispersion management.

3.3. Intracavity dispersion management and breathing mode laser operation

After building the basic ring cavity, checking the CW and passive mode-locking laser operations, dispersion management is introduced. The salient feature is the incorporation of the compressor and stretcher inside the ring laser cavity as sketched in Figure 14.

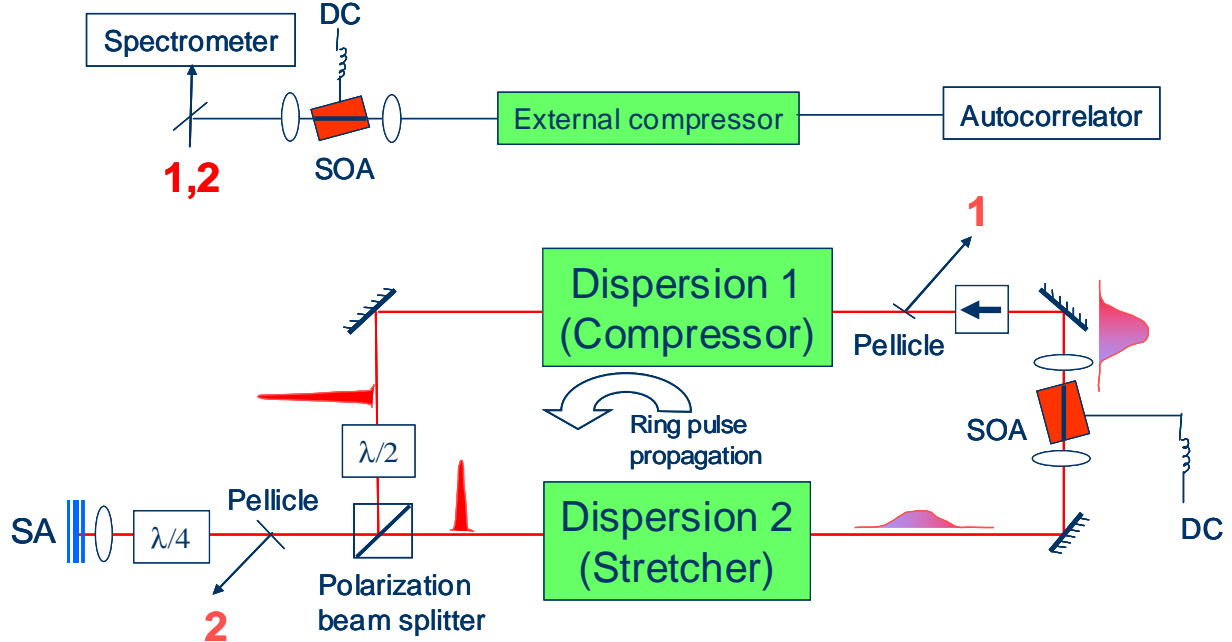


Figure 14: Experimental layout of (bottom) dispersion-managed mode-locked semiconductor σ -ring cavity laser and (top) diagnostics.

The dispersion elements 1 and 2 as well as an external compressor, are typical dual-pass grating-pair dispersion compensators with internal telescopes as shown in the Figure 15. They can introduce a positive (normal) or negative (anomalous) GVD depending on the relative position between gratings [41], [28].

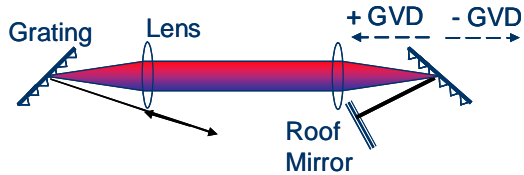


Figure 15: Geometrical sketch of the double-pass grating-pair dispersion compensator performing as a compressor or stretcher.

The GVD introduced by such a double-pass compressor is given by [41]:

$$\frac{\Delta t}{L\Delta I} = \frac{2 \frac{I}{d}}{cd \left[1 - \left(\frac{I}{d} - \sin g \right)^2 \right]} \quad (18)$$

where Δt is group delay in seconds, L is the distance of the grating away from 0 GVD position in meters, ΔI and I are the spectral width and wavelength in meters, d is the line spacing of the grating in meters, c is the speed of light and g is the beam incident angle with respect to the grating normal. Units of ps/(nm m) are more intuitive to work with than fs^2/m (unit of GVD parameter k'') when large amounts of dispersion are calculated, e.g. in fiber propagation or grating compressors. The ultrafast community uses the more common units of fs^2/m , when pulses and phenomena on the 10 fs time scale are calculated. As an example, the optical glass BK7 at 620 nm has $k''=10^{-25} \text{ s}^2/\text{m}$ or 5 fs/(nm cm). The compressor in our experiment in the double-pass configuration introduces 830 fs/(nm cm) at 830 nm for an incident angle of 38 degrees – more than 100 times larger introduced GVD compared to BK7.

The ratio of the cubic to the square term in the expansion of the grating spectral phase response could be calculated as following [28]:

$$R_G = \left| \frac{b_3(w - w_l)^3}{b_2(w - w_l)^2} \right| = \left| \frac{\Psi'''(w_l)}{3\Psi''(w_l)} \right| |w - w_l| \approx \frac{\Delta I_l}{I_l} \left[1 + \frac{I_l/d(I_l/d - \sin g)}{1 - (I_l/d - \sin g)^2} \right] \quad (19)$$

In our case, for a laser wavelength of 835 nm, and gratings with 1800 lines/mm and an incident beam angle of 38°, the cubic phase is 0.07 % of the quadratic phase. However, in our setup, the external compressor has the same geometry as the intracavity stretcher. Therefore, when both of them are properly aligned, the cubic and higher order spectral terms introduced to the generated laser output pulse by the stretcher, should be canceled by the external compressor.

The σ -cavity laser output is directed to a spectrometer or to an external SOA to boost the power prior to the external compressor and the autocorrelator. The external cavity SOA is a device of the same type as the internal cavity gain SOA. The pulse train repetition rate is 1.116 GHz, corresponding to the 31st harmonic of the laser cavity. The pulse spectrum after the SA (output 2) is recorded while keeping the introduced dispersion by element 2 constant and varying the dispersion introduced by element 1. The spectral change is shown in Figure 16 for a fixed dispersion of 4.57 ps/nm introduced by element 2. In each dispersion element, a 1cm grating position variation corresponds to an introduced dispersion of 0.83 ps/nm. There is an optimal grating position in element 1, which introduces approximately -0.25 ps/nm additional dispersion than that introduced by element 2. When such an optimal dispersion is introduced, the obtained spectrum is the broadest and pulses are compressible to their shortest duration. The optimal total dispersion of -0.25 ps/nm introduced by elements 1 and 2 compensates the dispersion of other intracavity elements. Clearly, small variations in the total cavity dispersion cause dramatic changes in the spectral shape and width.

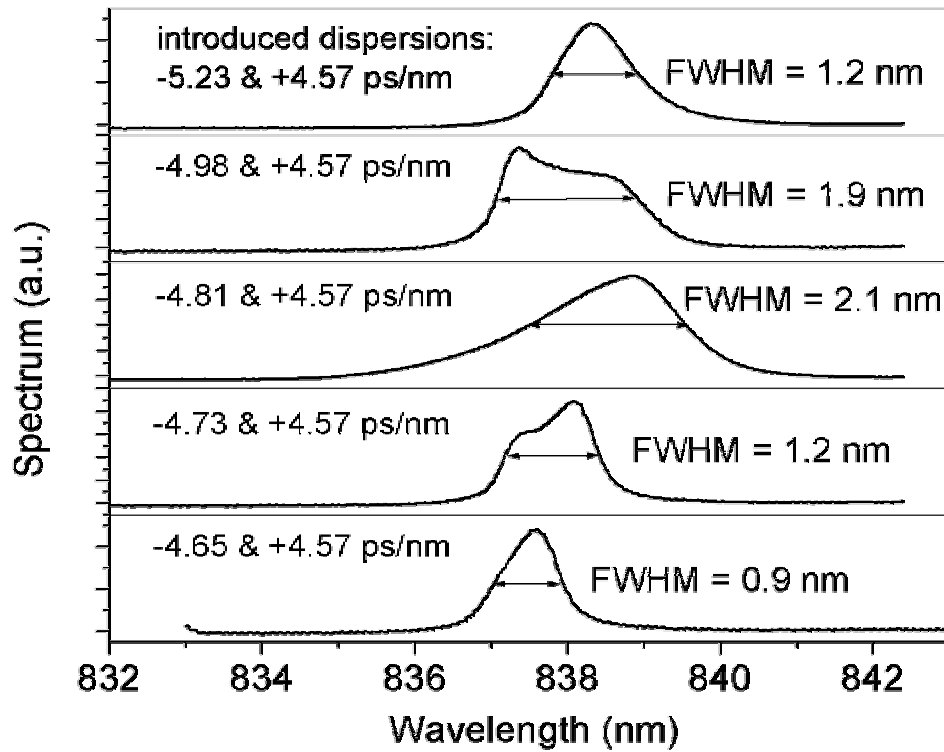


Figure 16: Spectral changes when dispersion introduced by element 1 is varied and dispersion introduced by element 2 is constant.

The second-harmonic intensity autocorrelation full-width at half-maximum (FWHM) after the gain element (laser output 1) is measured versus dispersion introduced by elements 1 and 2 as shown in Figure 17. Data points are collected at different grating positions yielding approximately 200 data points, and the overall map is obtained by interpolation. On-diagonal map values occur for introduced dispersions of equal magnitude and opposite signs in elements 1 and 2. When the laser operates in the regime near the diagonal region of the map, output pulses are well organized in phase, shorter, and without coherent spikes. In contrast, noise bursts – temporally broad pulses with coherence spikes - are observed in off-diagonal map regions of laser operation.

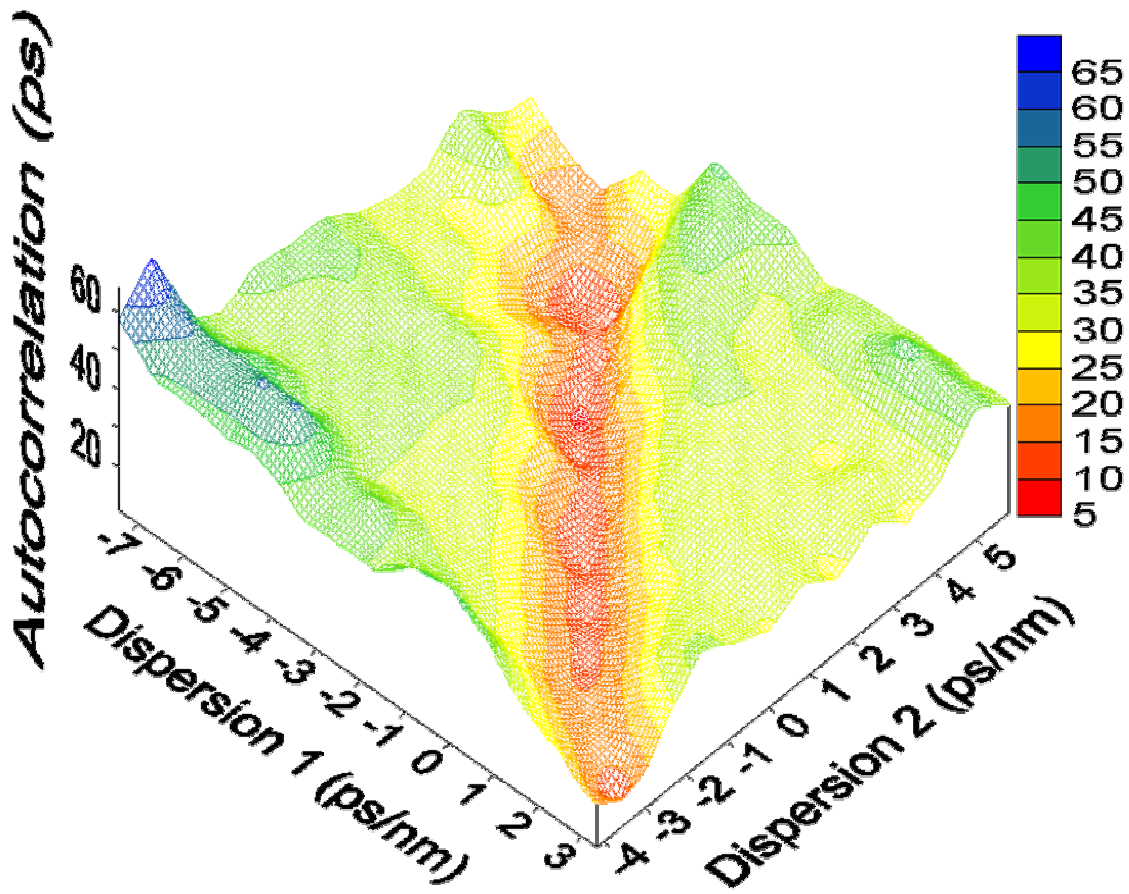


Figure 17: Laser output pulse second-harmonic autocorrelation FWHM versus introduced dispersions by element 1 and 2.

Similarly, the spectral FWHM is measured after the SA (output 2) and is plotted versus dispersion in elements 1 and 2 in Figure 18.

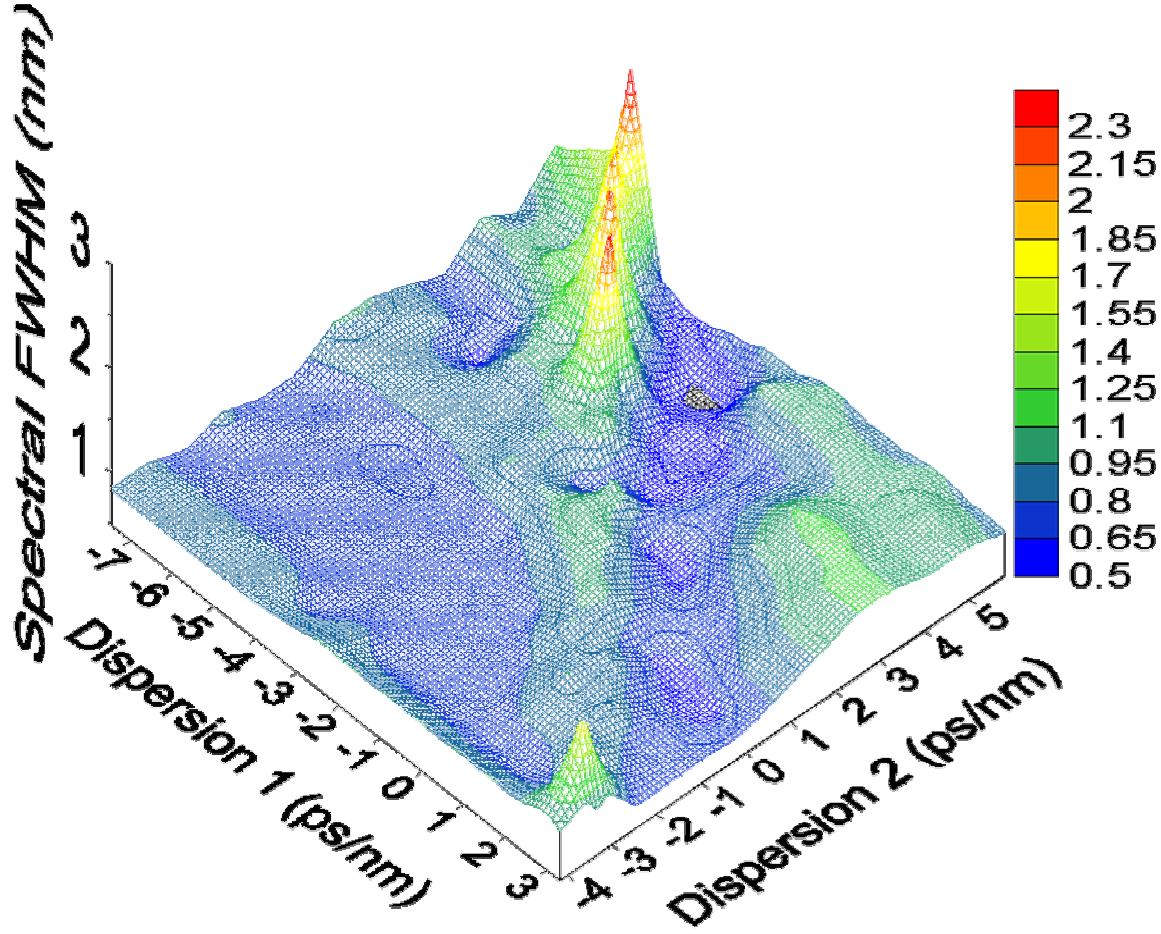


Figure 18: Laser output spectral FWHM versus introduced dispersions by element 1 and 2.

Hybrid mode locking improved the laser stability while performing the intracavity pulse evolution characterization. With the same cavity configuration (see Figure 19), the intracavity SOA is 92 mA dc-biased and a superimposed radio frequency (RF) sinusoidal signal modulates the gain at 323 MHz to enable ninth-harmonic hybrid mode-locking. Introduced dispersions are fixed to -5 and +5 ps/nm in the elements 1 (compressor in this case) and 2 (stretcher), respectively.

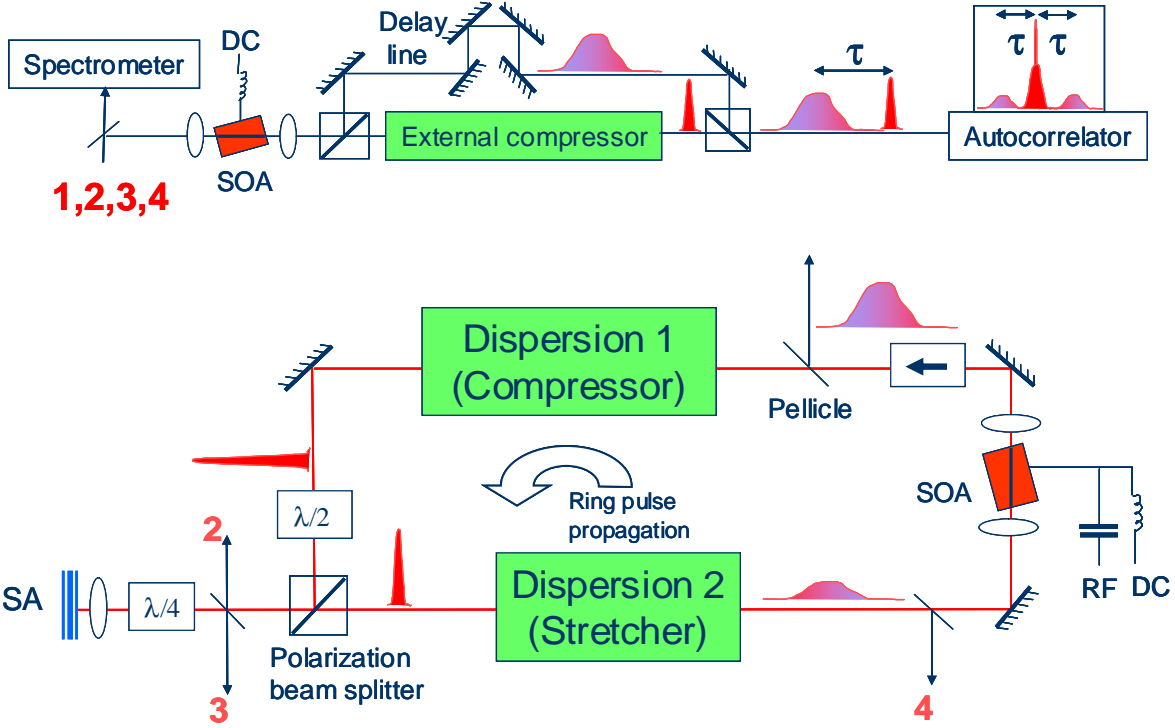


Figure 19: Hybirdly mode-locked sigma cavity semiconductor laser (bottom) with 4 outputs for pulse evolution characterization and (top) diagnostics.

The lower part of Figure 19 shows the mode-locked semiconductor sigma-ring cavity, and the upper part shows the setup for measurement of spectra as well as autocorrelation and crosscorrelation traces. Four laser outputs are provided to determine the pulse behavior after the gain medium (1), before the SA (2), after the SA (3), and before the gain medium (4). Optical spectra from the four points of the cavity are shown in Figure 20. The spectra are similar in shape and have the same peak wavelength at 839 nm.

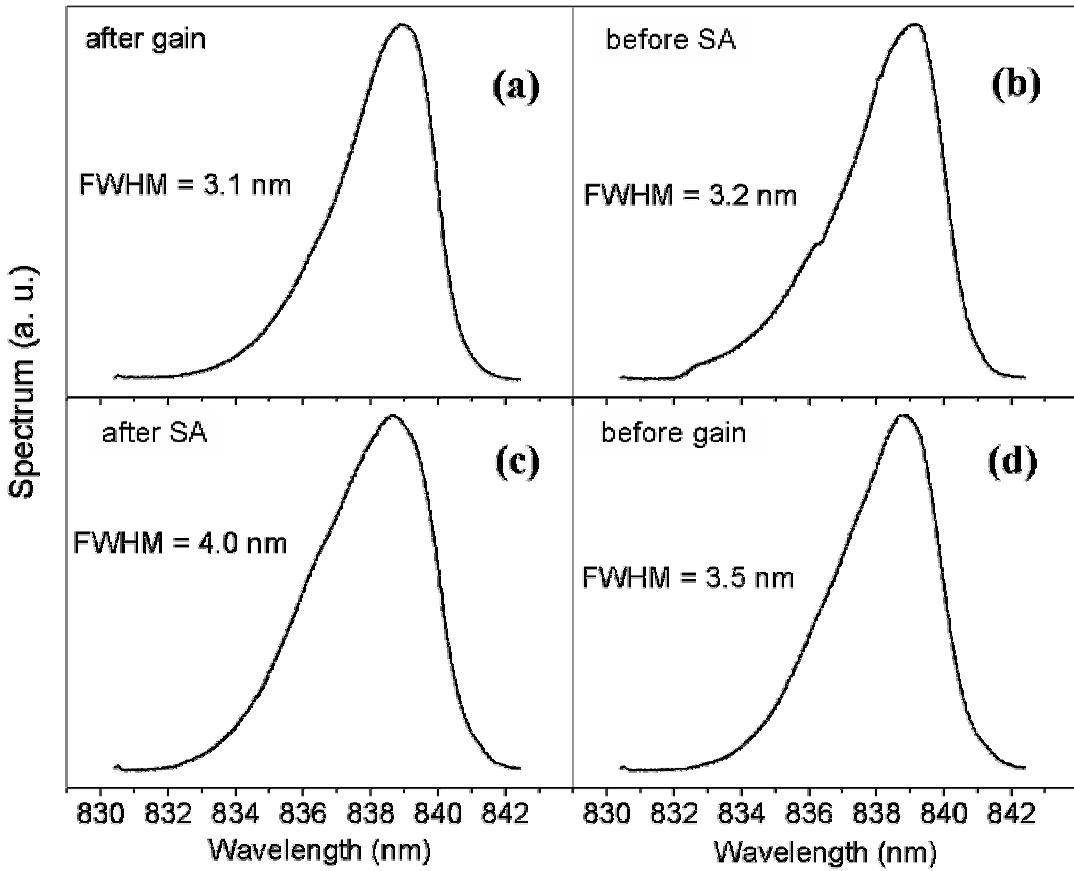


Figure 20: Optical power spectra: (a) after the gain media, (b) before the SA, (c) after the SA, and (d) before the gain media. Experimental error is 0.2 nm.

As depicted in the upper part of Figure 19 for the temporal measurements, the signals from the different cavity outputs are split after the external-cavity SOA amplifier. Half of the beam is guided through the delay line and then recombined with the other half, which has passed through the external compressor. The pulse from the cavity is combined with a compressed version of itself, with a small delay t , and the autocorrelator signal reveals the two pulse autocorrelation trace [42]. The side-peak in the trace represents the crosscorrelation between the two versions of the same pulse. Assuming that the compressed version of the pulse is much

shorter than the original (in our case more the 40 times shorter), the crosscorrelation trace measures the temporal intensity profile of the original pulse. The principle of the pulse temporal profile measurement with the two-pulse autocorrelation method is illustrated in Figure 21.

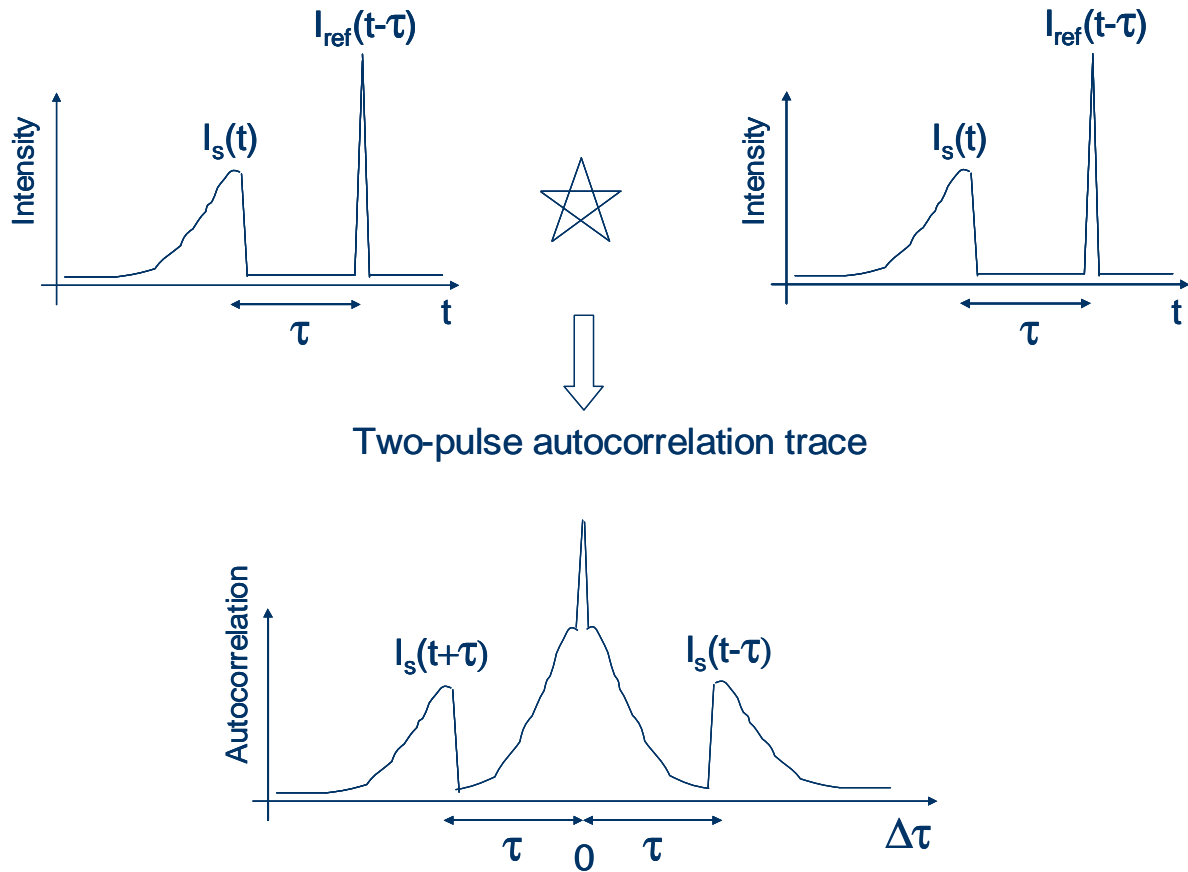


Figure 21: Principle of the pulse temporal intensity profile measurement via two-pulse intensity autocorrelation – sampling of a broad pulse with a much narrower one.

Mathematically, this method can be described as follows. The total incident intensity to the autocorrelator is the sum of the pulse to be sampled, $I_s(t)$ and the reference pulse separated by a small time delay t , $I_{ref}(t-t)$:

$$I(t) = I_s(t) + I_{ref}(t - t) \quad (20)$$

The two-pulse autocorrelation signal reveals the trace:

$$A(\Delta t) = \int_{-\infty}^{\infty} I_s(t)I_s(t - \Delta t)dt + \int_{-\infty}^{\infty} I_{ref}(t)I_{ref}(t - \Delta t)dt + I_s(\Delta t + t) + I_s(\Delta t - t) \quad (21)$$

where the first two terms are the autocorrelations of the sample and reference pulses respectively, overlapped in the middle of the trace (see Figure 21). The third and fourth terms are the crosscorrelations of the sample and the reference pulses. If the reference pulse is much shorter than the sample pulse, it can be approximated as the Dirac Delta-function $\delta(t)$. As shown previously in Equation (16), the crosscorrelation of a function (in this case sample pulse) with the delta function (reference pulse) provide us the temporal profile of the function. Therefore, the side peaks in the two-pulse autocorrelation trace (Figure 21) are the third and fourth term of Equation (21) which represents the sample pulse temporal intensity profile.

The time delay between the pulses t should be on the time scale of the broad pulse duration, but at least around three times the broad pulse FWHM in order to avoid overlapping of the middle autocorrelation trace with the side crosscorrelations, as could be inferred from Figure 21.

In Figure 22 the measured crosscorrelation traces of pulses from the four key cavity points are displayed.

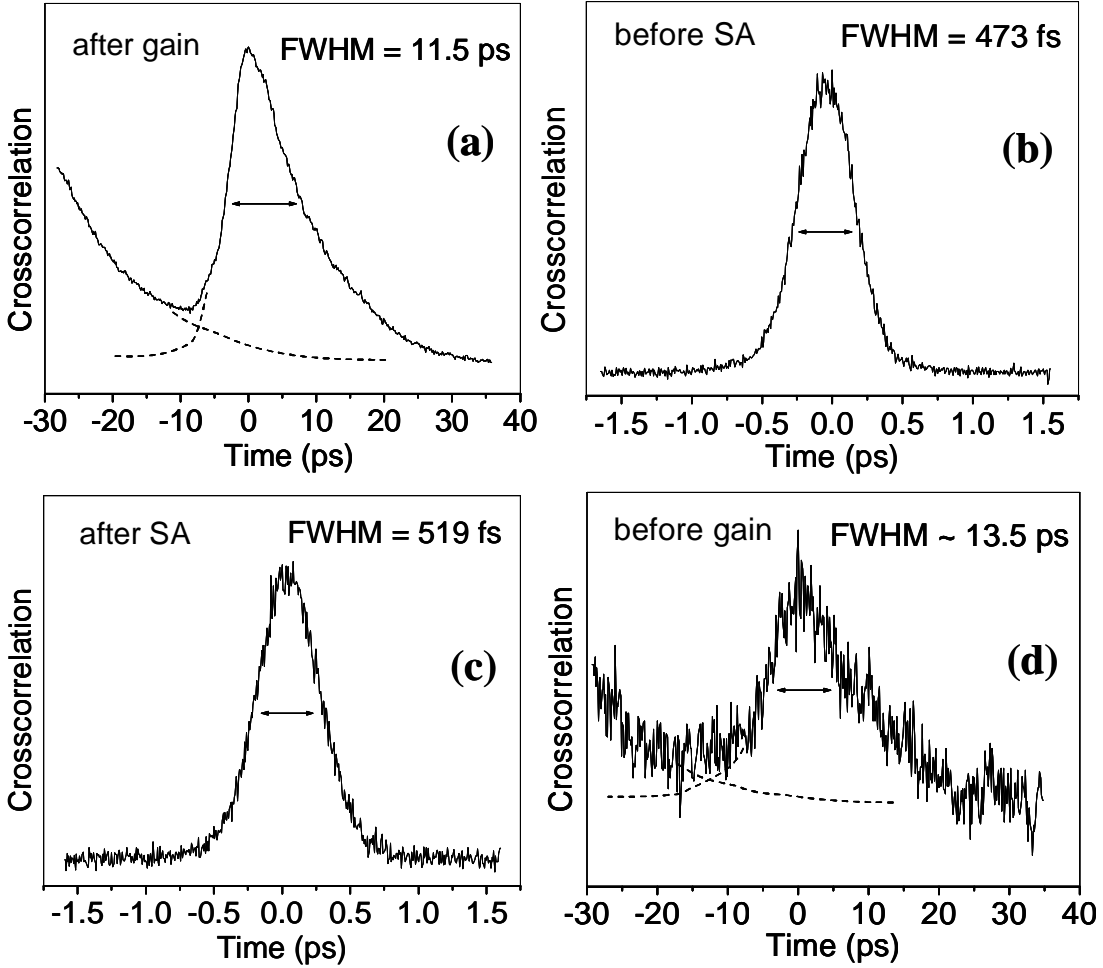


Figure 22: Crosscorrelation traces from the four key cavity points: pulses (a) after the cavity gain element, (b) before the SA, (c) after the SA, and (d) before the gain element.

The stretched pulses exhibit an asymmetric temporal profile with a steep leading edge and a long trailing edge. The sharp leading edge is due to the incorporation of the SA [15] and the long exponentially decaying trailing edge is governed by the gain depletion dynamics. The stretched pulse traces in Figures 22(a) and (d) also contain an artifact from the autocorrelation. The dashed line depicts how the contributions from autocorrelation and the crosscorrelation overlap. The crosscorrelation traces from before and after the SA in Figures 22(b) and (c) are

similar to the autocorrelation, since those are already short pulses in the cavity and are not externally compressible. One can observe that the crosscorrelation time scale is 20 times larger in the traces taken before and after the gain element (stretched pulses) compared to before and after the SA (compressed pulses). The dramatic change of the pulse duration while propagating within the cavity demonstrates that the laser operates in the breathing mode. The “breathing-mode” designation derives from the fact that the intracavity pulses are alternately stretched and compressed as they circulate around the ring resonator, changing the pulse width more than 20 times [43]. The pulse energy after the cavity gain media is more than 100 times higher than before the gain media [see the signal to noise ratios in Figures 22(a) and (d)]. This verifies that efficient intracavity chirped pulse amplification is achieved.

It should be noted that the effects of nonlinear pulse distortion in the external SOA have been minimized and quantified. The pulse spectrum and autocorrelation were measured prior to and following the external cavity SOA, with nearly identical results, and yielding higher signal to noise ratios (SNRs). The highest laser output pulse energy after the intracavity gain SOA does not activate nonlinear pulse distortion because the pulses are stretched and therefore the SPM is decreased. The average powers of the laser outputs with short intracavity pulses (before and after the SA) were much lower due to high cavity losses. In this case, the SOA can operate closer to the linear regime. However, the compressed intracavity pulses experienced a pulse broadening of 100-200 fs while propagating through the external SOA.

CHAPTER 4: NUMERICAL SIMULATIONS OF THE DISPERSION-MANAGED BREATHING-MODE SEMICONDUCTOR MODE-LOCKED RING LASER

4.1. Explanation of numerical simulations algorithm and parameters

The phenomenological theory of homogeneous laser frequency and amplitude modulation mode locking was developed back in late 1960s [44]. From the modified nonlinear Schroedinger equation the master mode locking equation was derived by H. A. Haus [45]. Assuming small pulse changes within the laser cavity, exponential terms in the master mode locking equation can be approximated with power expansions. In this case, an analytical solution for a mode-locked laser pulse is attainable [45]-[47]. Later on, H. A. Haus modeled the gain and noise of the external cavity mode-locked semiconductor laser [48] and semiconductor laser mode locking using MQW SA [49]. This and the subsequent work about mode-locked semiconductor lasers follow the approach of the power expansion in the master mode locking equation [50]-[52]. However, in a dispersion-managed breathing-mode semiconductor mode-locked ring laser the pulse changes the energy more than 100 times and the temporal duration more than 20 times while propagating within the cavity, as demonstrated in the previous section. In this case, a power expansion is not an appropriate approach. Numerical simulations are

necessary since there are no analytical solutions to the modified nonlinear Schrödinger equation. Profound numerical simulations of the single-pass ultrafast pulse propagation through the SOA were presented, including effects of GVD, SPM, and two-photon absorption (TPA), with the dependencies on the carrier depletion, carrier heating, spectral hole burning and their dispersions, including recovery times [53]. The SOA ultrafast single-pass pulse propagation model was extended to include current-induced gain saturation and gain recovery dynamics [54]. A numerical study of a linear cavity mode-locked laser with a dual-section monolithic device [55] and, more recently frequency shifts in external cavity semiconductor lasers [56] (no dispersion management) were reported. All the above-mentioned work is based on the rate equations as the starting point. Recently, progress has been reported in the semiclassical theory [57]. The Maxwell's equations and the coherent semiconductor Bloch equations as the starting point are coupled to the microscopic carrier scattering. The microscopic simulations described the ultrafast pulse breakup in the single-pass SOA gain regime and pulse compression in the transparency regime.

In our ring laser with the dispersion management, the ultrafast effects in the SOA do not need to be considered since the pulse propagating through the SOA is approximately 10 ps in duration, as presented in the previous chapter. The Split-Step Fourier algorithm is employed to simulate the laser pulse formation from random noise input [58]. Elements in the algorithm are arranged in an order analogous to the dispersion-managed mode-locked ring laser as sketched in Figure 23. The saturable gain and absorption, GVD, and SPM are the main physical mechanisms involved in the pulse formation and shaping as explained in Chapter 2. A time filter of FWHM = 131 ps is presented in Figure 24.

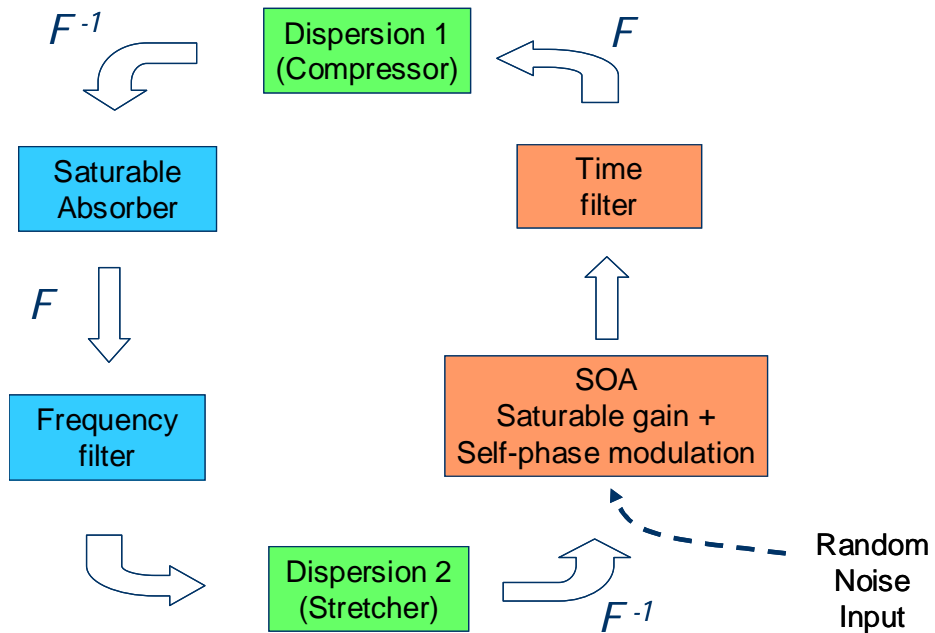


Figure 23: Algorithm for dispersion-managed mode-locked ring laser simulations.

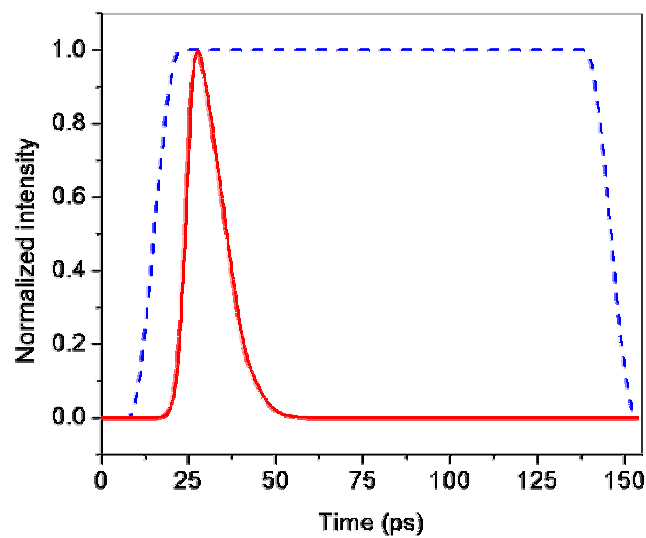


Figure 24: Normalized laser output pulse after the gain media and temporal filter with FWHM = 131 ps.

A frequency filter with $\text{FWHM} = 7.6 \text{ nm}$ accounts for the finite bandwidth of the excitonic saturable absorption and semiconductor gain as illustrated in Figure 25. Both the spectral and the temporal filter profiles are step functions with sinusoidal edges as shown in Figures 24 and 25. The sinusoid edges suppress more efficiently potential aliasing problem (sometimes also referred as the boundary reflection or window leakage) than e.g. Gaussian function, since the sine values are exactly zero at the edge of the time or frequency window. The main part of the time filter is unity function representing the RF modulation of the SOA above the laser threshold. The SOA is RF modulated with a sine wave of period of 3 ns for 323 MHz pulse repetition rate. The top of the sine wave with 3 ns period can be approximated with a flat surface when considering the optical pulse shaping of approximately 10 ps in duration. The step function area in the spectral filter is very narrow, performing essentially as a half of a sinusoid.

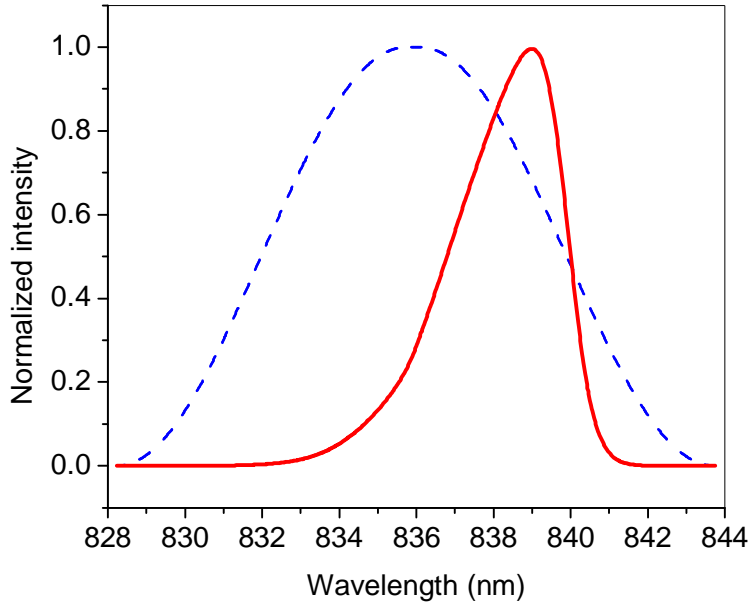


Figure 25: Normalized laser output pulse spectrum after the gain media and spectral filter with $\text{FWHM} = 7.6 \text{ nm}$.

The results from the simulations are scaled to the measured pulse energies after the cavity gain element $E_{SOA} = 33$ pJ and after the saturable absorber $E_{SA} = 0.86$ pJ. The most important constants used in simulations are summarized in Table 1.

Table 1: List of parameters used for simulations of the dispersion-managed breathing-mode mode-locked semiconductor ring laser.

Parameter	Value
SOA small signal gain exponential coefficient	96 cm^{-1}
SOA saturation energy	20.14 pJ
SA unsaturated reflectivity	2.2 %
SA saturation energy	0.31 pJ
Integrating SPM coefficient	0.35 pJ^{-1}
Introduced GVD by dispersion element 1	- 4.10 ps/nm
Introduced GVD by dispersion element 2	4.11 ps/nm

The simulations parameters are within the same order of magnitude when compared to values in the literature [34], [50], [51], [53]. Ultrafast effects in the SOA are not included as

explained earlier and the SOA gain recovery time is considered to be infinite in the model. The SOA gain recovery time can be approximated to infinity since previous measurements [15], [39] showed the SOA gain recovery time of approximately 500 ps compared to the time window of 150 ps in simulations and the propagating laser pulse duration of 10 ps. The SA recovery time is also considered to be infinite in our simulations as the measured value [15] of approximately 200 ps is much longer than the laser pulse duration of less than 1 ps, incident to the SA.

The pulse energy after the cavity gain element (SOA) is 1.64 times larger than the SOA gain saturation energy. The pulse energy after the SA is 2.8 times larger than the saturation energy of the SA, in agreement with a value of 3-5, as a rule of thumb for stable mode locking [59].

More detailed explanations about the simulations are provided in Appendix A containing the full code listing with comments.

4.2. Laser mode locking build-up

The mode locking build-up of the stretched pulse after the gain media is illustrated in Figure 26. Random noise is used as the laser input as could be seen in the first couple of cavity round propagations. The noise in the laser evolves into the steady-state mode-locked pulse shape in approximately 350 cavity round trips. In our case for 7.5 meters ring cavity length this corresponds to approximately 9 μ s.

Figures 27 and 28 display the build-up of the mode-locked laser spectra after the cavity gain element SOA and after the SA.

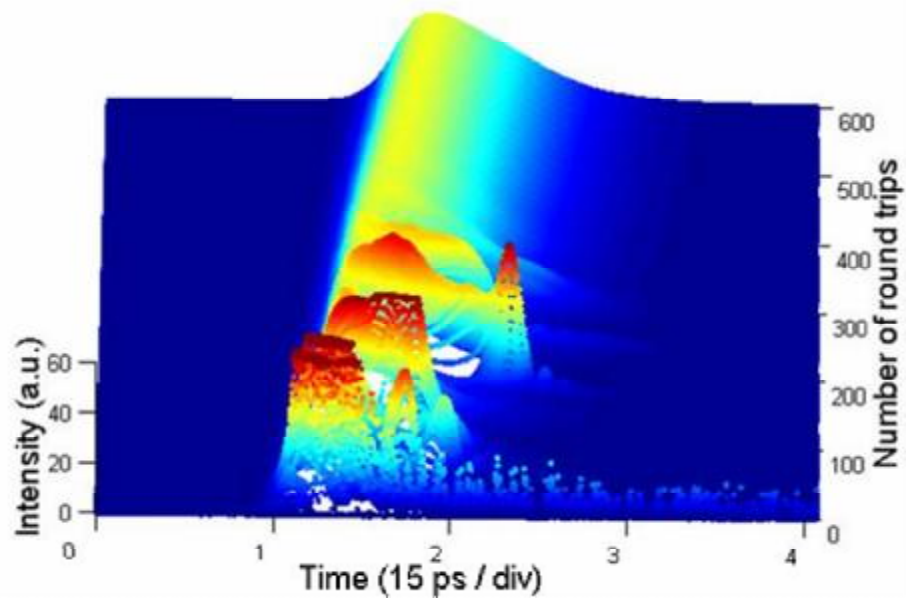


Figure 26: Build-up of the mode-locked stretched pulse temporal intensity profile after the gain media from random noise input.

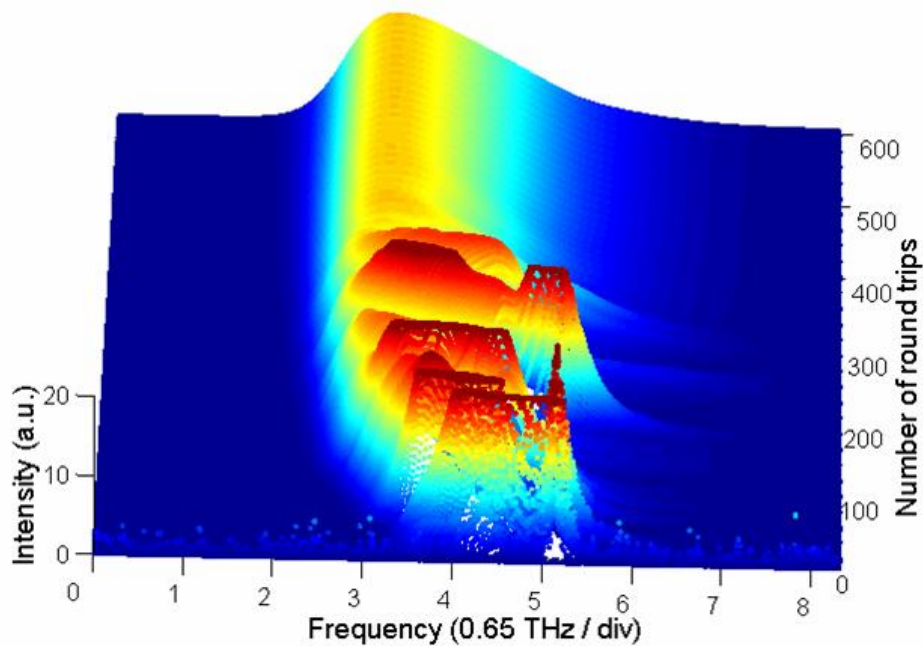


Figure 27: Formation of the mode-locked stretched pulse spectral profile after the gain media.

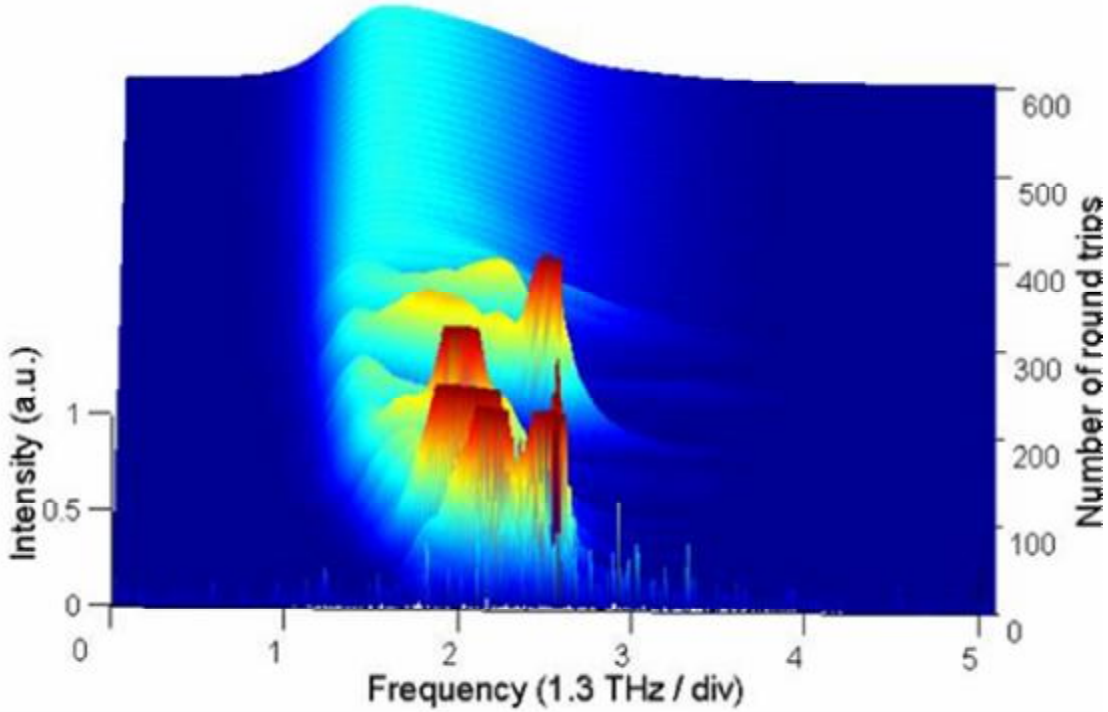


Figure 28: Mode-locked spectrum evolution of the intracavity compressed pulse after the SA.

The steady-state pulse spectral and temporal intensity is extracted after 600 simulated cavity round trips and compared with the measured results. Figure 29 displays the comparison of the simulated and measured spectra of the intracavity stretched and compressed pulses. An excellent match is achieved between the spectra of both the stretched and compressed intracavity pulses. As presented in Figure 30, the main part of the simulated stretched pulse temporal profile fit well as compared to the experimentally measured pulse. The discrepancy in the pulse wings is addressed by noting the influence of the middle autocorrelation part of the two-pulse autocorrelation trace (see Figure 21). The leading part of the crosscorrelation trace in Figure 30 contains an artifact from the middle autocorrelation trace as in Figure 22(a) described previously,

which enhances the leading and the trailing edge of the pulse measured by the two-pulse autocorrelation method.

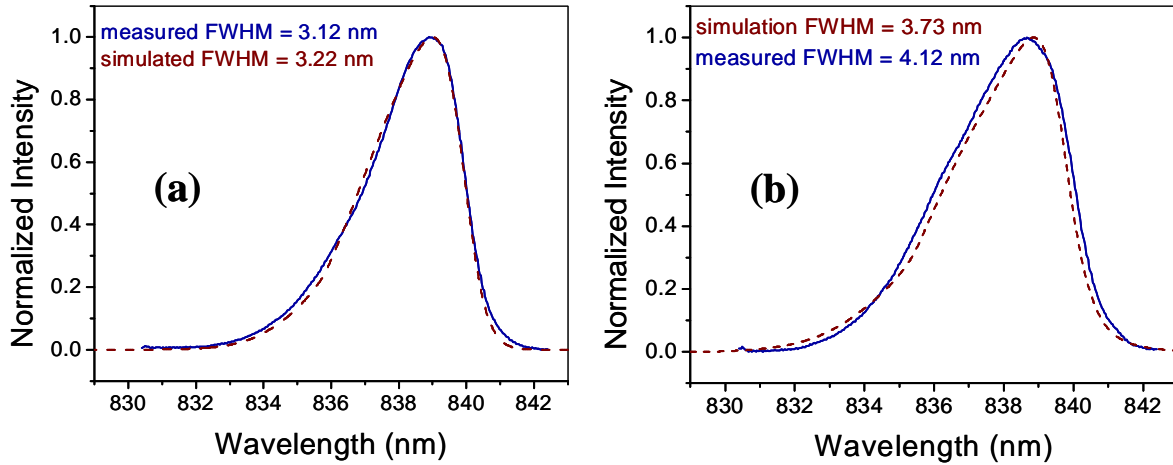


Figure 29: Comparison of (dashed) simulated and (solid) measured (a) stretched pulse spectrum after the SOA, and (b) compressed pulse spectrum after the SA.

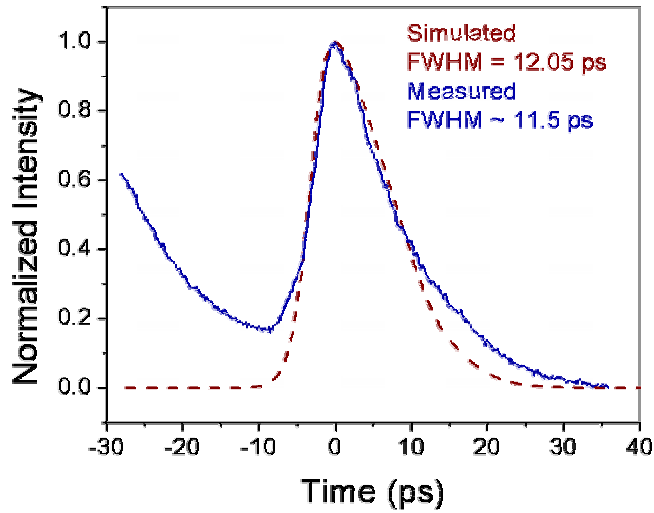


Figure 30: Comparison of (dashed) simulated and (solid) measured stretched pulse temporal intensity profile after the SOA.

The steady-state simulated compressed pulse temporal intensity profile after the SA is compared with the corresponding pulse retrieved by the PICASO method [60], [61] as shown in Figure 31. The pulse temporal intensity and phase are calculated by use of the PICASO routine from the measured spectrum and second-harmonic generation intensity autocorrelation. Both pulses exhibit the same trend. The simulated pulse is approximately 100 fs shorter than the pulse retrieved by PICASO. This error may be due to additional dispersion encountered in the experimental setup prior to the intensity correlation measurements, minor inaccuracies in the PICASO algorithm [62], [63], or the finite resolution of the temporal grid used in the simulation. Note that the difference between the retrieved pulse by PICASO and the pulse obtained through simulation differs by approximately 1 pixel point or 150 fs.

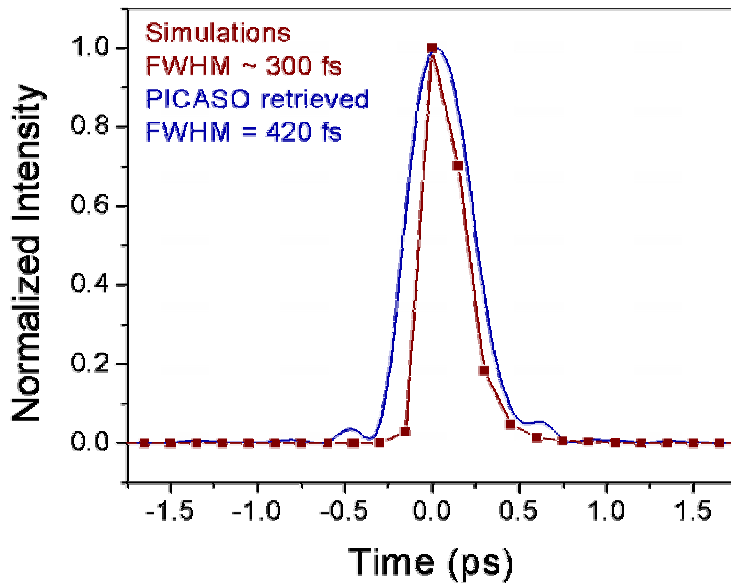


Figure 31: Comparison of (dashed) simulated and (solid) measured compressed pulse temporal intensity profile after the SA.

The very good agreement between the simulated and the measured results is obtained. This confirms our understanding and ability to control the physical mechanisms involved in pulse shaping within the ring cavity.

4.3. Injection locking of the ring laser

Additionally, the ability of dispersion-managed breathing-mode semiconductor mode-locked ring laser to lock-up to externally injected pulses is simulated. Investigations of laser injection locking properties are essential to determine the potential for optical clocking applications [6], [7]. Mode-locked semiconductor lasers, as compact, low noise ultrafast pulse sources are ideal candidates for clocking of future OTDM and WDM networks. Furthermore, seeding of the dispersion-managed semiconductor ring system as a chirped-pulse amplification system can be investigated for regenerative amplifier applications using a higher power intracavity SOA.

As an example, Gaussian pulses are used as an input for the injection locking simulation. The same parameters listed in Table 1 are used for injection locking simulation as in the mode locking buildup simulation. As illustrated in Figure 32, the lock-up is achieved after less than 50 cavity round trips, corresponding to less than 1 μ s for our ring laser cavity length of 7.5 m. The code with the more detailed explanations of the injection locking simulation is disclosed in the Appendix B of the dissertation.

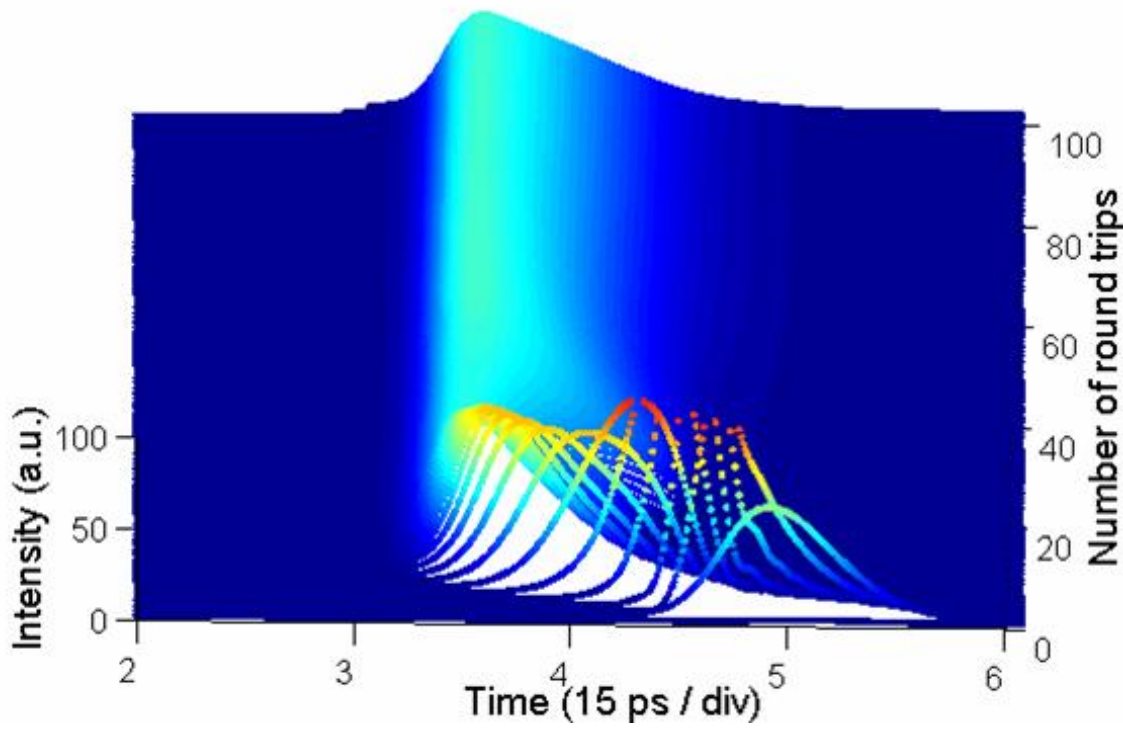


Figure 32: Locking-up of the laser stretched pulses after the SOA to the external-cavity injected Gaussian pulses.

The dispersion-managed semiconductor mode-locked laser could be easily built with a much shorter cavity length. The simulations indicate lock-up of such a short ring laser on the nanosecond time scale. This fast locking shows the great laser potential for the above-mentioned applications.

CHAPTER 5: THE PROPER CHOISE OF CHIRPING AND EXTERNAL CAVITY COMPRESSION TO PULSE DURATION OF 185 FS

5.1. External compression of up-chirped pulses down to bandwidth limit

The purpose of the novel dispersion-managed ring laser is to generate linearly chirped pulses that will enhance the efficiency of external-cavity amplification and compression. This chapter will be devoted to discussion of the targeted performance of the developed laser. As described previously and shown in Figure 14, an additional SOA is employed outside the laser cavity in the master oscillator power amplifier (MOPA) scheme to amplify the linearly chirped laser output after the intracavity gain SOA. The second-harmonic intensity autocorrelation is monitored following the external cavity pulse compression with a dual-pass grating-pair dispersion compensator.

In previous experiments [15], [26], [39], the external-cavity semiconductor mode-locked lasers exhibit up-chirped laser output pulses from linear or ring cavity geometries without dispersion management. The pulse is stretched inside the laser cavity by normal dispersion from the intracavity elements. Stretching the pulse with normal or positive dispersion produces the frequency increase along the pulse in temporal domain, or up chirping. Subsequently, the laser

output pulse is compressed by adding anomalous dispersion with external dispersion compensator.

Following this previous knowledge we started with up chirping of the dispersion-managed breathing-mode semiconductor mode-locked ring laser. The intracavity pulse is stretched prior to the cavity gain SOA by introducing enough normal dispersion. The pulse is compressed afterwards by adding anomalous dispersion with the intracavity compressor prior to the SA or, in the output path with the external cavity compressor for the shortest laser output pulses.

The comparison of the measured and the calculated second-harmonic autocorrelation of the externally compressed pulses is presented in Figure 33.

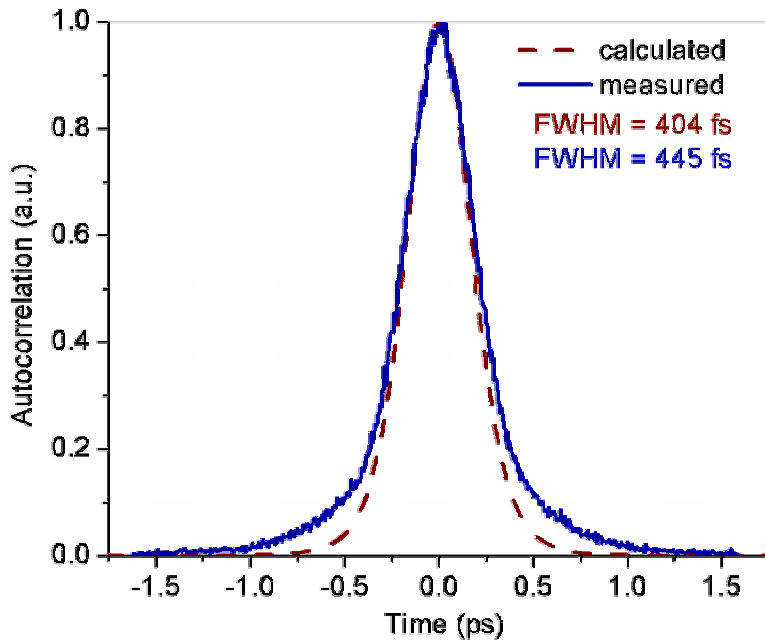


Figure 33: Comparison of the bandwidth-limited calculated (dashed) and the measured (solid) autocorrelations of the externally compressed up-chirped output pulses after the intracavity SOA.

The bandwidth-limited autocorrelation is calculated from the measured spectrum after the intracavity gain SOA [Figure 20(a)]. The details of the bandwidth-limited autocorrelation calculation are disclosed in the Appendix C. The calculated autocorrelation FWHM of 404 fs is only 10% shorter than the measured FWHM of 445 fs. This implies that efficient intracavity linear chirping and external cavity compression are achieved.

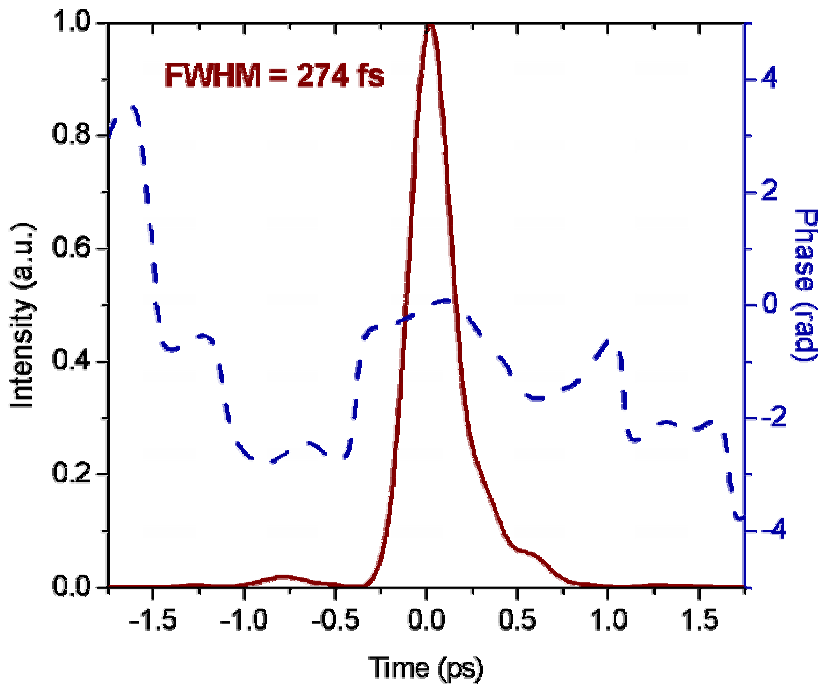


Figure 34: PICASO retrieved temporal intensity (FWHM = 274 fs) and phase of the externally compressed up-chirped output pulses after the intracavity gain element.

The externally compressed laser output pulse temporal intensity and phase are retrieved with the PICASO algorithm and presented in Figure 34. As expected, an asymmetric pulse with a longer trailing edge is obtained. The pulses from the output after the cavity gain SOA are externally compressed to FWHM = 274 fs. A measured average amplified power of 6.3 mW

after external compression at the pulse repetition rate 323 MHz would correspond to a pulse energy of approximately 19 pJ with a peak power of approximately 70 W and a focused intensity of approximately 1 GW/cm².

5.2. Preference for down chirping owing to the spectral and temporal pulse shaping

In principle, the dispersion-managed breathing-mode semiconductor mode-locked ring laser can provide up-chirped or down-chirped laser output pulses. In the up chirping regime the pulse propagating through the gain is stretched by introducing positive (normal) group velocity dispersion (GVD) and in the down chirping the pulse is stretched by introducing negative (anomalous) GVD. The intracavity gain SOA has a red shifted gain peak with respect to the SA excitonic absorption band, as illustrated in the Figure 35. The mode-locked laser spectrum is located between the SOA's gain peak and the SA's excitonic absorption band. Such a wavelength distribution results in the higher gain in the red part of the laser spectrum.

The SOA temporal and spectral properties as well as its response to the propagating up- or down-chirped pulses are sketched in the Figure 36. In the up chirping regime the pulse is stretched with normal (positive) dispersion, hence the red part of the pulse is first incident to the SOA. The temporal gain depletion effect causes stronger amplification of the leading (red) part of the pulse in the temporal domain. The combination of the temporal and spectral effects tends to more strongly amplify only the red portion of the pulse and therefore limits the attainable bandwidth of the mode-locked spectrum. For the generated up-chirped pulses, the mode-locked laser output spectrum is no broader than approximately 3 nm.

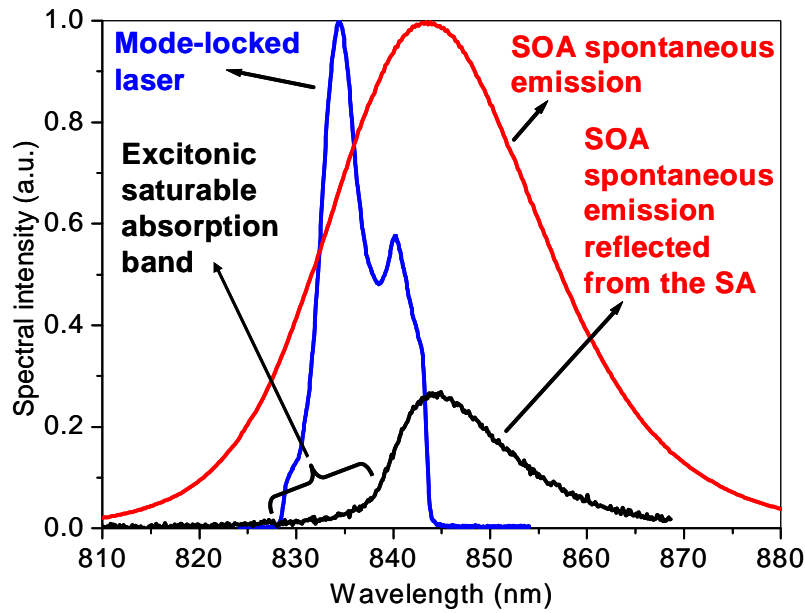


Figure 35: The wavelength position of the SOA spontaneous emission spectrum, the SA excitonic absorption band and a mode-locked laser spectrum.

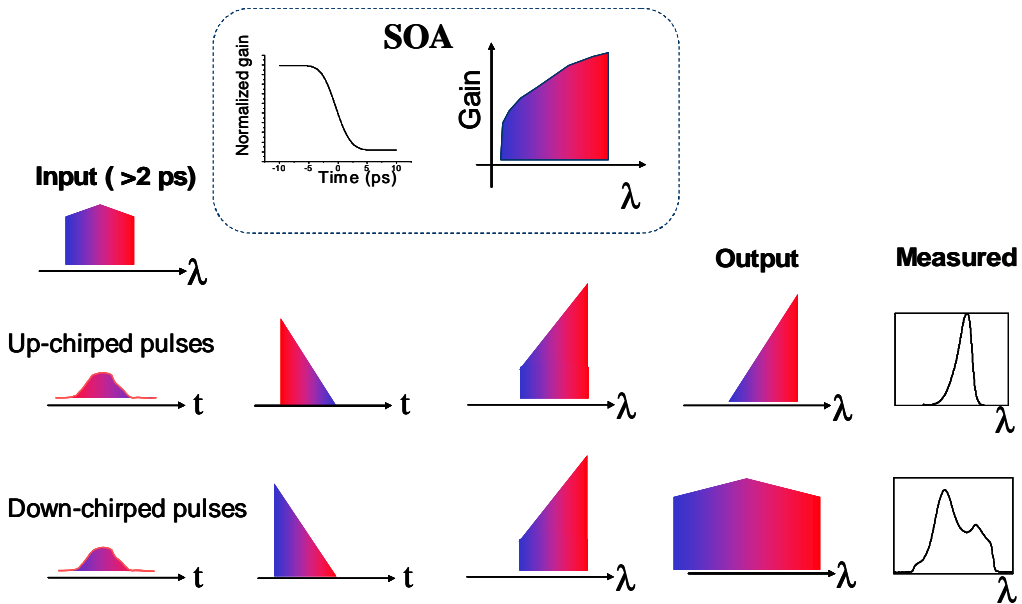


Figure 36: Illustration of the SOA temporal and spectral response to the incident up- and down-chirped pulses.

In the down chirping regime, the amplification in the spectral and temporal domains is balanced. The red part of the pulse experiences higher amplification due to the red shifted laser gain peak, but the blue part is initially passing through the SOA in time and experiences higher gain before the SOA gain depletes. These balanced effects in the temporal and spectral domains allow broadening of mode-locked laser spectra, hence there is a possibility of much shorter pulse generation. This is confirmed experimentally with the following measured results.

It is important to notice that up chirping would be preferable if the SOA gain peak were blue shifted with respect to the SA excitonic absorption band. For the blue shifted SOA gain peak the up-chirped pulses would experience balanced temporal and spectral amplification leading to broader mode-locked spectra and the possibility of shorter pulse generation.

Figure 37 presents the passively mode-locked laser performance for nonbreathing-mode, and breathing-mode in up and down chirping regimes. The externally compressed laser output pulse second-harmonic autocorrelation and spectral FWHM is plotted versus introduced GVD by the dispersion element 2 (stretcher). The presented results are along the diagonal of the maps in Figures 17 and 18 when the same amount of GVD with opposite sign is introduced by the dispersion element 2 (compressor). In the middle of the graph, a small amount of dispersion is introduced to the laser cavity. The laser spectra are narrow, the output pulses are not compressible below durations of 3-4 ps and in this case the laser does not operate in the breathing mode. After introducing sufficient normal (positive) dispersion, of ~ 3.3 ps/nm, mode-locked spectra broaden more than twice and pulses are compressible to approximately 0.5 ps, as shown in the right side of Figure 37. In this case the laser operates in the breathing mode and is in the up chirping regime. However, if sufficient anomalous (negative) dispersion is introduced

to the cavity, approximately -2 ps/nm, spectra broaden up to 6 times and pulses are compressible to much shorter durations, as depicted in the left side of Figure 37. The laser operates in the down chirping regime of the breathing mode.

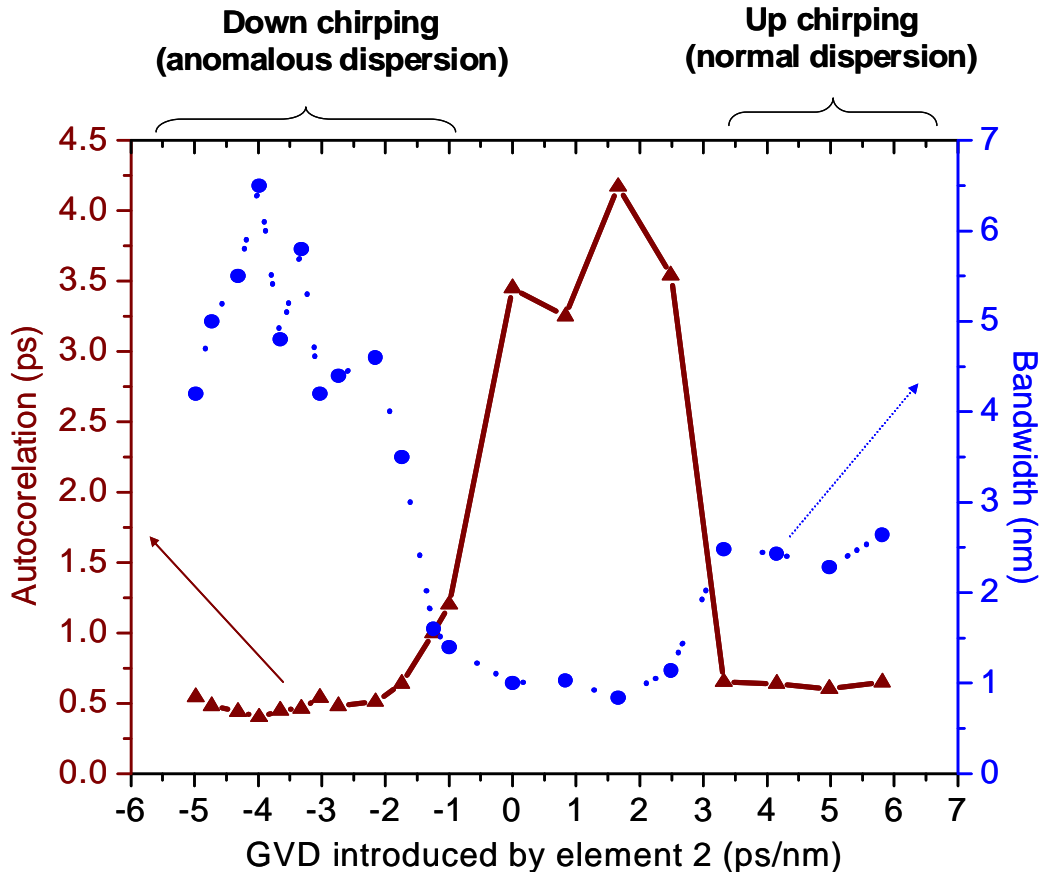


Figure 37: Externally compressed pulse autocorrelation and spectral FWHM versus introduced dispersion by element 2 along the map diagonal.

Clearly, for the dispersion-managed breathing-mode semiconductor mode-locked ring laser there is a great advantage to work in the down chirping regime compared to the up chirping for the red-shifted gain with respect to the SA.

5.3. FROG measured 185 fs pulses from down-chirped dispersion-managed breathing-mode ring laser

In next experiments an additional RF signal is applied to the external cavity SOA in order to achieve higher external cavity amplification as sketched in Figure 38. Both the intracavity and the external cavity SOA are DC biased with 200mA each, and additional RF power of approximately 1 W modulates each of the SOAs at 323 MHz repetition rate.

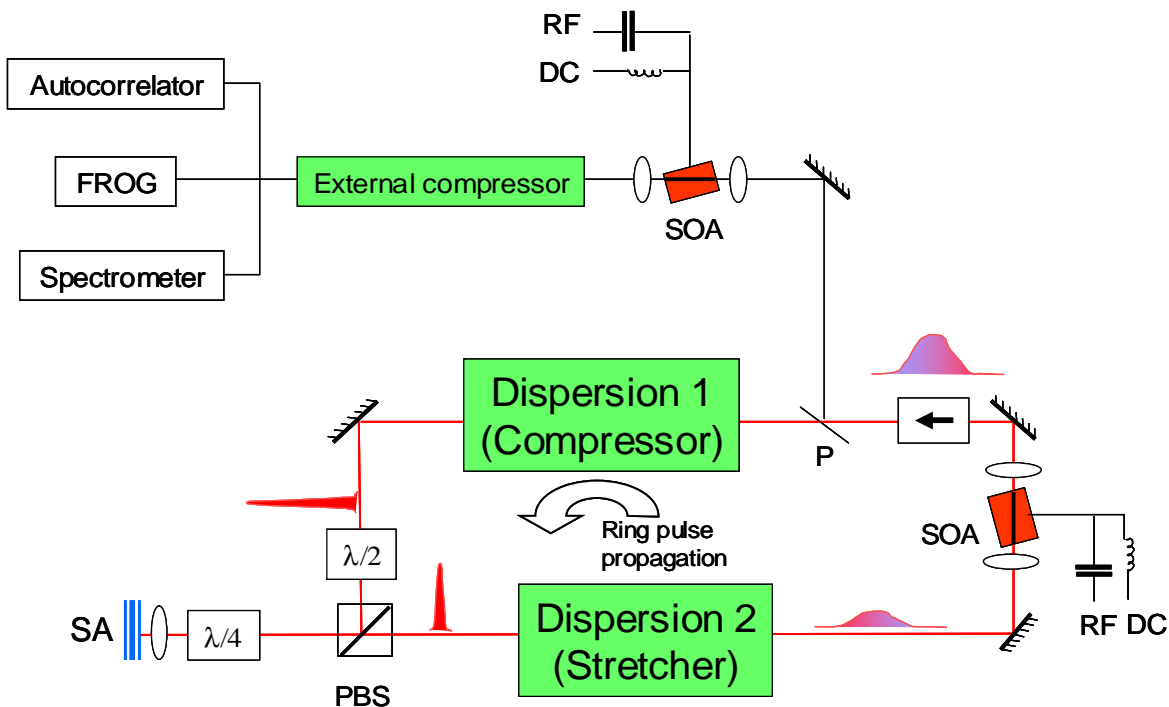


Figure 38: The experimental setup of (bottom) hybirdly mode-locked dispersion-managed breathing-mode semiconductor ring laser and (top) diagnostics with additional RF-modulated external SOA and SHG-FROG pulse characterization.

The RF modulation of the two SOAs is synchronized with an electrical delay line to achieve the highest amplification of the laser output pulse. The highest peak power of the amplified laser output pulse is obtained when the peak of the applied RF sinusoid match with the pulse propagating through the intracavity and external cavity SOA. Approximately twice higher average pulse power was measured with properly RF modulated external SOA when compared to the only DC biased SOA.

Following the external amplification and compression the laser output pulses are characterized with a spectrometer, a second-harmonic intensity autocorrelator and second-harmonic generation frequency-resolved optical gating (SHG-FROG). Since FROG characterization of an ultrafast pulse is advantageous compared to measurements of only intensity autocorrelation and power spectrum, a standard SHG-FROG setup is built in the lab, as sketched in Figure 3(b) and added to diagnostics. The pulse retrieval is performed with commercial software from Femtosoft Technologies.

The principle of the pulse characterization via FROG method is explained previously in Section 2.3. Today, this method is widely accepted in the ultrafast community as accurate, repeatable, robust and relatively simple. Recently, a simplified single-shot version of FROG referred to as GRENOUILLE (grating-eliminated no-nonsense observation of ultrafast incident laser light e-fields) [64] has been commercialized. The FROG method has been extensively used to characterize the ultrashort pulses from solid-state mode-locked lasers. Solid-state ultrafast lasers generate sufficiently powerful pulses that a hybrid method OPA-XFROG (optical parametric amplifier cross-correlated FROG) has been developed with sub femto-joule sensitivity [65]. However, the reported OPA-XFROG setup employs starting high-power pulses with 1 mJ energy and 90 fs duration. Since FROG is based on the detection of the second-

harmonic generated signal, the sensitivity is an issue for lower power laser systems such as mode-locked fiber or semiconductor systems. FROG characterization of the fiber laser pulses have been reported [66] and fiber-based FROG system was recently commercialized by the same group. Semiconductor multiwavelength mode-locked laser was studied via measured SHG-FROG traces [67], and to our knowledge, we report for the first time femtosecond pulse retrieval from a semiconductor mode-locked laser [68].

The measured hybirdly mode-locked laser output autocorrelation is compared with the bandwidth-limited calculated one in Figure 39.

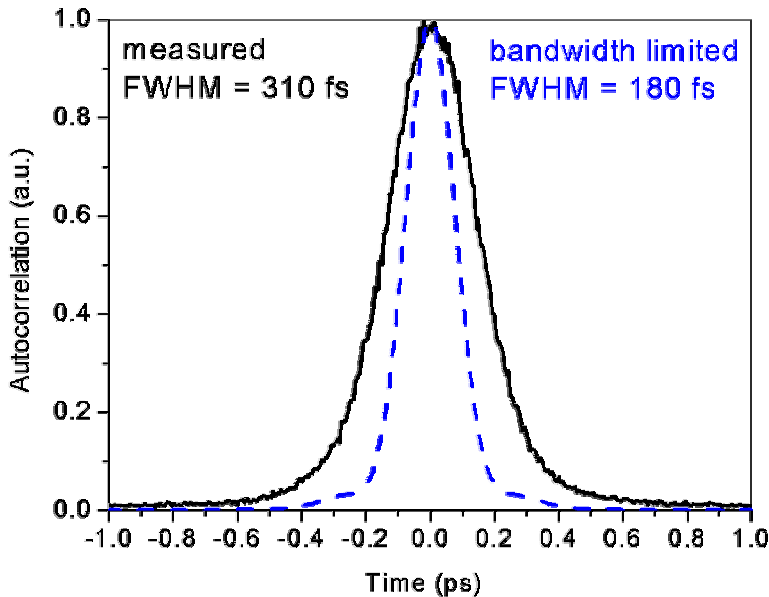


Figure 39: Comparison of the measured (solid line) and calculated bandwidth-limited (dashed) autocorrelation from the externally compressed down-chirped laser output pulse.

The code for the calculation of the bandwidth-limited autocorrelation is attached in the Appendix C. The bandwidth-limited autocorrelation is calculated from the measured hybirdly

mode-locked laser output spectrum presented in Figure 40. As depicted in Figure 39, the measured autocorrelation FWHM of 310 fs is 1.7 times broader than the bandwidth-limited one. The broadened laser output spectrum of FWHM = 9 nm along with the corresponding SHG-FROG retrieved spectral phase shown in Figure 40, is obtained from the down-chirped dispersion-managed breathing-mode ring laser. The SHG-FROG retrieved spectral phase exhibits some higher order dispersion in the compressed pulse. This implies a possibility of even shorter pulse generation with proper higher order dispersion compensation.

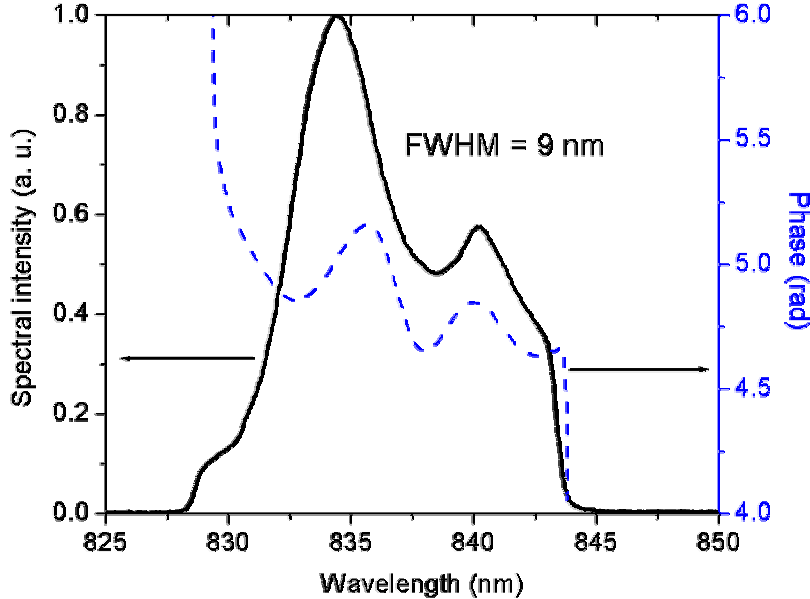


Figure 40: The measured compressed down-chirped laser (solid) spectrum and (dashed) FROG retrieved spectral phase.

Figure 41 displays the measured autocorrelation from the externally compressed down-chirped laser output pulse in log-scale. There are no significant wings in the autocorrelation

suggesting clean pulses with a low amount of cubic spectral phase. The measured signal to noise ratio is at least 20 dB. The measurement is limited by the dynamic range of the autocorrelator.

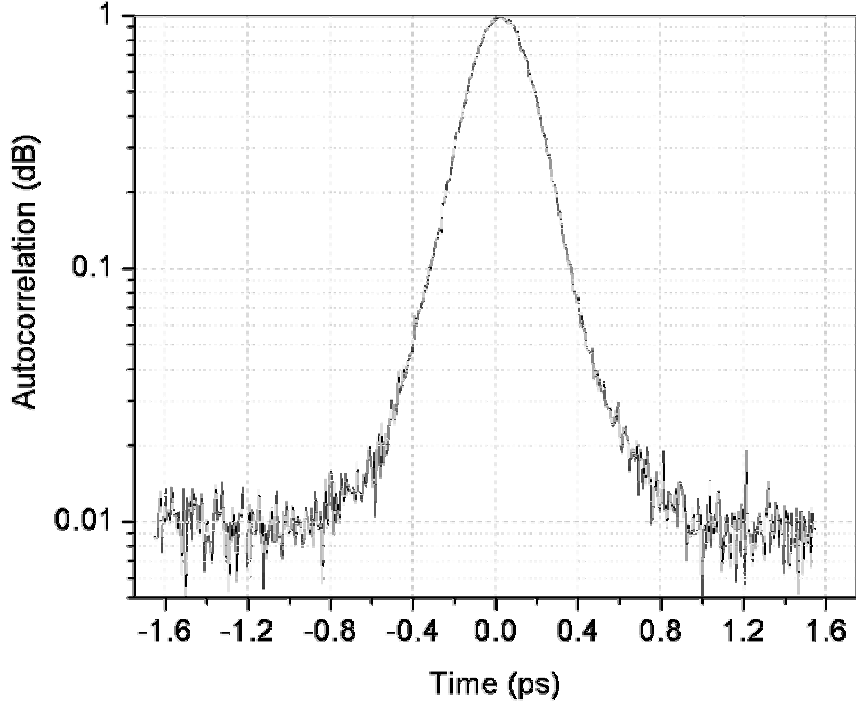


Figure 41: The measured autocorrelation from the externally compressed down-chirped laser output pulse in log-scale demonstrating SNR of 20 dBs.

Figure 42 shows the experimentally measured (left) and retrieved (right) SHG-FROG trace from the compressed down-chirped dispersion-managed breathing-mode semiconductor mode-locked ring laser. The retrieved trace recovers the salient features observed in the experimentally generated trace. The calculated FROG error is 0.006 using a 128x128 grid size. The grid size must be always mentioned, since the FROG error is actually proportional to $1/\sqrt{N}$, where $N \times N$ is the grid size [30]. The SHG-FROG extracted temporal intensity profile and the corresponding phase are depicted in Figure 43.

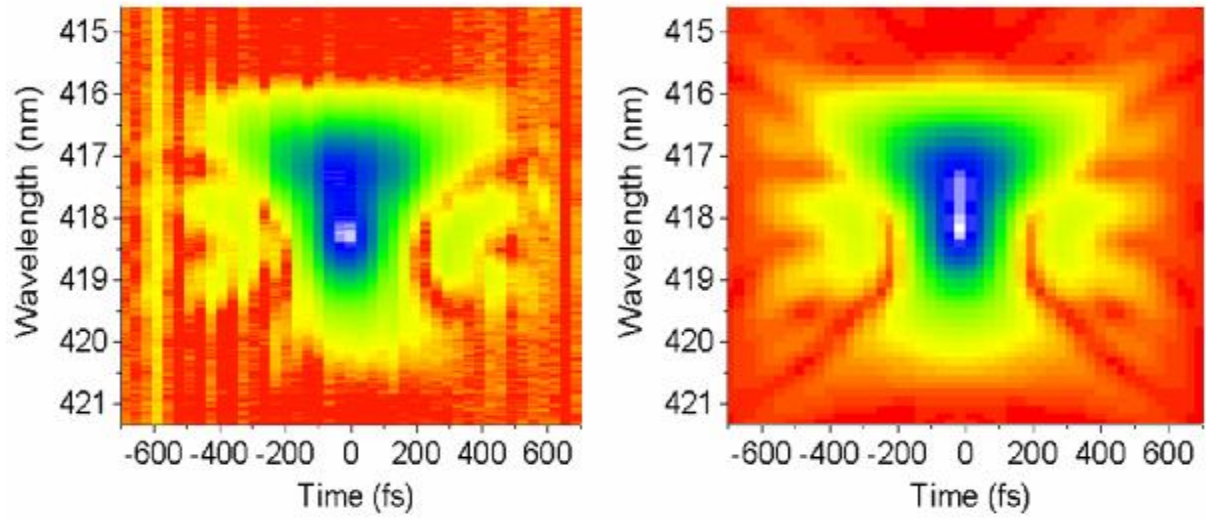


Figure 42: The SHG-FROG (left) experimentally measured and (right) retrieved trace. The FROG error was 0.006 with 128x128 grid size.

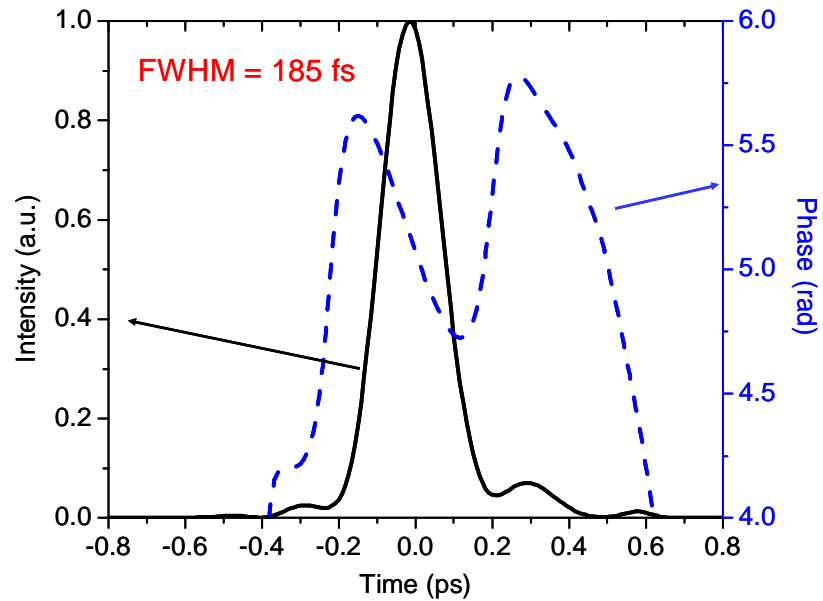


Figure 43: The SHG-FROG retrieved pulse (solid) temporal intensity of FWHM = 185 fs and (dashed) corresponding phase.

The pulse FWHM of 185 fs is achieved. The measured average output power is 14 mW at 323 MHz pulse repetition rate, implying a peak power of approximately 230 W, and a focused intensity of approximately 4.6 GW/cm^2 in a $5 \times 1 \mu\text{m}^2$ spot.

To our knowledge, this is the highest peak-power and the shortest pulse obtained ever from an electrically pumped semiconductor laser. It should be noted that the results are obtained by only linear chirp manipulation, which is important for potential future setup simplicity, repeatability and commercial applications.

5.4. Numerical simulations of the pulse generation by down chirping of the dispersion-managed breathing-mode semiconductor ring laser

In the numerical simulations of the down-chirped dispersion-managed breathing-mode semiconductor mode-locked ring laser the same algorithm and parameters are used as for the numerical simulations of the up-chirped laser described in the Section 4.1, except the introduced GVD and the spectral filter. The intracavity introduced GVD is +1.09 and -1.10 ps/nm for the element 1 (compressor) and 2 (stretcher), respectively. The introduced GVD has the opposite sign and a smaller amount in the case of down chirping when compared to the up chirping case. It is producing a similar amount of the pulse temporal broadening for the three times wider spectral width inside the laser cavity.

The new spectral filter profile is illustrated in Figure 44. The new spectral filter exhibits asymmetric profile of FWHM = 13.4 nm featuring higher transmission in the red part of the pulse spectrum. The filter edges are cosine function edges and the middle part is a linear

function with a slope of 20% increase, representing approximately the slope in the SOA spontaneous emission spectrum along the down-chirped laser mode-locked spectrum (see Figure 35). Such an asymmetric spectral filter accounts for the stronger amplification of the red part of the down-chirped pulse in the spectral domain. The stronger spectral amplification of the red pulse part is balanced with the stronger amplification of the blue (leading) pulse part in the temporal domain leading to the broader mode-locked spectrum generation, as discussed in the Section 5.2.

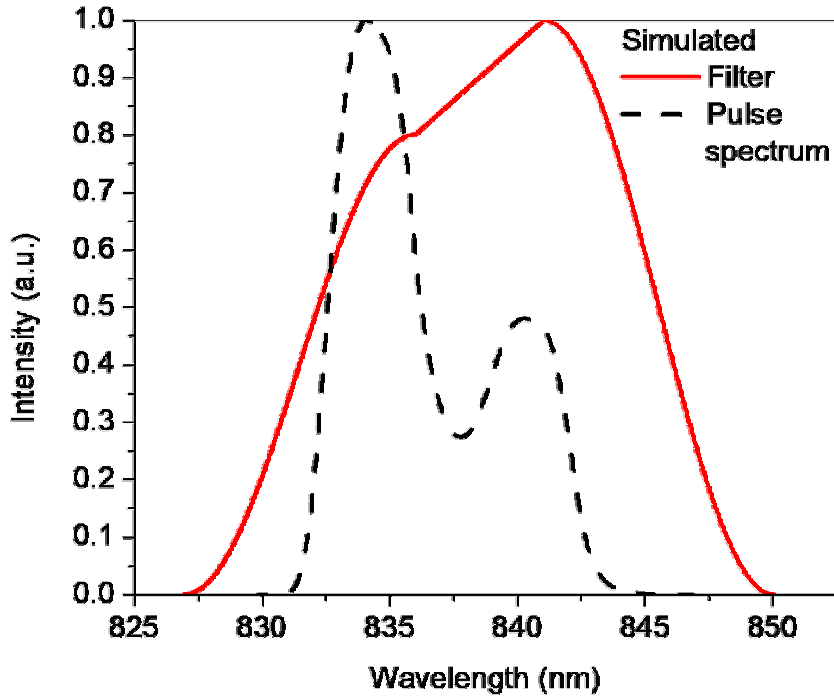


Figure 44: The simulated (solid) spectral filter of FWHM = 13.4 nm and (dashed) the normalized steady-state output pulse spectrum after the gain media.

The build-up of the mode-locked pulse spectrum after the gain SOA for down-chirped laser is presented in Figure 45. The laser evolves from the input random noise to a steady-state

mode locking solution in approximately 350 cavity round trips as was the case in the up chirping laser operating regime.

The steady-state pulse spectral intensity after 600 simulated cavity round trips is compared with the measured pulse spectrum as shown in Figure 46. Both spectra exhibit the same trend. They feature two peaks originating from the balance of amplification in the spectral and temporal domain, with the higher blue peak. The spectra are normalized and the simulated spectrum is shifted up to the level of the spontaneous emission background in the measured spectrum. The measured spectrum is clipped with a slit in the external compressor Fourier plane.

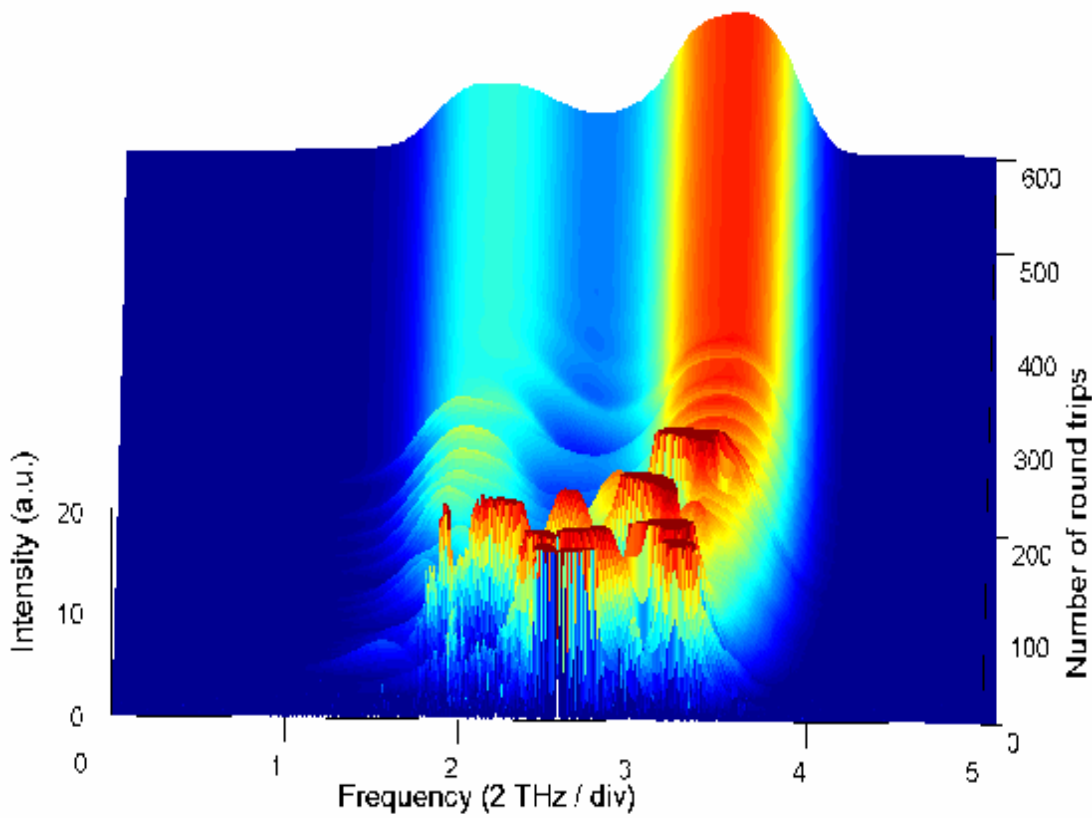


Figure 45: Simulated formation of the mode-locked stretched pulse spectral profile after the gain media in the down chirping regime of the breathing mode.

On the blue side of the spectrum, the slit removes the amplifier SOA spontaneous emission background. On the red side of the spectrum, the external compressor slit removing amplifier spontaneous emission matches with the intracavity compressor slit preventing the CW lasing caused by the stronger laser gain towards the red.

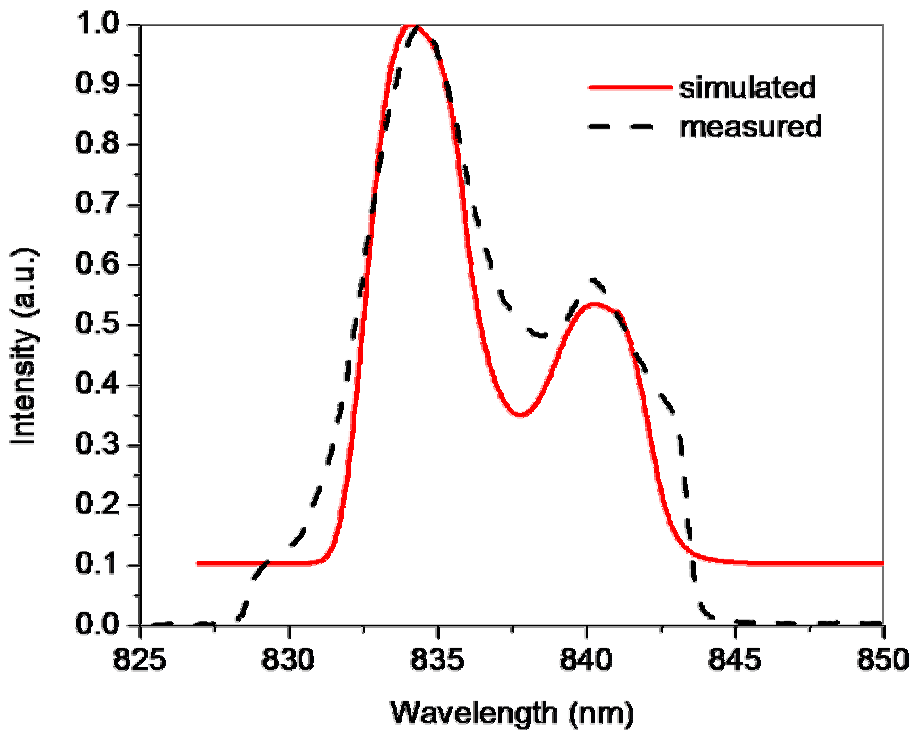


Figure 46: Comparison of (solid) the simulated and (dashed) the measured stretched pulse spectrum after the SOA.

The steady-state simulated compressed pulse temporal intensity after the gain SOA is compared with the corresponding pulse retrieved by the SHG-FROG method (see Figure 43 and the description in the previous Section) as presented in Figure 47. The temporal grid in the

simulations has a pixel size of 100 fs. Although the simulated pulse is not sufficiently sampled, a very good agreement between the simulated and the SHG-FROG retrieved pulse is observable.

It should be mentioned that with the new filter profile only by switching the signs of the introduced GVD in the compressor and the stretcher, the steady-state solution for the up-chirped dispersion-managed breathing-mode semiconductor mode-locked ring laser is obtained. This confirms that the physical mechanisms involved in the pulse shaping are properly included in the developed numerical model for both up and down chirping laser operating regimes.

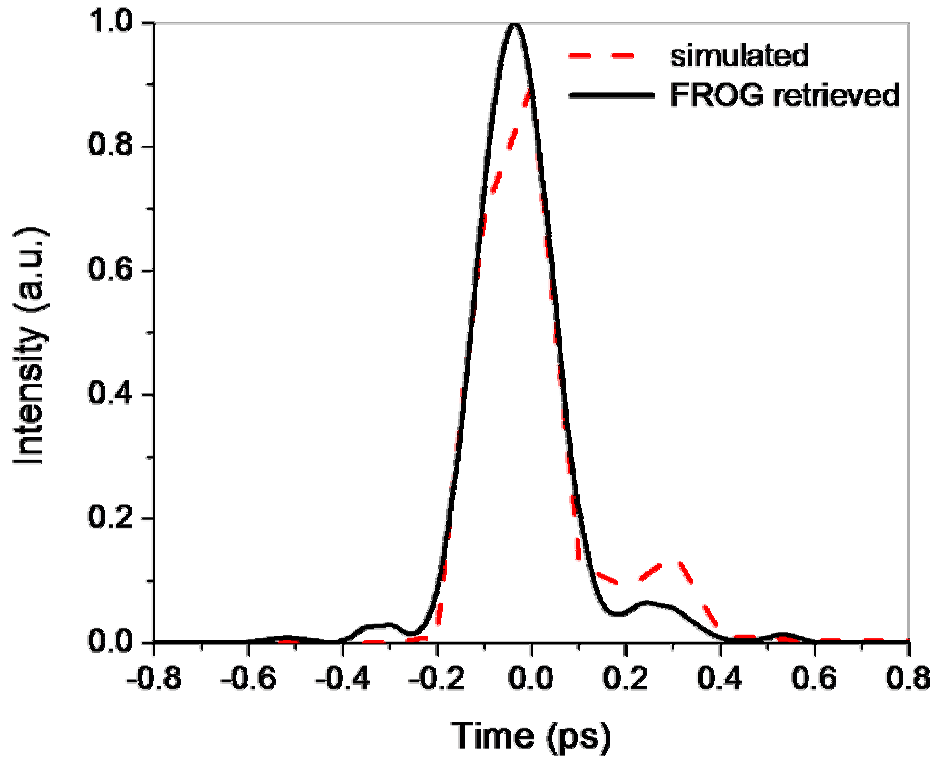


Figure 47: Comparison of (dashed) the simulated and (solid) the FROG retrieved compressed pulse temporal intensity.

The numerical simulations predict an additional very important feature. The steady-state solutions with broader mode-locked spectra are obtained by opening the spectral filter width. This suggests that with broader bandwidth SAs and/or SOAs or by shaping the laser gain through the dispersion adjustments, one can achieve broader mode-locked spectra and generate shorter pulses.

CHAPTER 6: APPLICATION TRENDS

6.1. Continuum generation via photonic crystal fiber

It is a great achievement to develop a novel laser. However, this laser can only be referred to as an exotic laser if it does not find a use or an application in the real world. In this chapter, we will discuss some of the paths which could be pursued for possible applications of our novel dispersion-managed breathing-mode semiconductor mode-locked laser.

The semiconductor media has relatively narrow gain bandwidth when compared to some solid-state crystals. Our SOA device emitting around 830 nm has spontaneous emission spectral FWHM of 25 nm (see Figure 6) and e.g. Ti:Sapphire has bandwidth of hundreds of nanometers. This is a serious inherent obstacle in efforts to generate pulses as short as possible from semiconductor media. Even more, the mode-locked spectra from the semiconductor laser do not extend more than approximately 10 nm for the “nice and clean” mode locking generating pulses compressible below 500 fs. Therefore, some additional tricks are needed inside or outside the semiconductor laser cavity to broaden the spectrum significantly beyond 10 nm and generate pulses much shorter than 150 fs.

For a long time researchers were experimenting to broaden laser spectra outside the laser cavity via nonlinear effects such as the SPM, four-wave mixing (FWM), Raman scattering and

others, to generate a broad continuous spectrum usually referred to as supercontinuum. The supercontinuum generation in crystals and glasses was first reported in 1970 by R. R. Alfano and S. L. Shapiro [69]. Soon, it was realized by R. Stolen [70] that supercontinuum is possible to generate in silica fibers what opened wide range of possibilities in fiber optics applications. Extensive earlier work in supercontinuum generation was described in the book by R. R. Alfano [71]. A new wave in optics arises with the development of photonic crystal fibers (PCFs) [72]. Owing to the enhanced nonlinearities in the PCF, supercontinuum is attainable with much shorter fiber lengths (in centimeters) using high-power solid-state lasers or longer fiber lengths using low-power lasers [73]. Extensive study of supercontinuum performance and noise was recently reported by many groups (e.g. [74]-[77]). Due to the low output power and low coupling efficiency caused by the mode-mismatch, continuum generation with semiconductor lasers has yet to be reported. A logical extension of our work is to pursue continuum generation with our novel high-power semiconductor mode-locked laser.

Figure 48 sketches the experimental setup for supercontinuum generation using the dispersion-managed semiconductor mode-locked ring laser and the PCF. The commercially available silica PCF from Blaze Photonics (University of Bath, UK) is used in the experiment. The scanning electron microscope (SEM) image of the PCF cross-section is presented in Figure 49. It consists of a silica core surrounded by air holes. The important properties of the PCF are listed in Table 2. The typical focusing lens (Melles Griot model 06GLC002 with NA of 0.5) is used for coupling the light into the PCF. The semiconductor laser output beam profile is single spatial mode, but highly elliptical (typically 8 mm high and 2 mm wide) and the beam is astigmatic. Due to such a semiconductor laser beam, without additional beam correction optics the mode mismatch with the fiber limited the coupling efficiency to 15%, e.g. more than 30%

coupling efficiency of the He-Ne laser output beam to the PCF was easily obtained. The output broadened spectrum after the PCF is measured with the optical spectrum analyzer model ANDO AQ6317B, with dynamic range up to 70 dB and resolution of 0.1 nm.

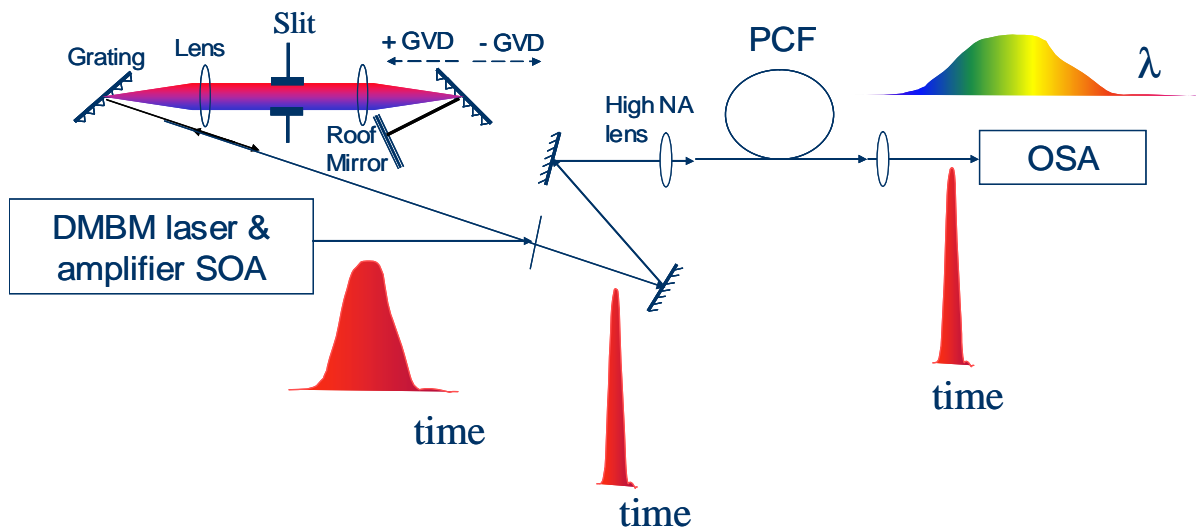


Figure 48: Experimental setup for supercontinuum generation and detection. DMBM laser – dispersion-managed breathing-mode laser, PCF – photonic crystal fiber, and OSA – optical spectrum analyzer.

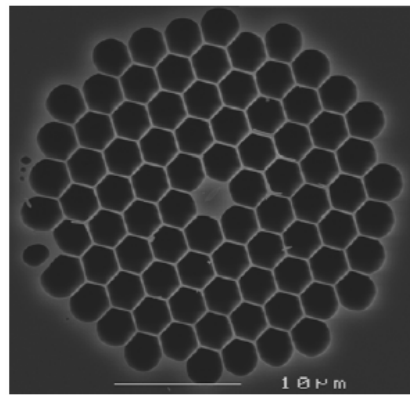


Figure 49: The SEM image of the PCF cross-section.

Table 2: Important properties of the PCF used for continuum generation.

Property	Value
Core diameter	2.8 μm
Nonlinear coefficient	$50 \text{ W}^{-1}\text{km}^{-1}$
Numerical aperture	0.32
Zero dispersion wavelength (λ_0)	841 nm
Loss at λ_0	37 dB/km
Dispersion slope at λ_0	0.58 ps/(nm ² km)

The breathing-mode semiconductor laser output spectrum and the pulse autocorrelation after external amplification and compression, prior to coupling into the PCF are presented in Figures 50 and 51. The laser pulse repetition rate is increased to 0.5 GHz in order to enhance the number of signal photons. The input spectrum to the PCF has sharp edges and FWHM of 8 nm. A slit is used in the external compressor to sharpen the edges of the input spectrum into the PCF. The slit removes the amplified spontaneous emission noise from the amplifier SOA and enhances the visibility of the broadened spectral wings in the output spectrum from the PCF.

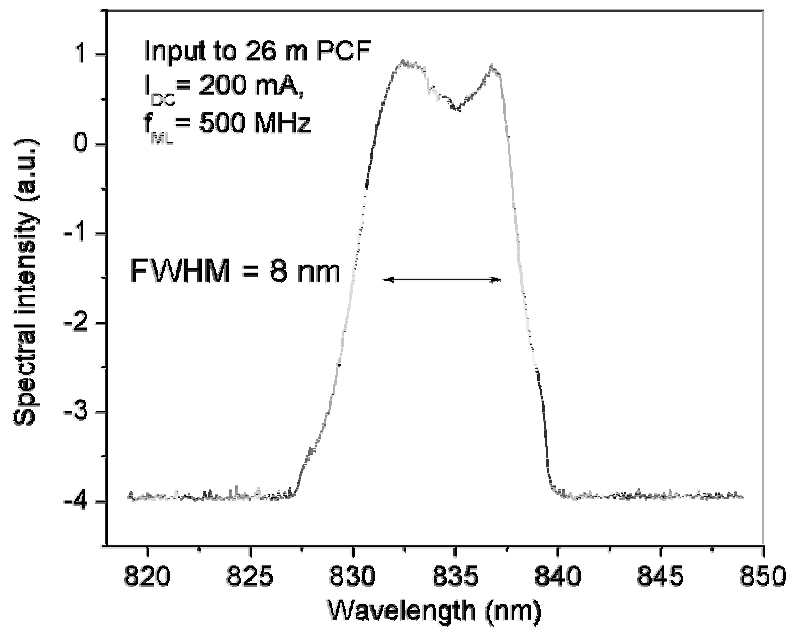


Figure 50: Laser output spectrum after amplification and compression, incident to the PCF.

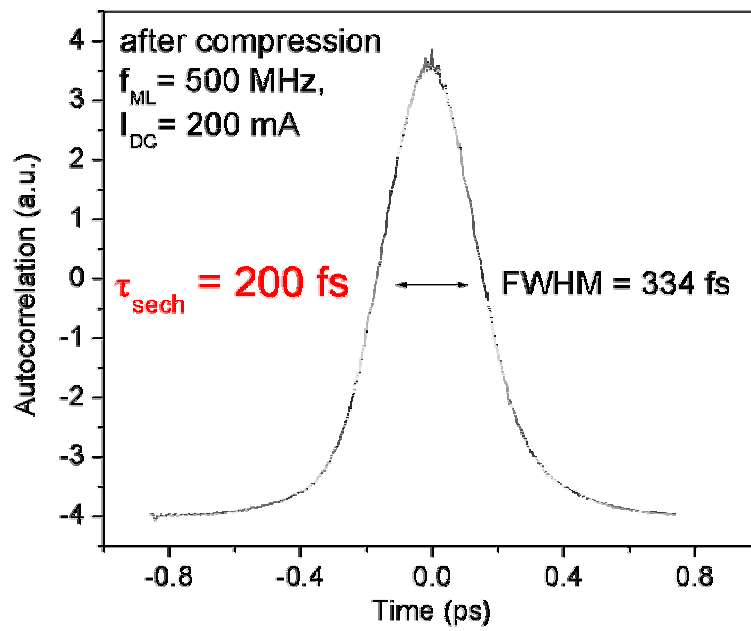


Figure 51: The autocorrelation of the compressed laser output pulse incident to the PCF.

The autocorrelation demonstrates clean input pulses without significant wings, with pulse FWHM of 200 fs assuming sech^2 pulse profile. The laser output average power of 1 mW is efficiently amplified to 22 mW by the amplifier SOA. The amplifier SOA is DC-biased with 200 mA and the RF power of 1 W is applied at 0.5 GHz. After the external cavity compressor with the slit, an average pulse power of 10 mW is incident to the PCF. The output average power from the PCF is 1.2 mW.

The output spectrum from the 1 meter piece of the PCF is compared with the input laser spectrum in Figure 52. The output spectral peak power is normalized to match the peak power of the input spectrum for clarity. The real output spectral peak level could be inferred from the noise level, which is the same for both spectra. The nonlinear spectral broadening is clearly observable in the wings, but it is still 27 dB below the peak spectral power.

The accumulated nonlinear phase shift causing the spectral broadening is proportional to the pulse propagation length through the nonlinear media, or in our case to the fiber length. Therefore, to enhance the spectral broadening the simplest solution is to increase the length of the fiber. However, the fiber length could not be increased infinitely because the fiber loss at some point decrease significantly the pulse peak power, the fiber dispersion broadens the pulse again decreasing the peak power, but also the expense for the fiber becomes high. In the next step, the spectrum is measured for a 26 meters long piece of the same type of PCF. The calculated loss is 1 dB and the pulse broadening due to dispersion is measured to be approximately 200 fs, both of which do not decrease the nonlinear interaction significantly. The 26 meters long PCF spectral response is plotted in Figure 53. Significant spectral broadening is observed after the PCF.

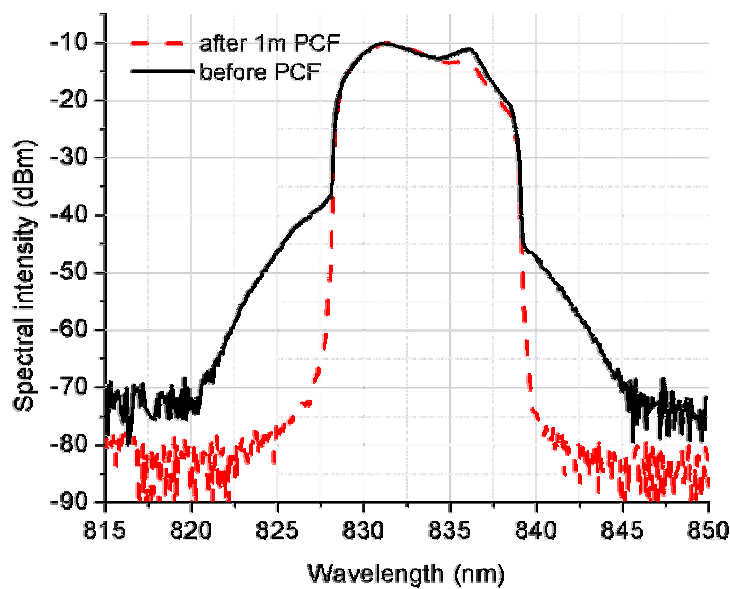


Figure 52: Comparison of the laser pulse spectra before and after 1 m long PCF.

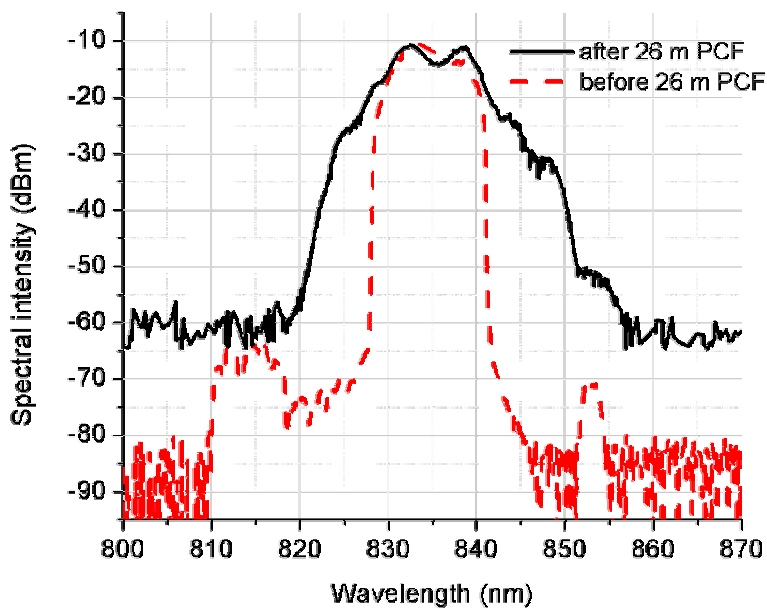


Figure 53: Comparison of the laser pulse spectra before and after 26 m long PCF.

The spectrum broadens approximately 5 nm within 10 dBs below the peak power and 40 nm before reaching the noise floor. A blue-shifted and a weaker red-shifted peak are observable in the input spectrum. They are 55 and 60 dBs below the spectral peak power, hence not influencing measurement results and can be addressed to the weak nonlinear interaction in the single mode detection fiber guiding the light to the optical spectrum analyzer.

Significantly broader spectra after 26 meters long PCF compared to the 1 meter long piece suggest that the experiments should be continued with longer fiber lengths to generate broader supercontinuum. With the longer fiber, the accumulated nonlinear phase would dominate the fiber loss and the pulse broadening due to the dispersion and broader coherent spectra could be achieved. Today the PCF fabrication techniques are progressing rapidly decreasing the losses and costs of the fiber. This will allow the feasibility of longer PCF with better performance and lower cost. The broadened coherent spectra from the nonlinear fiber could be subsequently amplified with an additional SOA. The broad high-power coherent spectra from the compact and efficient semiconductor laser and the PCF are highly desirable in many applications such as biomedical imaging, WDM in telecomm, metrology, and nonlinear spectroscopy to name a few.

6.2. Two-photon fluorescence imaging

One of the remarkable applications of the two-photon fluorescence effect is in the nonlinear imaging of various biomedical tissues [78]. The nonlinear biomedical imaging is one of the most rapidly growing areas of optics today [79]. However, the wide consumer market is

still not reached because it is usually performed with costly and sizable high-power solid-state lasers systems. Our novel developed high-power femtosecond semiconductor laser could play a significant role in this area. The operating wavelength of 830 nm matches closely the operating wavelength 800 nm of the Ti:Sapphire laser most commonly used in this area. Thus, in developed optical instruments, like the two-photon microscope, one can eventually replace the solid-state laser source with the semiconductor laser. Additionally, a wide variety of the chemical molecules are engineered for enhanced two-photon fluorescence around an 800 nm source wavelength.

A simple experiment can demonstrate the potential of our laser system for two-photon fluorescence imaging as sketched in Figure 54. The dispersion-managed breathing-mode semiconductor laser output pulses are amplified and externally compressed as in the previous experiment of continuum generation with the PCF.



Figure 54: Schematic of the experimental setup for two-photon fluorescence observation.

The same laser operating parameters are employed as described in the previous section and the laser system output spectrum and pulse autocorrelation are similar to ones presented in Figures 50 and 51. The semiconductor laser system output is focused in an organic dye sample with a typical lens of 0.5 numerical aperture. The organic dye sample with the enhanced two-photon fluorescence was prepared by the group of Prof. Kevin Belfield from the University of

Central Florida Chemistry Department [80]. The salient part of the organic dye is a fluorene derivative as shown in the Figure 55. It is a diphenylamine, 7-benzothiazol-2-yl-9, 9-didecyl-fluoren-2-yl. The organic dye is solidified on a microscopic plate for easier handling.

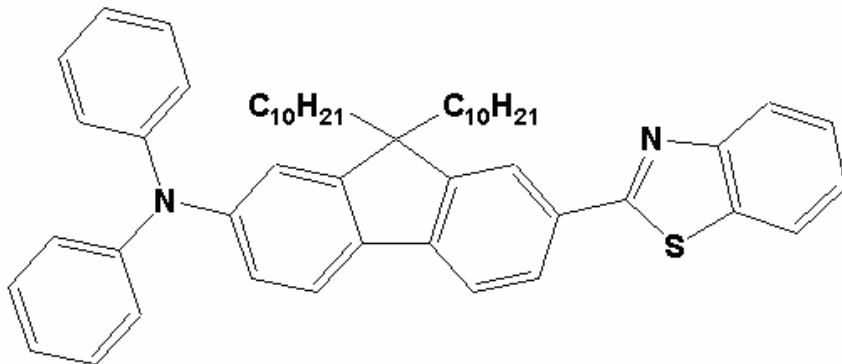


Figure 55: The chemical structure of the organic dye sample.

Although the two-photon absorption of the sample is optimized for 400 nm, the Ti:Sapphire wavelength, the sample exhibits absorption at 417 nm and strong fluorescence as shown in Figure 56. The photos of the blue light are taken with a low sensitivity commercial digital camera for home use. On the right photograph (zoomed out the left photograph) in the Figure 56 it is clearly observable two-photon fluorescence blue light from the sample on the microscopic plate.

This experiment demonstrates that our semiconductor laser system is sufficiently powerful to activate two-photon fluorescence from a typical organic dye sample used in the two-photon microscopy. It verifies the possibility of the dispersion-managed breathing-mode semiconductor laser system for two-photon laser scanning microscopy, where each point is scanned and imaged. To extend this further, the laser system could be tested for the possibility

of two-dimensional, single-shot imaging with a commercial two-photon fluorescence microscope.

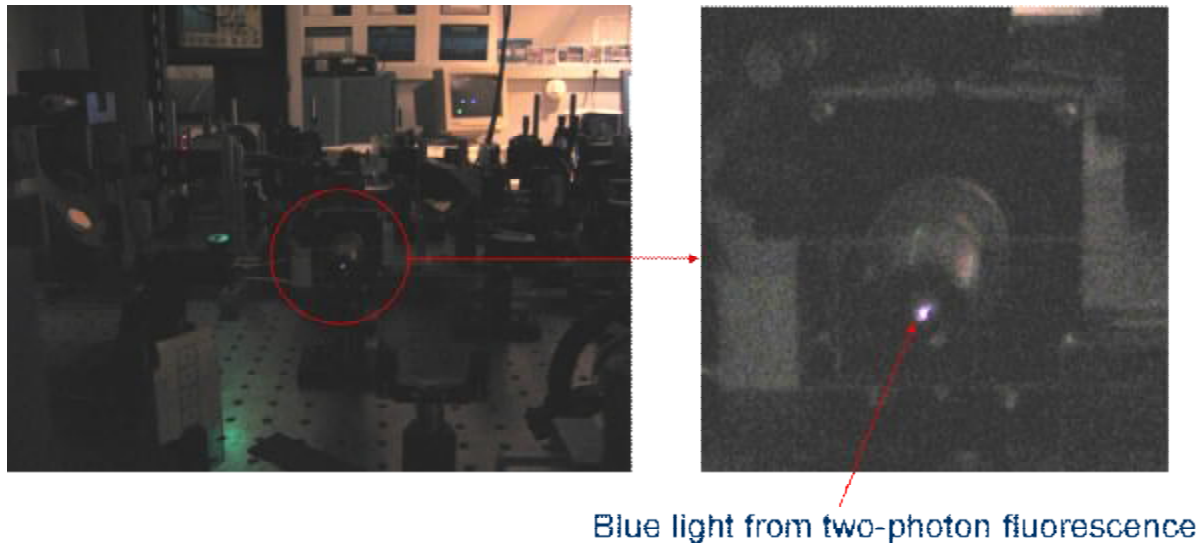


Figure 56: Photograph of the two-photon fluorescence from the organic dye sample. The right photograph is zoomed out part with the blue light from the left photograph.

6.3. Ultrashort pulse source for pump-probe experiments

The investigation of any kind of ultrafast phenomena in nature requires an ultrafast laser pulse source, since electronics and other technologies are too slow to measure effects on the femtosecond time scale. The pump-probe technique is a very powerful method to measure response of the material on the fs-scale [81]. A series of very elegant pump-probe experiments were performed to measure the fs-scale response of the SOAs [82]. The SOA and the SA fs-scale behavior were measured while they mode-lock a semiconductor laser [67], [15]. Recently,

semiconductor laser mode locking was demonstrated in the multiwavelength operating regime [83], [4]. The multiwavelength mode-locked semiconductor lasers are light sources with the great potential in the future WDM optical networks [84]. Therefore, it is of great importance to study how a single SOA supports simultaneous multiwavelength mode locking.

The time resolution of a pump-probe experiment is determined by the pulse duration of the ultrafast laser used as a pulse source. Traditionally the Ti:Sapphire laser was employed in the pump-probe experiments as the commercial source of the fs-pulses. However, one prefers to save money and space for the main part of the pump-probe experiment and use a compact, cost-effective fs-pulse source. In our pump-probe experiment the novel developed dispersion-managed breathing-mode semiconductor mode-locked laser is employed as the fs-pulse source.

The SOA ultrafast gain dynamics is studied for the input ultrafast multiwavelength pulses. The experimental setup is illustrated in Figure 57. The device under test is a 0.35 mm long, angle-striped and AR-coated SOA biased at a constant current of 200 mA. The dispersion-managed breathing-mode semiconductor ring laser is operating in the up chirping regime generating pulses as presented in Figure 34 and spectrum as in Figure 20(a). Most of the laser power is used for the pump beam and a small portion of 10% is used for the probe beam. The probe pulse duration is compressed to ~ 300 fs using a dual-grating dispersion compensator in the probe optical path. The probe beam polarization is rotated 90 degrees and a variable filter is employed to adjust its power. A variable delay station is used to delay the probe pulse with respect to the pump pulse. The pump pulse is obtained by passing the laser output pulses through a second dual-grating dispersion compensator. In the second compressor the linear chirp is compensated and additionally, the spectrum is filtered to generate 3 wavelength channels of approximately 0.5 nm FWHM each, with a 1.4 nm channel to channel separation.

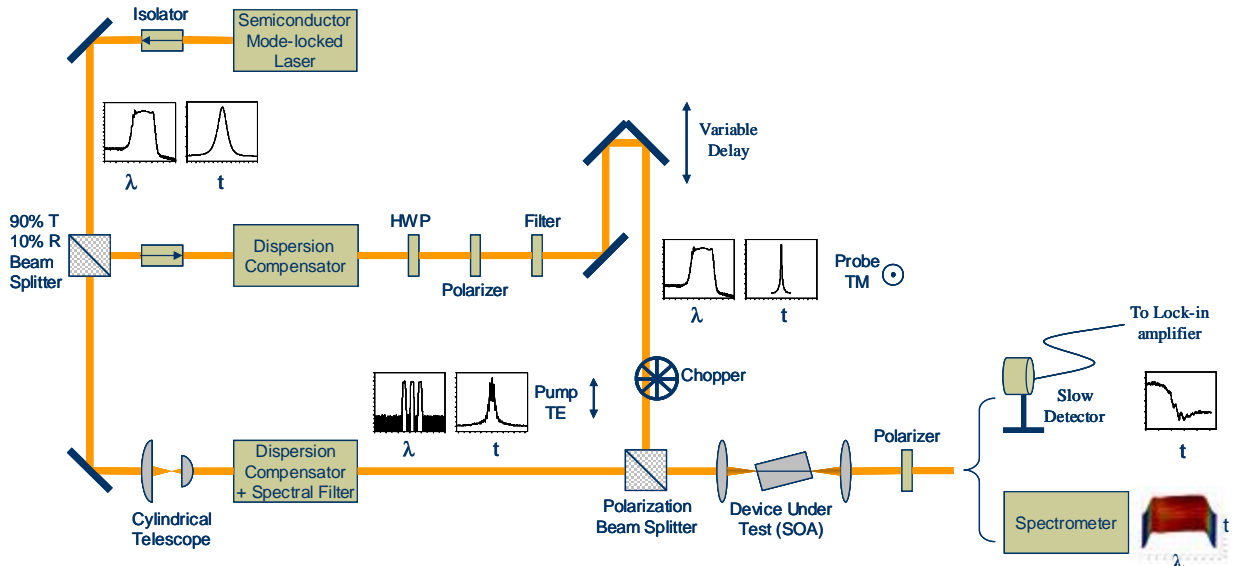


Figure 57: The experimental layout of the pump-probe experiment studying the SOA gain dynamics for input ultrafast multiwavelength pulses.

The spectral filtering of the pump beam into three phase-correlated wavelength channels generates the temporal profile of a burst of short pulses under a broad envelope. The temporal duration of a single pulse within the pulse burst is inversely proportional to the full spectral width encompassing all the wavelength channels, while the temporal duration of the pulse burst envelope is related to the spectral bandwidth of a single wavelength channel. The separation between pulses within the pulse burst is related to the separation between wavelength channels.

The pump and the probe beams are recombined and coupled into the SOA under test. The amplified probe beam power is measured as a function of the delay between the pump and the probe pulse. The strong pump pulses induce changes in the gain of the SOA. The short probe pulses are sufficiently weak in order not to induce significant changes in the gain. The probe pulse carries the information about the gain changes originated by the pump pulse as a

function of the delay between pump and probe. The crossed polarization of the pump and the probe as well as lock-in detection techniques are used to distinguish the probe pulse from the pump pulse after being amplified by the SOA under the investigation.

In Figure 58 a net reduction in the gain due to stimulated emission is observed for time delays larger than 5 ps, with a recovering time on a nanosecond scale, as explained in Figure 2. In addition, for delays between -1.5 ps and 1.5 ps, a rapid variation of the gain is measured which is caused by the periodic temporal nature of the phase-coherent 3 wavelength ultrafast pulse burst. These transients are related to two photon absorption (ultrafast gain depletion) and the relaxation of hot carriers generated by two photon absorption (ultrafast gain recovery).

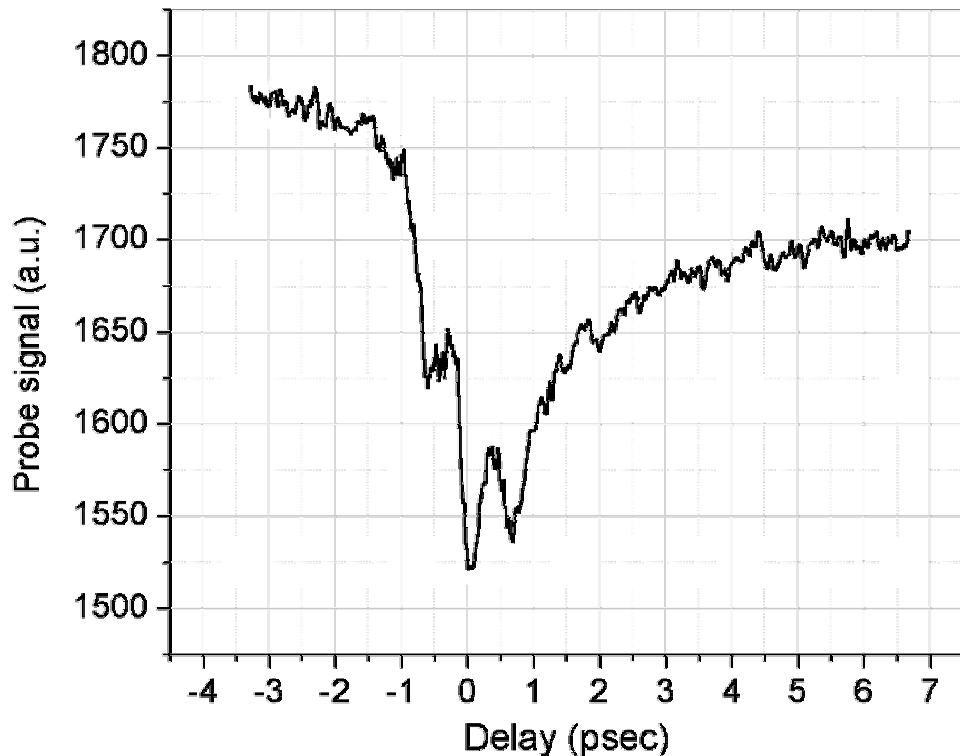


Figure 58: The fs-scale time resolved gain dynamics of the SOA amplifying multiwavelength ultrafast pulses.

The spectrally-resolved pump-probe measurements of the SOA ultrafast gain dynamics for multiwavelength input pulses are conducted to support our understanding of underlying principles governing the multiwavelength laser operation from a single diode system [85]. This ongoing project conducted principally by my lab-coworker Luis Archundia, is continuing to include the time- and spectrally-resolved pump-probe experiments on the intracavity SOA and the SA while they are mode locking the multiwavelength semiconductor laser.

The pump-probe experiments verify the stability, robustness and repeatability of our dispersion-managed breathing-mode semiconductor mode-locked ring laser. It demonstrates its ability to perform and potentially replace a commercial ultrafast pulse laser as a pulse source in some research areas.

CHAPTER 7: CONCLUSION AND FUTURE WORK SUGGESTIONS

7.1. Summary and conclusion of the dissertation

The goal of this research was to develop a state-of-the-art ultrafast electrically pumped all-semiconductor laser system exploiting the inherent compact and efficient nature of semiconductor media and generating ultrashort high power pulses. As well as an interesting scientific challenge that motivated this research, there is an actual strong commercial drive originating from the lack of compact and efficient ultrafast sources in many research and application areas. The cost and size of the Ti:Sapphire laser as a typical high-power ultrashort pulse source inhibit the progress in various scientific and industrial areas. Based on the extensive knowledge about ultrafast physical effects in semiconductors, our intention was to build, simulate and test a semiconductor system that may replace the Ti:Sapphire laser in some of applications.

Previous measurements [1], [53] demonstrate that for incident sub-picosecond pulses, semiconductor media is a less efficient amplifier and impresses highly nonlinear chirp along the propagating pulse. Both of these detrimental effects are suppressed by stretching the propagating pulse through an SOA to duration of more than approximately 5 ps. However, bleaching of the SA requires high peak power ultrashort pulses. To adjust the pulse widths appropriately for both

the SOA and the SA, dispersion management is introduced in the ring laser cavity allowing the laser to operate in the breathing-mode regime. The breathing-mode designates the regime of the laser operation when the pulse width alternates while circulating within the laser cavity. The ring laser generates mode-locked compressible pulses when the intracavity introduced dispersion is compensated, along the diagonal of the dispersion maps. The crosscorrelation measurements at the four key laser cavity points demonstrate that the ring laser is operating in the breathing-mode alternating the pulse width more than 30 times within the cavity.

The numerical simulations are developed to confirm our understanding of the breathing-mode semiconductor laser operation. The mode locking build-up from input random noise in the dispersion-managed semiconductor ring laser is simulated. The very good agreement is obtained between the simulated results and the experimentally measured results. The saturable gain and absorption of the SOA and the SA, respectively, as well as the dispersion management and the decreased SPM are the key physical mechanisms governing the mode-locked pulse evolution and shaping within the ring laser. Additionally, the numerical simulations of the laser injection locking are predicting the fast laser lock-up to the external input pulses.

The breathing-mode ring laser can operate in the up chirping or down chirping regime. In the up chirping regime pulses are stretched by introducing normal dispersion and are externally compressed to a duration of 274 fs which is within 10 % of the bandwidth limit. For the red-shifted SOA gain peak with respect to the SA excitonic absorption band, as it is in our case, the down chirping regime is preferable. In the down chirping regime of the breathing mode laser pulses are stretched by introducing anomalous dispersion. In this case, the stronger amplification of the leading blue part of the pulse in the temporal domain is balanced with the stronger amplification of the red part of the pulse in the spectral domain. The balancing of

amplifications of red and blue parts of the pulse spectrum allows broadening of the mode-locked spectrum and generation of shorter pulses. The spectral width of 9 nm is achieved by down chirping compared to 3 nm by up chirping. The externally compressed down chirped pulses are characterized with a home made SHG-FROG setup. The FROG algorithm retrieved pulse duration of 185 fs. At the pulse repetition rate of 323 MHz the measured average power of 14 mW corresponds to pulse peak power of 230 W and focused intensity of 4.6 GW/cm². To our knowledge this is the shortest pulse and the highest peak power generated from a semiconductor system achieved by only linear chirp manipulation.

There are a wide variety of directions to investigate the applications of the novel developed high power ultrashort semiconductor laser. Significant coherent spectral broadening is achieved by coupling the laser output pulses to the photonic crystal fiber. The measurements imply that with the longer PCF, coherent continuum generation with a semiconductor laser is feasible. The two-photon fluorescence is observed by focusing the laser output to the organic dye sample. This is an important step towards two-photon microscopy with a semiconductor laser as a light source. The laser is successfully used as an ultrafast pulse source in a pump-probe measurement of the ultrafast SOA gain dynamics for the multiwavelength mode-locked pulse input.

In conclusion, a novel semiconductor laser system is developed, and referred to as a dispersion-managed breathing-mode semiconductor mode-locked ring laser. The dispersion management allows for favorable pulse widths in the SOA and the SA to be efficiently amplified by using the chirped pulses and decreasing the detrimental SPM. The proper choice of the up or down chirping based on the wavelength position of the SOA and the SA additionally broadens the mode-locked spectrum. The SHG-FROG method is used to characterize the generated pulses

revealing the pulse duration of 185 fs and peak power of 230 W, to our knowledge the shortest and the highest peak power pulses from a semiconductor system obtained by only linear chirp control. The very good agreement between the results from the developed numerical simulations and the experimental results confirms profound understanding and our ability to control the physical mechanisms involved in the mode-locked pulse evolution and shaping within the ring laser. The repeatability and robustness of the novel laser is verified through couple of successful application examples.

7.2. Discussion of future possibilities

It is a difficult task to encounter all the promising paths that future improvements and applications of a novel potentially compact and efficient ultrafast semiconductor laser could pursue. First, it will be discussed the near future steps towards the finalization of application trends started already in this dissertation. Ideas about the replacement of the bulk optics parts in the prototype dispersion-managed ring laser using some novel promising technologies will be discussed further. The miniaturization and boosting the power in the external amplification part would open endless possibilities of this semiconductor laser system.

The coherent nonlinear spectral broadening via the PCF is a very attractive idea for variety of further experiments and applications. As mentioned in the end of Section 6.1, our experiments imply that a longer piece of the PCF would generate a coherent continuum. An interesting challenge would be to further amplify the generated continuum with an additional SOA after the PCF and recompress it. This could provide significantly shorter pulses with higher peak power than ever possible from just a semiconductor laser. The semiconductor media

gain bandwidth limitation could be overcome. Such a broadband ultrashort pulse source would have lower cost and smaller size than any such source available even in research stage today. In the process of developing this source, the following experiment would be beneficial to perform. It is a feedback adaptive recompression of the continuum generated from the PCF with the semiconductor laser system as the pulse source as illustrated in Figure 59. The feedback loop consists of the computer controlled spatial light modulator (SLM) in the Fourier plane of the compressor and the FROG setup measuring the residual pulse chirp. The pulse chirp is measured via FROG method and sent to a computer. The computer adjusts the liquid crystal cells in the SLM to cancel the residual pulse chirp. The residual pulse chirp is measured again by FROG method and the process continues until the shortest pulse is generated from the continuum.

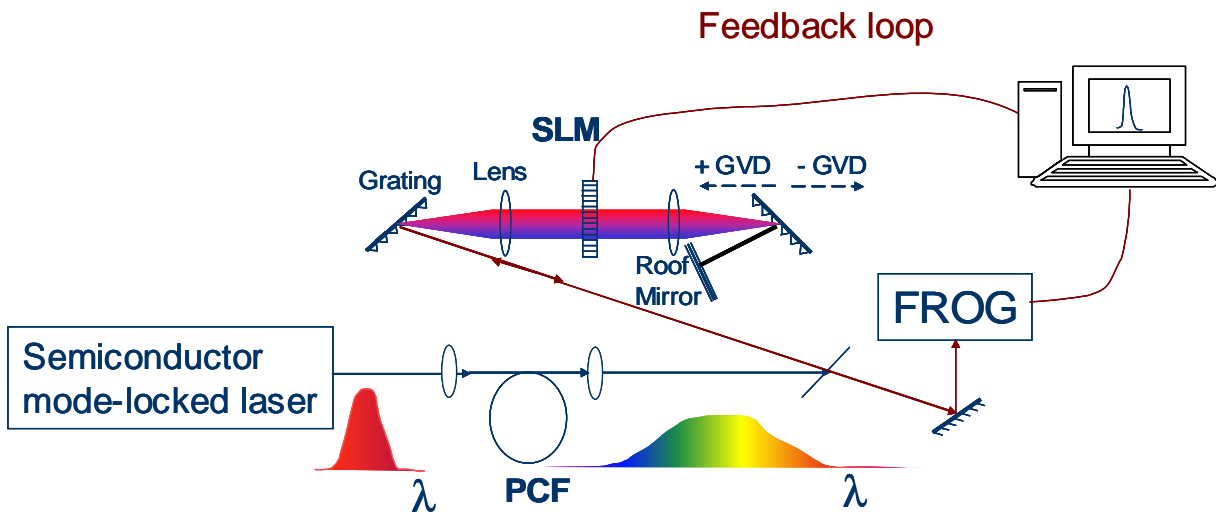


Figure 59: The adaptive feedback pulse recompression from a continuum generated via the PCF and the dispersion-managed mode-locked semiconductor laser system.

This experiment would provide important information about the pulse phase after the nonlinear spectral broadening in the PCF. The pulse phase information is essential for the efficient pulse amplification with an additional SOA and recompression with a compressor without the SLM and the feedback loop. Besides, more of academic importance would be the shortest pulse generation limited by the broad continuum spectrum, which could reach 10 fs duration for 100 nm continuum width around 830 nm. It is more of academic importance since the feedback loop with computer controlled SLM is neither really cost-effective nor compact.

In Section 6.2 the two-photon fluorescence experiment was demonstrated. The blue light from the two-photon fluorescence of the organic dye sample is observed. The organic dye is excited with pulses from the dispersion-managed breathing-mode semiconductor mode-locked laser. Instead of focusing to the uniform sample dye, the laser pulses could be guided to the two-photon microscope. According to students from Prof. Eric van Stryland, their commercial two-photon microscope can resolve a 2-D image using Ti:Sapphire laser attenuated to the average power of 1 mW, with pulse duration of 200 fs, at 80 MHz repetition rate. This is more than three times lower pulse peak power and energy when compared to our semiconductor system generating 185 fs pulses at 323 MHz repetition rate with 14 mW of average power. Thus, if the semiconductor laser pulses would be successfully guided to the commercial two-photon microscope, 2-D imaging could be performed. Output pulses from the dispersion-managed semiconductor laser system could be guided via a fiber to the laboratory with the two-photon microscope. In the external cavity compressor the semiconductor laser output pulse duration could be optimized by prechirping (impressing the optimum amount of the GVD to the pulse) to achieve the shortest duration after the propagation through the fiber, on the input to the microscope. In order to guide as much laser pulse power as possible to the microscope, a careful

coupling of the semiconductor laser pulses to the appropriate fiber should be performed and two-photon fluorescence 2-D imaging should be feasible with use of the dispersion-managed breathing-mode semiconductor mode-locked laser.

Various other pump-probe experiments and other research and commercial applications of the novel developed compact efficient ultrafast pulse source could be pursued depending on the future motivations.

The miniaturization of the laser is a very important future task. The use of bulk optics parts in the current prototype laser cause the unnecessary big cavity size. The biggest issues in the cavity are definitely the bulky dual-grating double-pass compressors. The rest of the optics is not necessary and the SOA and the SA are chip-sizable. Today there are various technologies producing dispersion compensation. One can remark a great progress in the chirped fiber Bragg grating (CFBG) technology, recently reporting tunable CFBG-based devices [86], [87]. An appropriate CFBG device could replace the bulk dual-grating compressor as illustrated in Figure 60. It is essential to match the GVD introduced by two CFBGs, introduce sufficient GVD to the laser cavity, and reduce the losses of the CFBGs and circulators (if the CFBG operates in the reflection mode, one additional circulator per CFBG is needed) in order to achieve the breathing-mode laser operation.

The fiberized dispersion-managed breathing-mode semiconductor mode-locked ring laser employing one CFBG in reflection mode of operation is sketched in Figure 61. The optical isolators prevent the residual light transmitted through the CFBG to be amplified by the SOA. The single-CFBG ring geometry removes the fabrication requirement of the two very well GVD matched CFBGs and reduces the cost. However, the challenge today is to fabricate a CFBG with a sufficiently low loss in reflection and a low transmission for a wide bandwidth. The CFBG are

commercially available today and hopefully the fiberized version of the dispersion-managed breathing-mode semiconductor mode-locked laser will be developed soon.

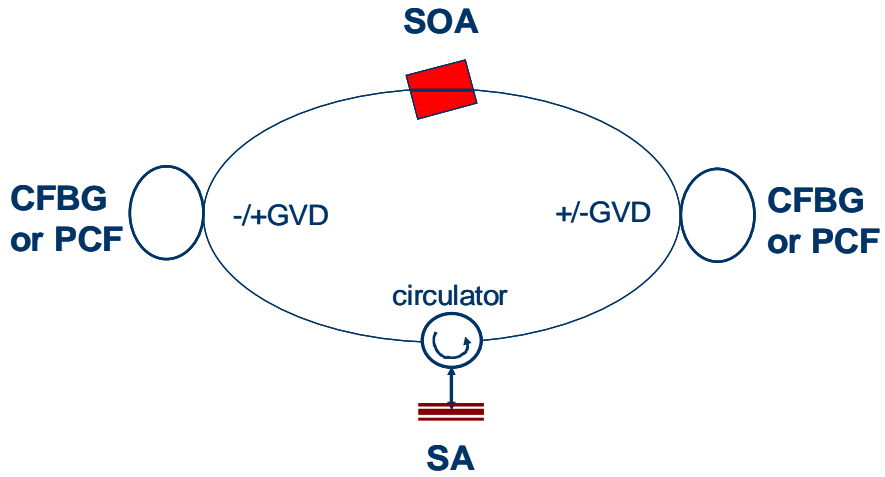


Figure 60: The fiberized version of the dispersion-managed breathing-mode semiconductor mode-locked ring laser. CFBG – chirped fiber Bragg grating; PCF – photonic crystal fiber.

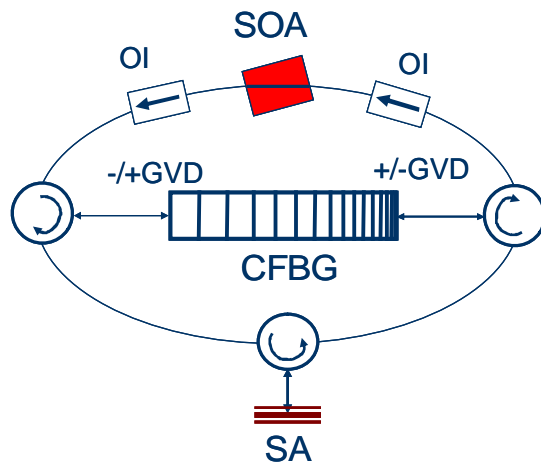


Figure 61: The fiberized version of the dispersion-managed breathing-mode semiconductor mode-locked ring laser employing one CFBG operating in the reflection mode. OI - optical isolator.

The photonic crystal fiber (PCF) technology is entering the field of the dispersion-related applications [88]. The new hot topic in the ultrafast community is the pulse compression with the PCF [89]. One can envision that dual-grating compressors or CFBGs could be replaced with suitably designed PCFs in the dispersion-managed breathing-mode semiconductor mode-locked ring laser as shown in Figure 60. The future will show which technology will win in the game of the compact dispersion-related applications.

On the level of the new promising technologies for future SOAs, our group is intensively working on the GCSEL (grating-coupled surface-emitting semiconductor lasers) and GCSOA (grating-coupled semiconductor optical amplifier) devices [90]. The GCSEL and GCSOA devices have one and two gratings, respectively, etched on the ends of the upper surface. The surface gratings allow coupling of the light in or out with large beam cross-section and low divergence. The large grating emitting area prevents the thermal load. Therefore, much higher power of emitted light is possible than from a typical edge emitting SOA as plotted in Figure 5. The combination of the mode-locked semiconductor laser based on the GCSEL device and amplifier based on GCSOA device shows great potential for the high power ultrafast pulse generation with a low divergence circular beam cross-section.

The amplification of the femtosecond pulses with quantum dot based devices has been intensively studied [91]. The quantum dot based SOA can support wider gain bandwidth when compared to the typical multi quantum well (MQW) SOA. The wide bandwidth gain is crucial for potential broader mode-locked spectrum and shorter pulse generation. Therefore, the very attractive possibility of ultrafast semiconductor mode-locked lasers based on the quantum dot devices is also intensively pursued in our group.

Saturable absorbers incorporating carbon nanotubes (SAINTs) have been studied and recently commercialized. The fiber laser mode locking was reported using SAINTs [92]. The reported SAINT device offers several advantages according to authors, over the MQW SAs such as ultrafast recovery time (<1 ps), polarization-insensitive operation, exceptionally high optical damage threshold, mechanically and environmentally robust, chemical stability, and the ability to operate both in transmission, reflection and bi-directional modes. Moreover, the fabrication cost and complexity of SAINT devices are potentially much lower than that of the conventional MQW-based devices. The property of the device can be controlled simply by varying the thickness and density of the nanotube layer, as well as selecting nanotubes with diameters matching to the operating wavelength. A wideband operation can also be achieved by mixing together nanotubes with different diameters.

So far, we have been discussing the next steps for the already started applications, the promising new technologies to decrease the complexity and size of the ring laser by replacing the bulky grating compressors with the CFBGs or the PCFs, and the novel technologies for the SOA and the SA. This was all mostly about the oscillator cavity. However, one should notice that with smart tricks on the external cavity amplification, the overall laser system performance could be greatly improved.

When compared to the solid-state lasers, the output power of the conventional semiconductor lasers is limited by much shorter upper state lifetime of the semiconductor media. This inherent semiconductor limitation could be overcome using a new concept of extreme chirped pulse amplification (XCPA) developed in our group [93]. The laser output pulse is stretched with a CFBG to much longer duration of ~20 ns than the semiconductor upper state lifetime of ~ 1 ns prior to external cavity amplification. In this case, the external cavity amplifier

SOA senses the propagating pulse almost as it were a continuous wave (CW) light and amplifies it as the CW light. For the CW propagating light the output power is not limited by the upper state lifetime and one can electrically pump the SOA to amplify the light until it is limited by thermal effects. Employing an efficient thermal management scheme, one can achieve much higher average pulse output power than from a conventional pulsed semiconductor laser, followed by compression of the pulses. The same concept of the XCPA could be employed inside the laser cavity. The breathing-mode laser cavity plus the XCPA based external, possibly cascaded amplification unifies the efforts to develop an electrically pumped all-semiconductor laser system capable of sub-ps μ J pulse generation [94]. Such a semiconductor laser system could perform applications such as ultrafast laser precision micromachining, currently feasible only with the Ti:Sapphire and eventually fiber lasers [95].

In the end, this dissertation describes some efforts of the much wider vision. Our vision is by use of the novel technologies to miniaturize the prototype semiconductor laser and amplifier and create extremely compact and highly efficient ultrashort high power optical pulse source. Such a semiconductor system would have endless possibilities and applications.

**APPENDIX A: THE COMPUTER CODE FOR NUMERICAL
SIMULATIONS OF THE UP-CHIRPED DISPERSION-MANAGED
BREATHING-MODE SEMICONDUCTOR RING LASER MODE
LOCKING BUILDUP (Mathcad)**

The simulations of the up-chirped dispersion-managed breathing-mode semiconductor ring laser mode locking build up.

Included effects are the saturable gain with the integrating self phase modulation, negative GVD, the saturable absorption, and positive GVD.

The time and frequency window is an array of m+1 points. $m := 1023$ $t := 0, 1..m$ $v := 0, 1..m$

Number of ring cavity propagations: $n := 600$ $p := 0, 1..n + 1$

Starting field is random numbers representing noise $r_{in,t} := |rnd(1)|$

Parameters for the SOA: inverse saturation energy: $s := 0.0006$
 small signal gain exponential coefficient per meter: $g := 4.8$
 phenomenological integral self-phase modulation coefficient: $nINT := 0.0042$

Parameters for the SA: inverse saturation energy $s1 := 0.03$
 small signal absorption exponential coefficient per meter $L := -3.8$

Introduced GVD: dispersion element 1 (compressor): $k1 := -1.2 \cdot 10^{-3}$
 dispersion element 2 (stretcher): $k2 := 1.2036 \cdot 10^{-3}$

$L1 := 0.2$ Linear cavity loss in %: $1 - L1 = 0.8$

Constant time delay of the pulse per round trip: $td := -0.08 \cdot 10^{-2}$

Modeling of the time filter:

$edgewidth := 100$ $k := 50$ $i := 0, 1..k$ $t1 := m + 1 - edgewidth - k$

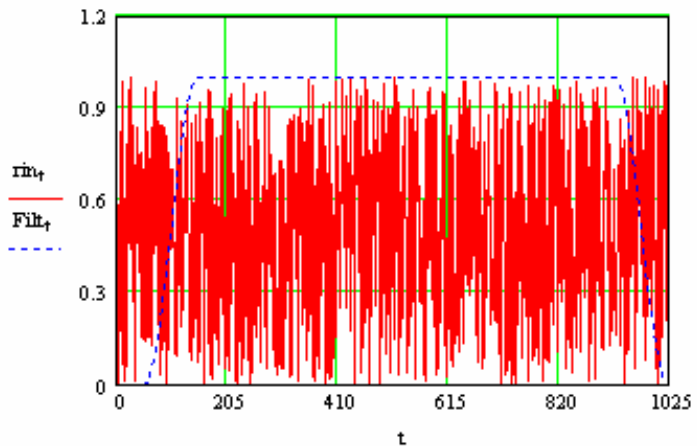
Time filter FWHM: $\tau1 = 874$

$$\theta1_t := \text{if}\left(t > k, \frac{t - k}{edgewidth} \cdot \pi, 0\right) \quad \text{edge1}_t := \frac{1 - \cos(\theta1_t)}{2} \quad \theta2_t := \frac{(t - m + edgewidth)}{edgewidth} \cdot \pi$$

$$\text{edge2}_t := \frac{1 + \cos(\theta2_t)}{2} \quad F1_t := \text{if}[t < (edgewidth + k), \text{edge1}_t, 1]$$

$$F2_t := \text{if}[t > (m + 1 - edgewidth), \text{edge2}_t, 1] \quad \text{Filt}_t := F1_t \cdot F2_t$$

Input to the ring cavity
and temporal filter profile:



Modeling of the frequency filter:

$$\text{edgewidthf} := 500$$

$$v1 := m + 1 - \text{edgewidthf}$$

$$\text{Frequency filter FWHM: } v1 = 524$$

$$\theta1f_v := \frac{v}{\text{edgewidthf}} \cdot \pi \quad \theta2f_v := \frac{(v - m + \text{edgewidthf})}{\text{edgewidthf}} \cdot \pi \quad \text{edge1f}_v := \frac{1 - \cos(\theta1f_v)}{2}$$

$$\text{edge2f}_v := \frac{1 + \cos(\theta2f_v)}{2}$$

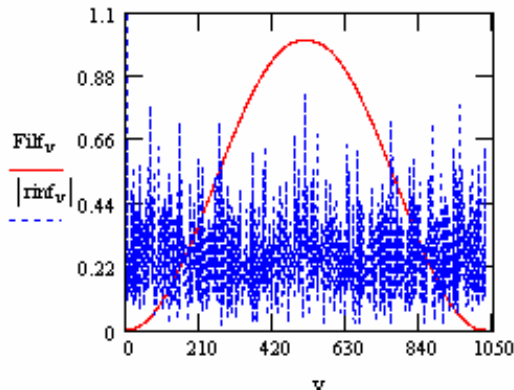
$$F1f_v := \text{if}(v < \text{edgewidthf}, \text{edge1f}_v, 1)$$

$$F2f_v := \text{if}[v > (m + 1 - \text{edgewidthf}), \text{edge2f}_v, 1]$$

$$Filf_v := F1f_v \cdot F2f_v$$

$$\text{Input noise in frequency domain: } rinf := \text{cfft}(rin)$$

Frequency filter profile
and input noise in frequency domain:



Laser cavity round trip loop:

$E :=$ <pre> E <- rin Etot <- E for d ∈ 0,1..m Einc_d <- $(-1)^d \cdot E_d$ Ef <- cfft(Einc) for c ∈ 0,1..m </pre>	Input field is noise. d - index in time domain c - index in frequency domain Shifting the spectrum to the middle and fast Fourier transforming it.
---	---

```

Etotfc ← Efc·Filfc                                Filtering in frequency
for k ∈ 0,1..n
    INT0 ← 0
    for d ∈ 0,1..m
        INTd+1 ← (|Ed|)2 + INTd
        Gd ←  $\sqrt{\frac{s \cdot INT_d}{e^{-\varepsilon} - 1 + e^{s \cdot INT_d}}}$           Saturable gain
        Egsdd ← Ed·Gd·Filtd                               Filtering in time
        Espmdd ← Egsdd·ei·n·INT·INTd           Self-phase modulation
        Espmld ← (-1)d·Espmdd
        Espmf ← cfft(Espml)
        for c ∈ 0,1..m
            Edisp1c ← Espmfc·ei·k1·\left(c-\frac{m+1}{2}\right)^2      Dispersion element 1
            Edilct ← icfft(Edisp1)                                (compressor)
            for d ∈ 0,1..m
                Edisp1tdd ← (-1)d·Edilctd
            INT0 ← 0
            for d ∈ 0,1..m
                INTd+1 ← (|Edisp1tdd|)2 + INTd
                Gsad ←  $\sqrt{\frac{s1 \cdot INT_d}{e^{-L} - 1 + e^{s1 \cdot INT_d}}}$           Saturable absorber
                Esadd ← Edisp1tdd·Gsad·Filtd·L1
                for d ∈ 0,1..m
                    Esacd ← (-1)d·Esadd
                    Esaf ← cfft(Esac)                                Filtering in time plus linear
                                                                loss.
                    for c ∈ 0,1..m
                        Esaf1c ← Filfc·Esafc                  Esaf is E field after saturable
                                                                absorber.
                        Edisp2c ← Esaf1c·ei\left[k2\cdot\left(c-\frac{m+1}{2}\right)^2 + td\cdot\left(c-\frac{m+1}{2}\right)\right]      Esaf is Fourier transform of Esaf.
                                                                Filtering in frequency
                                                                Dispersion element 2
                                                                (stretcher)
                    Edisp21 ← icfft(Edisp2)
                    for d ∈ 0,1..m
                        Edisp2tdd ← (-1)d·Edisp21d

```

$$\left| \begin{array}{l} E \leftarrow Edisp2t \\ Etot \leftarrow \text{augment}(Etot, Espm) \\ Etotf \leftarrow \text{augment}(Etotf, Espmf) \\ \begin{pmatrix} Etot \\ Etotf \end{pmatrix} \end{array} \right.$$

Back to the start of the loop

Attach the last field of the inner loop to the previous matrix started with the input to get the 3D evolution plot.

Output matrix consists of two matrixes - evolution matrix of temporal field and evolution matrix of frequency field.

$E_t := E_0 \quad I_{t,p} := (|E_{t,p}|)^2 \quad$ Output temporal intensity matrix

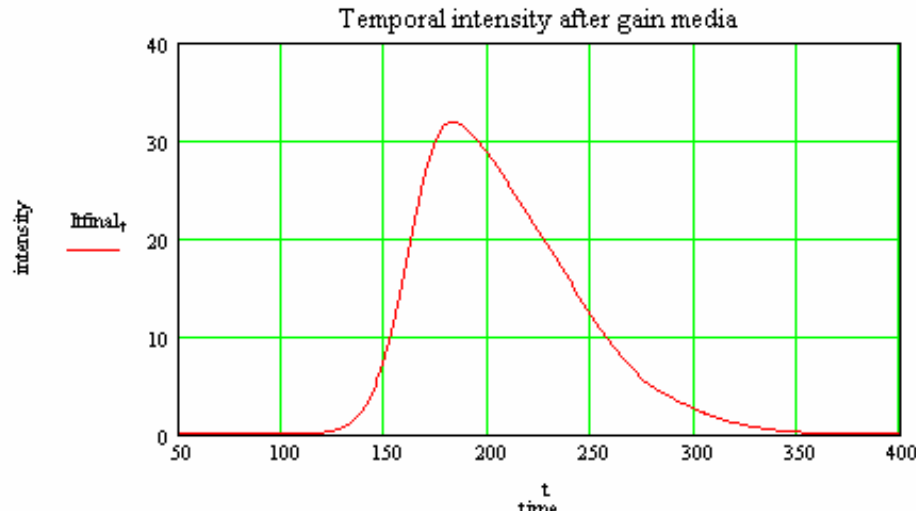
$E_f := E_1 \quad I_{f,v,p} := (|E_{f,v,p}|)^2 \quad$ Output spectral intensity matrix

List of parameters:

SOA	SA	GVD	SPM		Filter widths in frequency and time
$s = 6 \times 10^{-4}$	$s1 = 0.03$	$k1 = -1.2 \times 10^{-3}$	$nINT = 4.2 \times 10^{-3}$	loss	$v1 = 524$
$g = 4.8$	$L = -3.8$	$k2 = 1.2036 \times 10^{-3}$		$t1 = 874$	numb. of prop.
					$n = 600$
					$td = -8 \times 10^{-4}$

The last temporal field after the gain media: the steady state solution

$Itfinal_t := It_{t,n+1}$



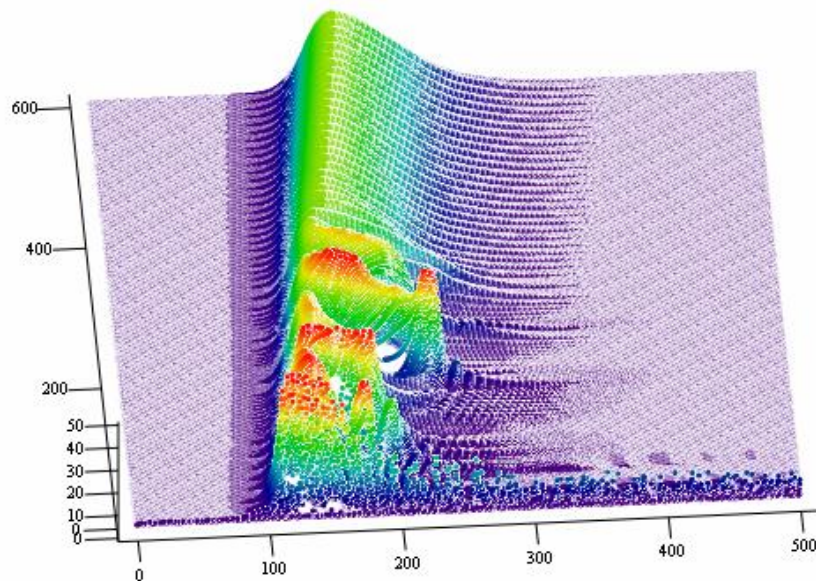
$INT2_0 := 0$

$INT2_{t+1} := INT2_t + Itfinal_t$

Pulse energy:

$$INT2_{1024} = 2.73122 \times 10^3$$

Temporal pulse generation from noise after n ring propagations



It

The last spectral field after the gain media: the steady state solution

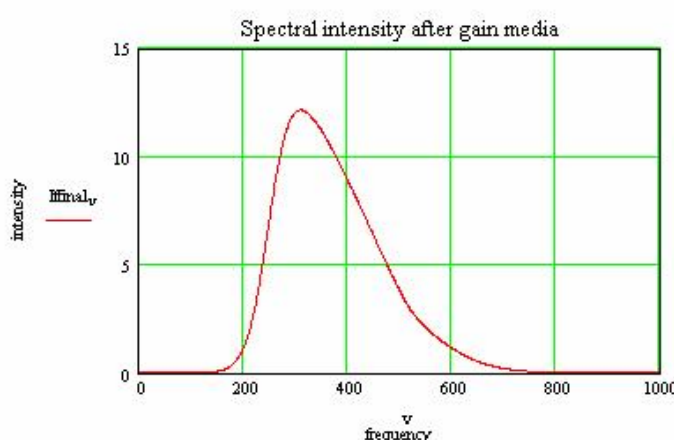
$$Iffinal_v := If_{v,n+1}$$

$$INT1_0 := 0$$

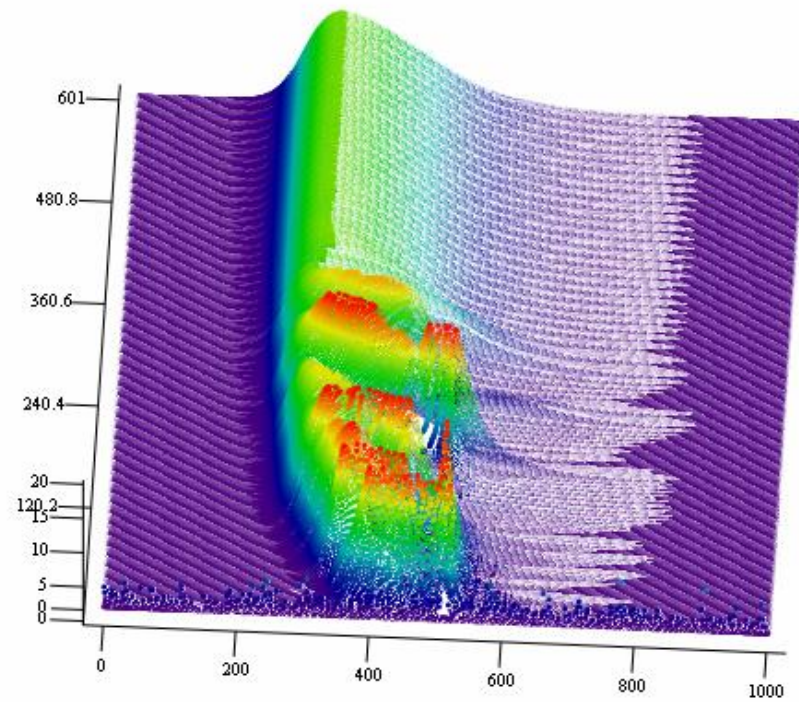
$$INT1_{v+1} := INT1_v + Iffinal_v$$

Pulse energy:

$$INT1_{1024} = 2.73122 \times 10^3$$



Evolution of pulse spectrum after n ring propagations



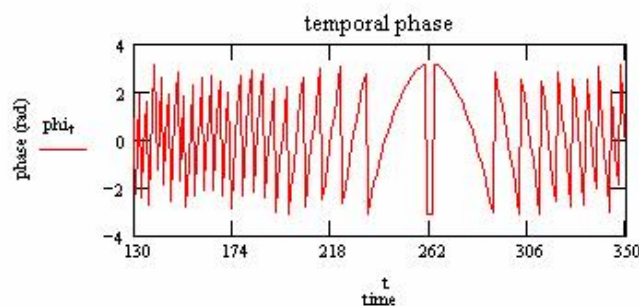
If

Calculation of steady state pulse temporal phase and instantaneous frequency:

$$Efin_t := Et_{t,n+1} \quad Efin_v := Ef_{v,n+1} \quad \phi_t := \text{if}(Efin_t \neq 0, \arg(Efin_t), 0)$$

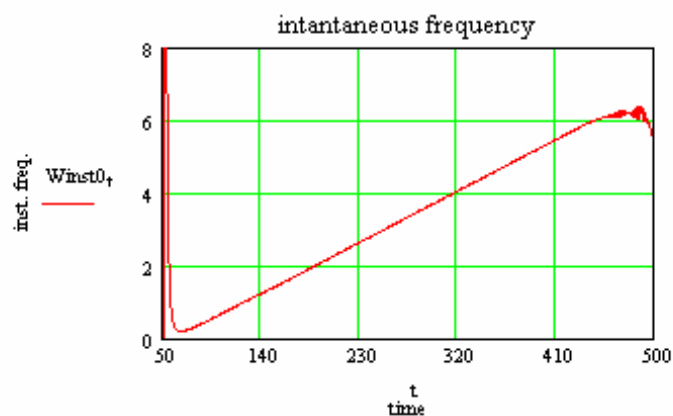
$$Efl_v := i \cdot 2 \cdot \frac{\pi}{m+1} \cdot v \cdot Efin_v$$

$$Et1 := \text{ifft}(Efl) \quad dEt_t := (-1)^t \cdot Et1_t$$



$$W_{inst0_t} := \frac{(Re(Etfin_t) \cdot Im(dEt_t)) - (Re(dEt_t) \cdot Im(Etfin_t))}{(|Etfin_t|)^2}$$

The pulse energy is actually between points 120 and 350 in time and the rest of the time window is noise.



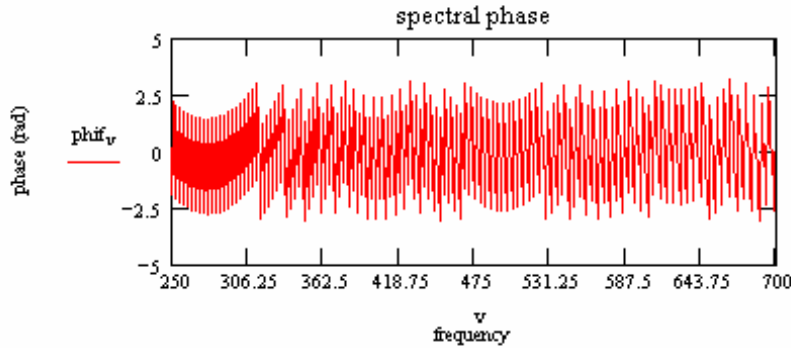
Calculation of steady state pulse spectral phase and group delay:

$$Effin1_v := (-1)^v Effin_v \quad phif_v := \arg(Effin1_v)$$

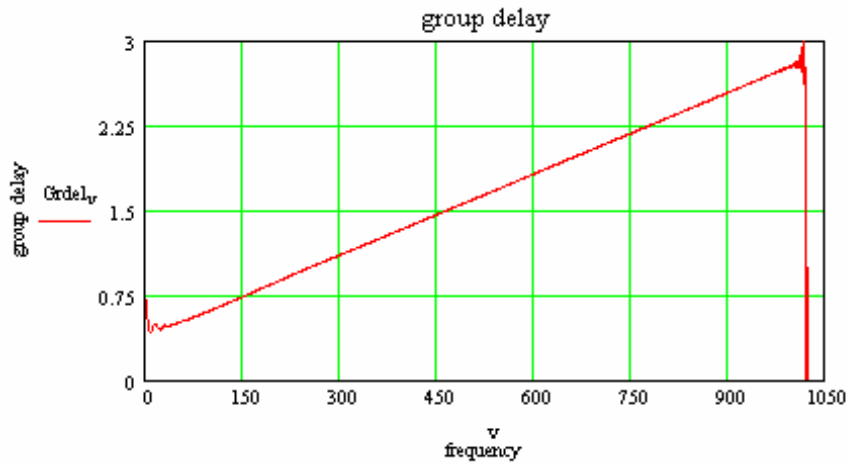
$$Et11_t := -i \cdot 2 \cdot \frac{\pi}{m+1} \cdot t \cdot Etfin_t$$

$$dEf1_t := (-1)^t \cdot Et11_t$$

$$dEf := cfft(dEf1)$$



$$Grdel_v := -\frac{(Re(Effin_v) \cdot Im(dEf_v)) - (Re(dEf_v) \cdot Im(Effin_v))}{(|Effin_v|)^2}$$



**APPENDIX B: THE COMPUTER CODE FOR NUMERICAL
SIMULATIONS OF THE UP-CHIRPED DISPERSION-MANAGED
BREATHING-MODE SEMICONDUCTOR RING LASER LOCKING UP
TO EXTERNALLY INJECTED GAUSSIAN PULSES (Mathcad)**

The program for simulations of the up-chirped dispersion-managed breathing-mode semiconductor mode-locked ring laser locking up to externally injected Gaussian pulses.

Included effects are the saturable gain with the integrating self phase modulation, negative GVD, the saturable absorption, and positive GVD.

The time and frequency window is an array of m+1 points. $m := 1023 \quad t := 0, 1..m \quad v := 0, 1..m$

Number of ring cavity propagations: $n := 100 \quad p := 0, 1..n + 1$

Starting field and intensity

$$\text{Pulse width: } \tau := 50 \quad E_{int} := 1 \cdot \exp \left[-1 \cdot \frac{\left(t - \frac{m+1}{2} \right)^2}{\tau^2} \right] \quad I_{int} := (|E_{int}|)^2$$

Parameters for the SOA: inverse saturation energy: $s := 0.0006$

small signal gain exponential coefficient per meter: $g := 5.4$

phenomenological integral self-phase modulation coefficient: $n_{INT} := 0.0042$

Parameters for the SA: inverse saturation energy $s1 := 0.03$

small signal absorption exponential coefficient per meter $L := -3.8$

Introduced GVD: dispersion element 1 (compressor): $k1 := -1.2 \cdot 10^{-3}$

dispersion element 2 (stretcher): $k2 := 1.2036 \cdot 10^{-3}$

$L1 := 0.2 \quad$ Linear cavity loss in %: $1 - L1 = 0.8$

Constant time delay of the pulse per round trip: $td := -0.08 \cdot 10^{-2}$

Modeling of the time filter:

$\text{edgewidth} := 100 \quad k := 50 \quad i := 0, 1..k \quad t1 := m + 1 - \text{edgewidth} - k$

Time filter FWHM: $t1 = 874$

$$\theta_{1t} := \text{if}\left(t > k, \frac{t-k}{\text{edgewidth}} \cdot \pi, 0\right) \quad \text{edge1}_{1t} := \frac{1 - \cos(\theta_{1t})}{2} \quad \theta_{2t} := \frac{(t - m + \text{edgewidth})}{\text{edgewidth}} \cdot \pi$$

$$\text{edge2}_{2t} := \frac{1 + \cos(\theta_{2t})}{2} \quad F1_t := \text{if}[t < (\text{edgewidth} + k), \text{edge1}_{1t}, 1]$$

$$F2_t := \text{if}[t > (m + 1 - \text{edgewidth}), \text{edge2}_{2t}, 1] \quad \text{Filt}_t := F1_t \cdot F2_t$$

Modeling of the frequency filter:

$$\text{edgewidthf} := 500 \quad v1 := m + 1 - \text{edgewidthf} \quad \text{Frequency filter FWHM: } v1 = 524$$

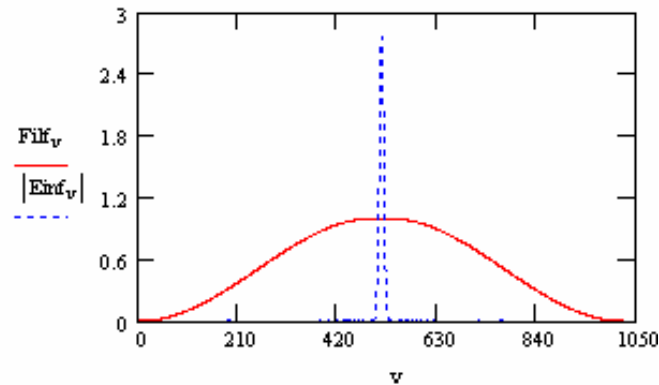
$$\theta1f_v := \frac{v}{\text{edgewidthf}} \cdot \pi \quad \theta2f_v := \frac{(v - m + \text{edgewidthf})}{\text{edgewidthf}} \cdot \pi \quad \text{edge1f}_v := \frac{1 - \cos(\theta1f_v)}{2}$$

$$\text{edge2f}_v := \frac{1 + \cos(\theta2f_v)}{2} \quad F1f_v := \text{if}(v < \text{edgewidthf}, \text{edge1f}_v, 1)$$

$$F2f_v := \text{if}[v > (m + 1 - \text{edgewidthf}), \text{edge2f}_v, 1] \quad Filf_v := F1f_v \cdot F2f_v$$

Input Gaussian in frequency domain: $Ein1_t := (-1)^t \cdot Ein_t$ $Einf := \text{cfft}(Ein1)$

Frequency filter profile
and input Gaussian in frequency domain:



Laser cavity round trip loop:

$E :=$ $E \leftarrow Ein$ $Etot \leftarrow E$ $\text{for } d \in 0, 1..m$ $Einc_d \leftarrow (-1)^d \cdot E_d$ $Ef \leftarrow \text{cfft}(Einc)$ $\text{for } c \in 0, 1..m$ $Etotf_c \leftarrow Ef_c \cdot Filf_c$	Input field is Gaussian. d - index in time domain c - index in frequency domain Shifting the spectrum to the middle and fast Fourier transforming it. Filtering in frequency
--	--

```

for k ∈ 0,1..n
    INT₀ ← 0
    for d ∈ 0,1..m
        INTd+1 ← (|Ed|)2 + INTd
        Gd ←  $\sqrt{\frac{e^{s \cdot INT_d}}{e^{-\varepsilon} - 1 + e^{s \cdot INT_d}}}$ 
        Egsd ← Ed · Gd · Filtd
        Espmd ← Egsd · ei · n · INT · INTd
        Espmld ← (-1)d · Espmd
        Espmf ← cfft(Espml)
        for c ∈ 0,1..m
            Edisp1c ← Espmfc · ei · k1 · (c - m+1/2)2
        Edilct ← icfft(Edisp1)
        for d ∈ 0,1..m
            Edisp1td ← (-1)d · Edilctd
        INT₀ ← 0
        for d ∈ 0,1..m
            INTd+1 ← (|Edisp1td|)2 + INTd
            Gsad ←  $\sqrt{\frac{e^{s_1 \cdot INT_d}}{e^{-L} - 1 + e^{s_1 \cdot INT_d}}}$ 
            Esad ← Edisp1td · Gsad · Filtd · L1
        for d ∈ 0,1..m
            Esacd ← (-1)d · Esadd
        Esaf ← cfft(Esac)
        for c ∈ 0,1..m
            Esafc ← Filfc · Esafc
            Edisp2c ← Esafc · ei · [k2 · (c - m+1/2)2 + td · (c - m+1/2)]
        Edisp21 ← icfft(Edisp2)
        for d ∈ 0,1..m
            Edisp2td ← (-1)d · Edisp21d
        E ← Edisp2t
    
```

Saturable gain
Filtering in time
Self-phase modulation
Espm is E field after saturable gain media and self phase modulation.
Espmf is Fourier transform of Espm.
Dispersion element 1 (compressor)
Saturable absorber
Filtering in time plus linear loss.
Esa is E field after saturable absorber.
Esaf is Fourier transform of Esa
Filtering in frequency
Dispersion element 2 (stretcher)
Back to the start of the loop

$$\begin{cases} \text{Etot} \leftarrow \text{augment}(\text{Etot}, \text{Espm}) \\ \text{Etotf} \leftarrow \text{augment}(\text{Etotf}, \text{Epmf}) \\ \begin{pmatrix} \text{Etot} \\ \text{Etotf} \end{pmatrix} \end{cases}$$

Attach the last field of the inner loop to the previous matrix started with the input to get the 3D evolution plot.

Output matrix consists of two matrixes - evolution matrix of temporal field and evolution matrix of frequency field.

$\text{Et} := \text{E}_0 \quad \text{It}_{t,p} := (|\text{Et}_{t,p}|)^2 \quad \text{Output temporal intensity matrix}$

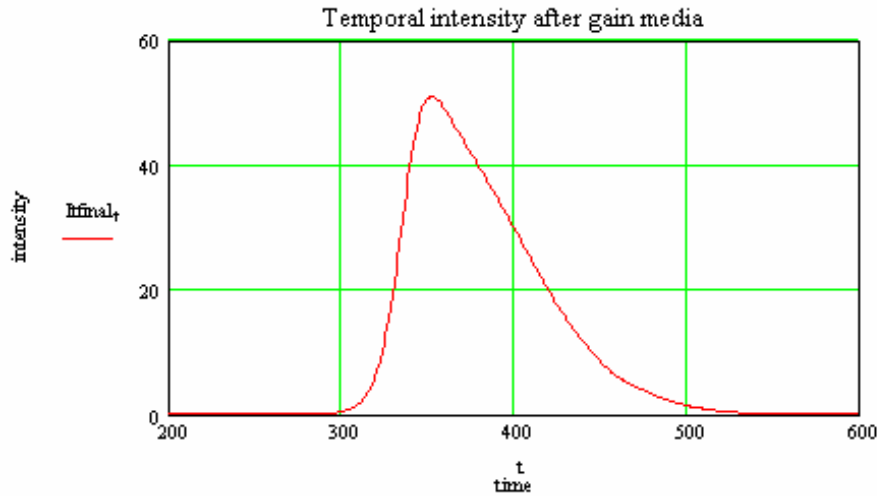
$\text{Ef} := \text{E}_1 \quad \text{If}_{v,p} := (|\text{Ef}_{v,p}|)^2 \quad \text{Output spectral intensity matrix}$

List of parameters:

SOA	SA	GVD	SPM	Pulse width	Filter widths in frequency and time
$s = 6 \times 10^{-4}$	$s_1 = 0.03$	$k_1 = -1.2 \times 10^{-3}$	$n\text{INT} = 4.2 \times 10^{-3}$	$\tau = 50$	$v_1 = 524$ $t_1 = 874$
$g = 5.4$	$L = -3.8$	$k_2 = 1.2036 \times 10^{-3}$			numb. of prop.
					$n = 100$
			loss	$1 - L_1 = 0.8$	$t_d = -8 \times 10^{-4}$

The last temporal field after the gain media: the steady state solution

$\text{Itfinal}_t := \text{It}_{t,n+1}$



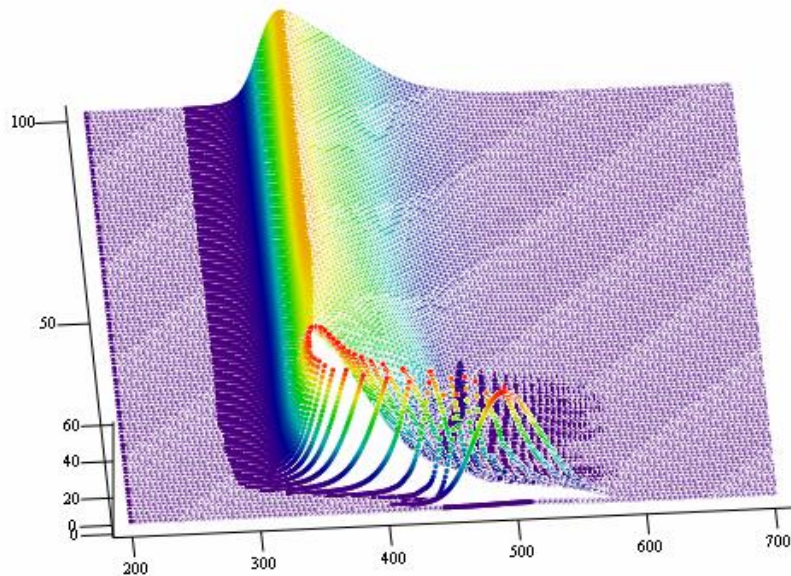
$\text{INT2}_0 := 0$

$\text{INT2}_{t+1} := \text{INT2}_t + \text{Itfinal}_t$

Pulse energy:

$$\text{INT2}_{1024} = 4.18357 \times 10^3$$

Temporal pulse generation from noise after n ring propagations



It

The last spectral field after the gain media: the steady state solution

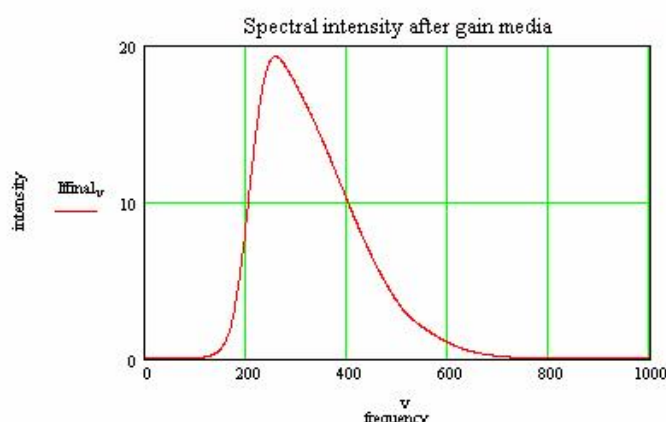
$$Iffinal_v := If_{v,n+1}$$

$$INT1_0 := 0$$

$$INT1_{v+1} := INT1_v + Iffinal_v$$

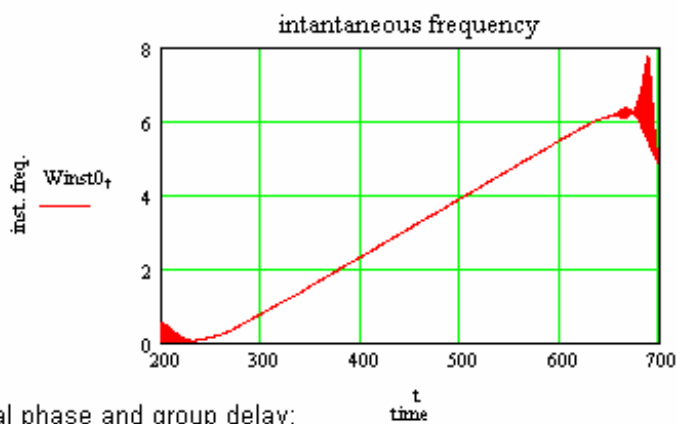
Pulse energy:

$$INT1_{1024} = 4.18357 \times 10^3$$



$$W_{inst0_t} := \frac{(\operatorname{Re}(Etfint_t) \cdot \operatorname{Im}(dEt_t)) - (\operatorname{Re}(dEt_t) \cdot \operatorname{Im}(Etfint_t))}{(|Etfint_t|)^2}$$

The pulse energy is actually between points 300 and 500 in time and the rest of the time window is noise.



Calculation of steady state pulse spectral phase and group delay:

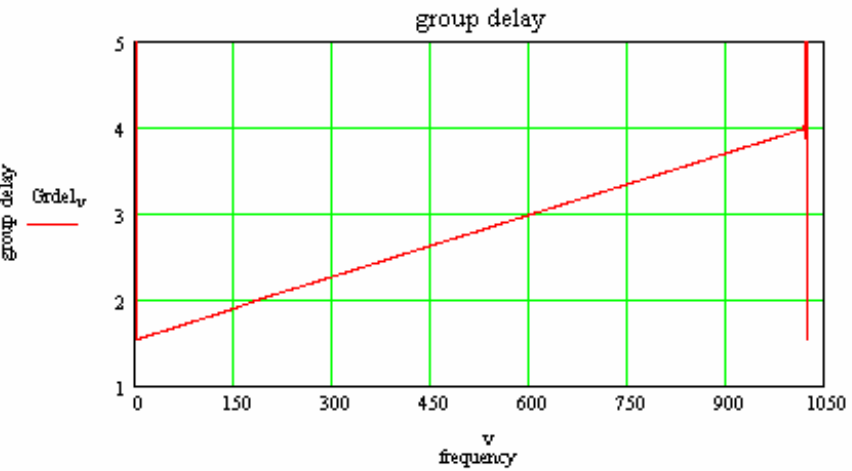
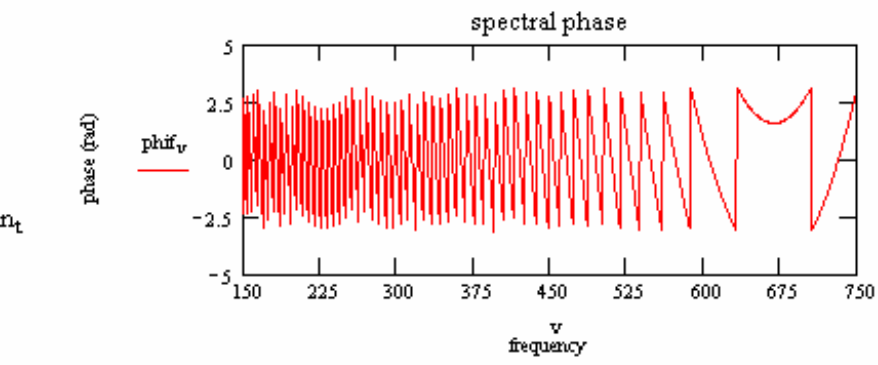
$$Effin1_t := (-1)^t \cdot Effin_t \quad phif_v := \arg(Effin1_v)$$

$$Et11_t := -i \cdot 2 \cdot \frac{\pi}{m+1} \cdot t \cdot Etfint_t$$

$$dEf1_t := (-1)^t \cdot Et11_t$$

$$dEf := cfft(dEf1)$$

$$Grdel_v := -\frac{(\operatorname{Re}(Effin_v) \cdot \operatorname{Im}(dEf_v)) - (\operatorname{Re}(dEf_v) \cdot \operatorname{Im}(Effin_v))}{(|Effin_v|)^2}$$



**APPENDIX C: THE COMPUTER CODE FOR CALCULATION OF THE
PULSE BANDWIDTH-LIMITED AUTOCORRELATION FROM A
MEASURED OPTICAL POWER SPECTRUM (Mathcad)**

The program for calculation of the Fourier transform limited autocorrelation from a measured spectrum.

Putting the experimentally measured spectrum in the middle of the 4096 pixels window.

$$k := 1024, 1025 \dots 1535 \quad \max := 4095 \quad i := 0, 1 \dots \max$$

$\lambda_{range} := 30$ in nm Defining the width of the experimental spectral window.

Reading the measured power spectrum. $I_{lam_i} := 0 \quad E_{lam_i} := 0$

spec := READPRN("D:\Bojan\FROG\FROGdata\185fs111403downch04%\specactAMPnorm.dat")

Calculating the spectrum in frequency units.

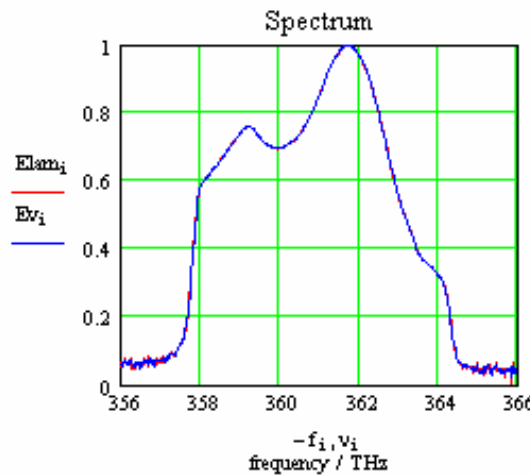
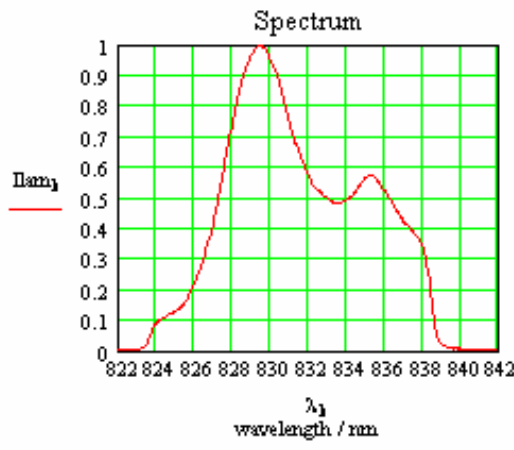
$$I_{lam_k} := spec_{k-1024} \quad E_{lam_k} := \sqrt{|I_{lam_k}|} \quad \lambda_i := 819.059 + \frac{(i - 1024) \cdot \lambda_{range}}{511} \quad f_i := \frac{-3 \cdot 10^8}{\lambda_i \cdot 10^{-9}} \cdot 10^{-12}$$

$$\Delta v := f_{\max} - f_0 \quad \Delta v = 95.09298 \text{ in THz} \quad f_{\max} = -300.19436$$

$$\Delta t := \frac{1}{\Delta v} \quad \Delta t = 0.01052 \quad 1 \text{ step in ps in time window}$$

$$4095 \cdot \Delta t = 43.06312 \quad \text{time window width in ps}$$

$$v_{1,i} := f_0 + \frac{i}{\max} \cdot \Delta v \quad E_{v,i} := \text{linterp}(f, E_{lam}, v_{1,i}) \quad v_i := |v_{1,i}|$$



$$E_t := \text{icfft}(E_v) \quad I_{t,i} := (|E_{t,i}|)^2 \quad \text{It is the Fourier transform of the measured spectrum}$$

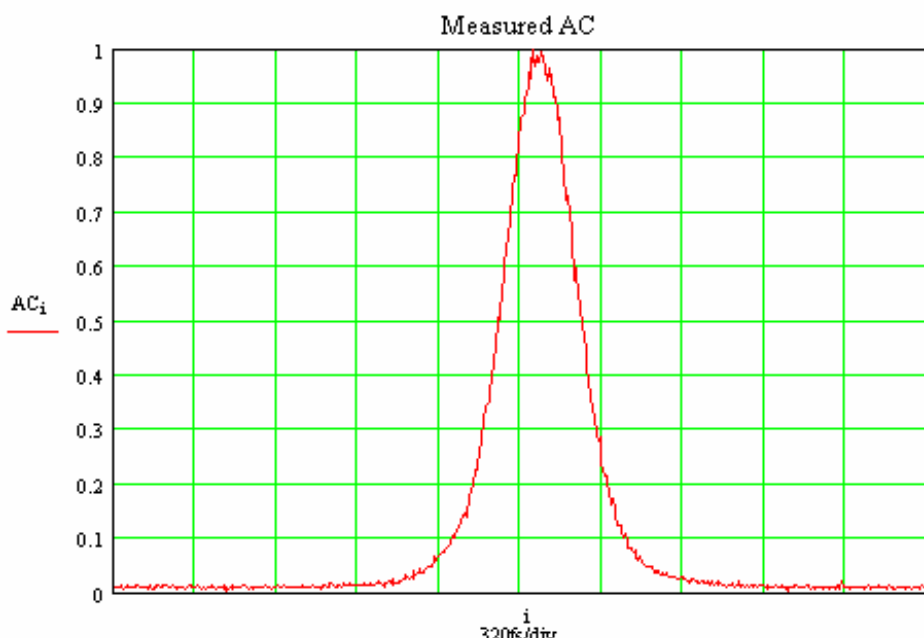
Calculating the bandwidth limited autocorrelation in the frequency domain.

$$I_w := \text{cfft}(I_t) \quad ACw_i := (|I_w_i|)^2 \cdot (-1)^i \quad \text{newAC} := \text{icfft}(ACw)$$

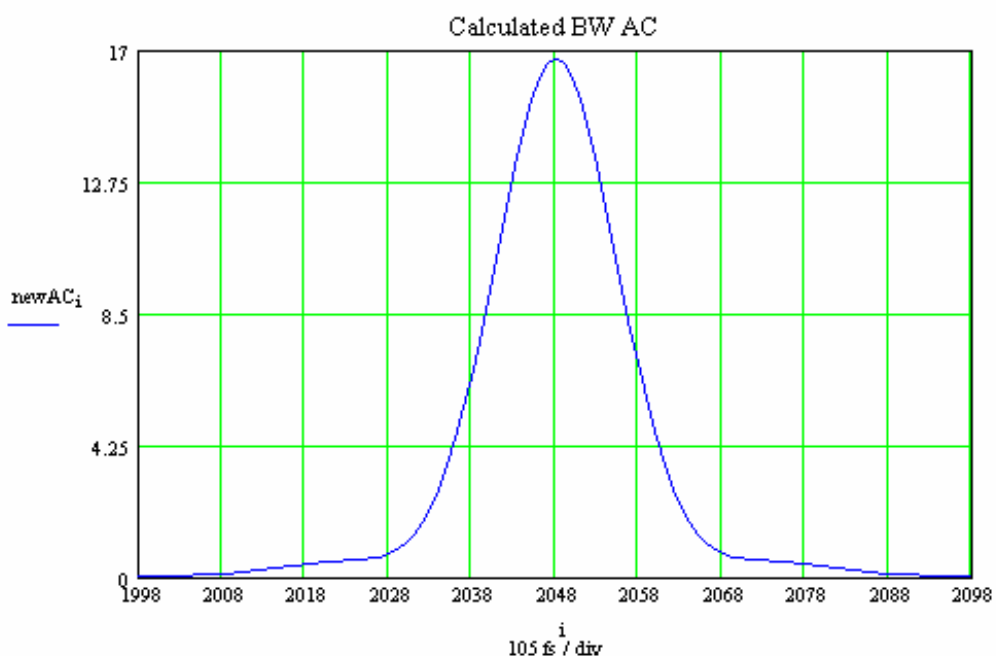
Importing the measured autocorrelation for comparison.

```
AC := READPRN("D:\Bojan\FROG\FROGdata\185fs111403downch04%\autocomp310fsnorm.dat")
```

Input measured autocorrelation



$\Delta t = 0.01052$ 1 step in ps in time window



LIST OF REFERENCES

1. K. L. Hall, E. R. Thoen, and E. P. Ippen, "Nonlinearities in Active Media," in *Nonlinear Optics in Semiconductors II*, E. Garmire and A. Kost, Academic Press, San Diego (1999).
2. Y. Silberberg, P. W. Smith, D. J. Eilenberger, D. A. B. Miller, A. C. Gossard, and W. Wiegmann, "Passive Mode Locking of a Semiconductor Diode Laser," *Opt. Lett.* **9**, 507-509 (1984).
3. C. Schmidt, E. Dietrich, S. Diez, H. J. Ehrke, U. Feiste, L. Kuller, R. Ludvig, and H. G. Weber, "Mode-locked Semiconductor Lasers and Their Applications for Optical Signal Processing," in *Conference on Lasers and Electro-Optics 1999*, paper CThA3.
4. M. Mielke, G. A. Alphonse, and P. J. Delfyett, "168 channels x 6 GHz from a multiwavelength mode-locked semiconductor laser," *IEEE Photon. Technol. Lett.* **15**, 501-503 (2003).
5. K. L. Lee and C. Shu, "Switching-wavelength pulse source constructed from a dispersion-managed SOA fiber ring laser," *IEEE Photon. Technol. Lett.* **15**, 513-515 (2003).
6. B. K. Mathason and P. J. Delfyett, "Pulsed injection locking dynamics of passively mode-locked external-cavity semiconductor laser systems for all-optical clock recovery," *IEEE J. Lightwave Technol.* **18**, 1111-1120 (2000).
7. T. Ohno, K. Sato, T. Shimizu, T. Furuta, and H. Ito, "Recovery of 40 GHz optical clock from 160 Gbit/s data using regeneratively modelocked semiconductor laser," *Electron. Lett.* **39**, 453-455 (2003).
8. C. M. DePriest, T. Yilmaz, A. Braun, J. Abeles, and P. J. Delfyett Jr., "High-Quality Photonic Sampling Streams from a Semiconductor Diode Ring Laser," *IEEE J. Quantum Elect.* **38**, 380-389 (2002).
9. G. A. Keeler, B. E. Nelson, D. Agarwal, C. Debaes, N. C. Helman, A. Bhatnagar, and D. A. B. Miller, "The Benefits of Ultrashort Optical Pulses in Optically Interconnected Systems," *IEEE J. Sel. Top. Quant.* **9**, 477-485 (2003).

10. B. E. Nelson, G. A. Keeler, D. Agarwal, N. C. Helman, and D. A. B. Miller, "Wavelength Division Multiplexed Optical Interconnect Using Short Pulses," *IEEE J. Sel. Top. Quant.* **9**, 486-491 (2003).
11. K. W. Holman, D. J. Jones, J. Ye, and E. P. Ippen, "Orthogonal Control of the Frequency Comb Dynamics of a Mode-locked Laser Diode," *Opt. Lett.* **28**, 2405-2407 (2003).
12. I. Pastirk, J. M. D. Cruz, K. A. Walowicz, V. V. Lozovoy, and M. Dantus, "Selective Two-photon Microscopy with Shaped Femtosecond Pulses," *Opt. Express* **11**, 1695-1701 (2003). <http://www.opticsexpress.org>
13. S. Bourquin, A. D. Aguirre, I. Hartl, P. Hsiung, T. H. Ko, J. G. Fujimoto, T. A. Birks, W. J. Wadsworth, U. Buenting, and D. Kopf, "Ultrahigh Resolution Real Time OCT Imaging Using a Compact Femtosecond Nd:Glass Laser and Nonlinear Fiber," *Opt. Express* **11**, 3290-3297 (2003). <http://www.opticsexpress.org>
14. N. Nishizawa, Y. Chen, P. Hsiung, V. Sharma, T. H. Ko, E. P. Ippen, and J. G. Fujimoto, "Real-time, Ultrahigh Resolution Optical Coherence Tomography at 1.5 mm Using a Femtosecond Fiber Laser Continuum," *Proceedings CD from OSA Topical Meeting Ultrafast Phenomena 2004*, paper WB1.
15. S. Gee, R. Coffie, P. J. Delfyett, G. Alphonse, and J. Connolly, "Intracavity Gain and Absorption Dynamics of Hybrid Modelocked Semiconductor Lasers Using Multiple Quantum Well Saturable Absorbers," *Appl. Phys. Lett.* **71**, 2569-2571 (1997).
16. C. Kurtzke, "Suppression of Fiber Nonlinearities by Appropriate Dispersion Management," *IEEE Photon. Technol. Lett.* **5**, 1250-1253 (1993).
17. T. H. B. Nijhof, N. T. Doran, W. Forysiak, and F. M. Knox, "Stable Soliton-Like Propagation in Dispersion Managed Systems with Net Anomalous, Zero and Normal Dispersion," *Electron. Lett.* **23**, 1726-1727 (1997).
18. Y. Chen and H. A. Haus, "Dispersion-Managed Solitons in the Net Positive Dispersion Regime," *J. Opt. Soc. Am. B* **16**, 24-30 (1999).
19. H. A. Haus and Y. Chen, "Dispersion Managed Solitons as Nonlinear Bloch Waves," *J. Opt. Soc. Am. B* **16**, 889-894 (1999).
20. F. Tauser, F. Adler, and A. Leitenstorfer, "Widely Tunable Sub-30-fs Pulses from a Compact Erbium-doped Fiber Source," *Opt. Lett.* **29**, 516-518 (2004).
21. F. O. Ilday, J. Buckley, L. Kuznetsova, and F. W. Wise, "Generation of 36-femtosecond Pulses from a Ytterbium Fiber Laser," *Opt. Express* **11**, 3550-3554 (2003). <http://www.opticsexpress.org>

22. C. J. S. de Matos and J. R. Taylor, "Multi-kilowatt, All-fiber Integrated Chirped-pulse Amplification System Yielding 40x Pulse Compression Using Air-core Fiber and Conventional Erbium-doped Fiber Amplifier," *Opt. Express* **12**, 405-409 (2004). <http://www.opticsexpress.org>
23. A. Albert, V. Couderc, L. Lefort, and A. Barthelemy, "High-energy Femtosecond Pulses from an Ytterbium-doped Fiber Laser with a New Cavity Design," *IEEE Photon. Technol. Lett.* **16**, 416-418 (2004).
24. Y. Chen, F. X. Kartner, U. Morgner, S. H. Cho, H. A. Haus, E. P. Ippen, and J. G. Fujimoto, "Dispersion-Managed Mode-Locking," *J. Opt. Soc. Am. B* **16**, 1999-2004 (1999).
25. A. Azouz, N. Stelmakh, and J.-M. Lourtioz, "Passive Modelocking of Semiconductor Lasers with Tunable Group Velocity Dispersion Cavity," *Electron. Lett.* **29**, 1437-1438 (1993).
26. P. J. Delfyett, L. T. Florez, N. Stoffel, T. Gmitter, N. C. Andreadakis, Y. Silberberg, J. P. Heritage, and G. A. Alphonse, "High-Power Ultrafast Laser Diodes," *IEEE J. Quantum Elect.* **28**, 2203-2219 (1992).
27. A. Azouz, N. Stelmakh, P. Langlois, J.-M. Lourtioz, and P. Gavrilovic, "Nonlinear Chirp Compensation in High-Power Broad-Spectrum Pulses from Single-Stripe Mode-Locked Laser Diodes," *IEEE J. Sel. Top. Quant.* **1**, 577-582 (1995).
28. J. C. Diels and W. Rudolph, *Ultrafast Laser Pulse Phenomena: Fundamentals, Techniques, and Applications on a Femtosecond Time Scale*, Academic Press, San Diego (1996).
29. G. P. Agrawal and N. A. Olsson, "Self-Phase Modulation and Spectral Broadening of Optical Pulses in Semiconductor Laser Amplifiers," *IEEE J. Quantum Elect.* **25**, 2297-2306 (1989).
30. R. Trebino, *Frequency-resolved Optical Gating: the Measurement of Ultrashort Laser Pulses*, Kluwer Academic Publishers (2000).
31. R. Trebino and D. J. Kane, "Using Phase Retrieval to Measure the Intensity and Phase of Ultrashort Pulses: Frequency-resolved Optical Gating," *J. Opt. Soc. Am. A* **10**, 1101-1111 (1993).
32. J. S. Osinski, Y. Zou, P. Grodzinski, A. Mathur, and P. D. Dapkus, "Low-Threshold-Current-Density 1.5 μm Lasers Using Compressively Strained InGaAsP Quantum Wells," *IEEE Photon. Technol. Lett.* **4**, 10-13 (1992).

33. P. W. Smith, Y. Silberberg, and D. A. B. Miller, "Mode Locking of Semiconductor Diode Lasers Using Saturable Excitonic Nonlinearities," *J. Opt. Soc. Am. B* **2**, 1228-1235 (1985).
34. P. J. Delfyett, A. Dienes, J. P. Heritage, M. Y. Hong, and Y. H. Chang, "Femtosecond Hybrid Mode-Locked Semiconductor Laser and Amplifier Dynamics," *Appl. Phys. B* **58** 183-195 (1994).
35. D. S. Chemla, D. A. B. Miller, P. W. Smith, A. C. Gossard, and W. Wiegmann, "Room Temperature Excitonic Nonlinear Absorption and Refraction in GaAs/AlGaAs Multiple Quantum Well Structures," *IEEE J. Quantum Elect.* **20**, 265-275 (1984).
36. W. H. Knox, R. L. Fork, M. C. Downer, D. A. B. Miller, D. S. Chemla, C. V. Shank, A. C. Gossard, and W. Wiegmann, "Femtosecond Dynamics of Resonantly Excited Excitons in Room-Temperature GaAs Quantum Wells," *Phys. Rev. Lett.* **54**, 1306-1309 (1985).
37. H. A. Haus, "Theory of Mode-locking with a Slow Saturable Absorber," *IEEE J. Quantum Elect.* **11**, 736-746 (1975).
38. J. T. Gopinath, E. R. Thoen, E. M. Koontz, M. E. Grein, L. A. Kolodziejski, E. P. Ippen, and J. P. Donnelly, "Recovery Dynamics in Proton-bombarded Semiconductor Saturable Absorber Mirrors," *Appl. Phys. Lett.* **78**, 3409-3411 (2001).
39. *PhD Thesis* by Dr. Sangyoun Gee, "High Power Ultra Short External Cavity Modelocked Semiconductor Lasers," CREOL, University of Central Florida (2000).
40. T. Okuno, Y. Masumoto, M. Ito, and H. Okamoto, "Large Optical Nonlinearity and Fast Response Time in Low-temperature Grown GaAs/AlAs Multiple Quantum Wells," *Appl. Phys. Lett.* **77**, 58-60 (2000).
41. E. B. Tracy, "Optical Pulse Compression with Diffraction Gratings," *IEEE J. Quantum Elect.* **5**, 454-458 (1969).
42. P. J. Delfyett, "High power ultrafast semiconductor injection diode lasers," in *Compact Sources of Ultrashort Pulses*, I. N. Duling, III, ed., Cambridge University Press (1995).
43. B. Resan, L. Archundia, P. J. Delfyett, and G. Alphonse, "Dispersion-managed Semiconductor Mode-locked Ring Laser," *Opt. Lett.* **28**, 1371-1373 (2003).
44. D. J. Kuizenga and A. E. Siegman, "FM and AM Mode Locking of the Homogeneous Laser - Part I: Theory," *IEEE J. Quantum Elect.* **6**, 694-708 (1970).
45. H. A. Haus, "Theory of Mode-locking with a Slow Saturable Absorber," *IEEE J. Quantum Elect.* **11**, 736-746 (1975).

46. O. E. Martinez, R. L. Fork, and J. P. Gordon, "Theory of Passively Mode-locked Lasers Including Self-phase Modulation and Group-velocity Dispersion," *Opt. Lett.* **9**, 156-158 (1984).
47. O. E. Martinez, R. L. Fork, and J. P. Gordon, "Theory of Passively Mode-locked Lasers for the Case of a Nonlinear Complex-propagation Coefficient," *J. Opt. Soc. Am. B* **2**, 753-760 (1985).
48. H. A. Haus, "Theory of Modelocking of a Laser Diode in an External Resonator," *J. Appl. Phys.* **51**, 4042-4049 (1980).
49. H. A. Haus and Y. Silberberg, "Theory of Mode Locking of a Laser Diode with a Multiple-quantum-well Structure," *J. Opt. Soc. Am. B* **2**, 1237-1243 (1985).
50. R. G. M. P. Koumans and R. Van Roijen, "Theory for Passive Mode-locking in Semiconductor Laser Structures Including the Effects of Self-phase Modulation, Dispersion, and Pulse Collisions," *IEEE J. Quantum Elect.* **32**, 478-492 (1996).
51. J. A. Leegwater, "Theory of Mode-locked Semiconductor Lasers," *J. Quantum Elect.* **32**, 1782-1790 (1996).
52. D. Eliyahu, A. Yariv, and R. A. Salvatore, "Broader, Flatter Optical Spectra of Passively Mode-locked Semiconductor Lasers for a Wavelength-division Multiplexing Source," *Appl. Opt.* **36**, 3430-3434 (1997).
53. M. Y. Hong, Y. H. Chang, A. Dienes, J. P. Heritage, P. J. Delfyett, S. Dijaili, and F. G. Patterson, "Femtosecond Self- and Cross-phase Modulation in Semiconductor Laser Amplifiers," *IEEE J. Sel. Top. Quant.* **2**, 523-539 (1996).
54. A. Bogoni, L. Poti, A. Bizzi, M. Scalfardi, and A. Reale, "Novel Extended SOAs Model for Applications in Very High-speed Systems and Its Experimental Validation," *IEEE Photon. Technol. Lett.* **14**, 905-907 (2002).
55. M. Schell, M. Tsuchiya, and T. Kamiya, "Chirp and Stability of Mode-locked Semiconductor Lasers," *IEEE J. Quantum Elect.* **32**, 1180-1190 (1996).
56. M. Houssin, B. Fermigier, and M. Desaintfuscien, "Simulation of the Frequency Behavior of External-cavity Semiconductor Laser," *IEEE J. Quantum Elect.* **39**, 833-837 (2003).
57. S. Hughes, P. Borri, A. Knorr, F. Romstad, and J. M. Hvam, "Ultrashort Pulse-propagation Effects in a Semiconductor Optical Amplifier: Microscopic Theory and Experiment," *IEEE J. Sel. Top. Quant.* **7**, 694-702 (2001).

58. B. Resan and P. J. Delfyett, Jr., "Dispersion-managed Breathing-mode Semiconductor Mode-locked Ring Laser: Experimental Characterization and Numerical Simulations," *IEEE J. Quantum Elect.* **40**, 214-221 (2004).
59. U. Keller, K. J. Weingarten, F. X. Kartner, D. Kopf, B. Braun, I. D. Jung, R. Fluck, C. Honninger, N. Matuschek, J. Aus der Au, "Semiconductor Saturable Absorber Mirrors (SESAM's) for Femtosecond to Nanosecond Pulse Generation in Solid-state Lasers," *IEEE J. Sel. Top. Quant.* **2**, 435-453 (1996).
60. J. W. Nicholson, J. Jasapara, W. Rudolph, F. G. Omenetto, and A. J. Taylor, "Full-filed Characterization of Femtosecond Pulses by Spectrum and Cross-correlation Measurements," *Opt. Lett.* **24**, 1774-1776 (1999).
61. J. W. Nicholson, M. Mero, J. Jasapara, and W. Rudolph, "Unbalanced Third-order Correlations for Full Characterization of Femtosecond Pulses," *Opt. Lett.* **25**, 1801-1803 (2000).
62. J. W. Nicholson and W. Rudolph, "Noise Sensitivity and Accuracy of Femtosecond Pulse Retrieval by Phase and Intensity from Correlation and Spectrum Only (PICASO)," *J. Opt. Soc. Am. B* **19**, 330-339 (2002).
63. J.-H. Chung and A. M. Weiner, "Ambiguity of Ultrashort Pulse Shapes Retrieved From the Intensity Autocorrelation and the Power Spectrum," *IEEE J. Sel. Top. Quant.* **7**, 656-666 (2001).
64. P. O'Shea, M. Kimmel, X. Gu, and R. Trebino, "Highly Simplified Device for Ultrashort-pulse Measurement," *Opt. Lett.* **26**, 932-934 (2001).
65. J. Zhang, C. Lee, J. Y. Huang, and C. Pan, "Sub Femto-joule Sensitive Single-shot OPA-XFROG and its Application in Study of White-light Supercontinuum Generation," *Opt. Express* **12**, 574-581 (2004). <http://www.opticsexpress.org>
66. J. M. Dudley, L. P. Barry, J. D. Harvey, M. D. Thomson, B. C. Thomsen, P. G. Bollond, and R. Leonhardt, "Complete Characterization of Ultrashort Pulse Source at 1550 nm," *IEEE J. Quantum Elect.* **35**, 441-450 (1999).
67. P. J. Delfyett, H. Shi, S. Gee, I. Nitta, J. C. Connolly, and G. A. Alphonse, "Joint Time-frequency Measurements of Mode-locked Semiconductor Diode Lasers and Dynamics Using Frequency-resolved Optical Gating," *IEEE J. Quantum Elect.* **35**, 487-500 (1999).
68. B. Resan, L. Archundia, and P. J. Delfyett, Jr., "FROG Measured 185 fs Pulses Generated by Down-chirped Dispersion-managed Breathing-mode Semiconductor Laser," *Proceedings CD from OSA Topical Meeting Ultrafast Phenomena 2004*, paper TuE41.

69. R. R. Alfano and S. L. Shapiro, "Observation of Self-phase Modulation and Small-scale Filaments in Crystals and Glasses," *Phys. Rev. Lett.* **24**, 592-594 (1970).
70. R. H. Stolen and C. Lin, "Self-phase-modulation in Silica Fibers," *Phys. Rev. A* **17**, 1448-1453 (1978).
71. R. R. Alfano, *The supercontinuum laser source*, Springer-Verlag (1989).
72. P. S. J. Russell, "Photonic Crystal Fibers," *Science* **299**, 358-362 (2003).
73. J. W. Nicholson, A. K. Abeeluck, C. Headley, M. F. Yan, and C. G. Jorgensen, "Pulsed and Continuous-wave Supercontinuum Generation in Highly Nonlinear, Dispersion-shifted Fibers," *Appl. Phys. B* **77**, 211-218 (2003).
74. J. Zhao, L. Chen, C. Chan, and C. Lin, "Analysis of Performance Optimization in Supercontinuum Sources," *Opt. Lett.* **29**, 489-491 (2004).
75. J. W. Nicholson and M. F. Yan, "Cross-coherence Measurements of Supercontinuum Generated in Highly-nonlinear, Dispersion Shifted Fiber at 1550 nm," *Opt. Express* **12**, 679-688 (2004). <http://www.opticsexpress.org>
76. N. Haverkamp and H. R. Telle, "Complex Intensity Modulation Transfer Function for Supercontinuum Generation in Microstructure Fibers," *Opt. Express* **12**, 582-587 (2004). <http://www.opticsexpress.org>
77. K. M. Hilligsoe, T. V. Andersen, H. N. Paulsen, C. K. Nielsen, K. Molmer, S. Keiding, R. Kristiansen, K. P. Hansen, and J. J. Larsen, "Supercontinuum Generation in a Photonic Crystal Fiber with Two Zero Dispersion Wavelengths," *Opt. Express* **12**, 1045-1054 (2004). <http://www.opticsexpress.org>
78. W. Denk, J. H. Strickler, and W. W. Webb, "Two-photon Laser Scanning Fluorescence Microscopy," *Science* **248**, 73-76 (1990)
79. P. T. C. So, "Prospects of Nonlinear Microscopy in the Next Decade," *Opt. Express* **3**, 312-314 (1998). <http://www.opticsexpress.org>
80. K. D. Belfield, D. J. Hagan, E. W. Van Stryland, K. J. Schafer, and R. A. Negres, "New Two-photon Absorbing Fluorene Derivatives: Synthesis and Nonlinear Optical Characterization," *Org. Lett.* **1**, 1575-1577 (1999).
81. E. P. Ippen and C. V. Shank, "Techniques for Measurements," in *Ultrashort Light Pulses, Picosecond Techniques and Applications*, S. L. Shapiro, Springer, Berlin (1977).
82. K. L. Hall, G. Lenz, A. M. Darwish, and E. P. Ippen, "Subpicosecond Gain and Index Nonlinearities in InGaAsP Diode Lasers," *Optics Comm.* **111**, 589-612 (1994).

83. H. Shi, J. Finlay, G. A. Alphonse, J. C. Connolly, and P. J. Delfyett, "Multiwavelength 10-GHz Picosecond Pulse Generation from a Single-stripe Semiconductor Diode Laser," *IEEE Photon. Technol. Lett.* **9**, 1439-1441 (1997).
84. L. Boivin, M. Wegmueller, M. C. Nuss, and W. H. Knox, "110 Channels x 2.35 Gb/s from a Single Femtosecond Laser," *IEEE Photon. Technol. Lett.* **11**, 466-468 (1999).
85. L. Archundia, B. Resan, and P. J. Delfyett, "Time- and Spectrally-resolved Ultrafast Gain Dynamics of a Semiconductor Optical Amplifier under Phase-correlated Multiwavelength Pulse Amplification," accepted for publication in *Appl. Phys. Lett.* (2004).
86. D. Gauden, E. Goyat, A. Mugnier, P. Lesueur, P. Yvernault, and D. Pureur, "A Tunable Four-channel Fiber Bragg Grating Dispersion Compensator," *IEEE Photon. Technol. Lett.* **15**, 1387-1388 (2003).
87. X. Dong, P. Shum, N. Q. Ngo, C. C. Chan, J. H. Ng, and C. Zhao, "Largely Tunable CFBG-based Dispersion Compensator with Fixed Center Wavelength," *Opt. Express* **11**, 2970-2974 (2003). <http://www.opticsexpress.org>
88. L.-P. Shen, W.-P. Huang, and S.-S. Jian, "Design of Photonic Crystal Fibers for Dispersion-related Applications," *IEEE J. Lightwave Technol.* **21**, 1644-1651 (2003).
89. A. B. Rulkov, S. V. Popov, J. R. Taylor, T. Hansen, and J. Broeng, "Femtosecond Pulse compression around 1 μ m wavelength in air-guiding PCF," in *Proceedings CD from Conference on Lasers and Electro-Optics CLEO 2004*, paper CWK1.
90. K. Kim, S. Lee, O. Smolski, and P. J. Delfyett, Jr., "External-cavity, Actively Mode-locked Grating-coupled Surface-emitting Laser and Amplification Characteristics of a Grating-coupled Semiconductor Optical Amplifier," *Opt. Lett.* **29**, 1273-1275 (2004).
91. E. U. Rafailov, P. Loza-Alvarez, W. Sibbett, G. S. Sokolovskii, D. A. Livshits, A. E. Zhukov, and V. M. Ustinov, "Amplification of Femtosecond Pulses Over by 18 dB in a Quantum-dot Semiconductor Optical Amplifier," *IEEE Photon. Technol. Lett.* **15**, 1023-1025 (2003).
92. S. Y. Set, H. Yaguchi, Y. Tanaka, and M. Jablonski, "Laser Mode Locking Using a Saturable Absorber Incorporating Carbon Nanotubes," *IEEE J. Lightwave Technol.* **22**, 51-56 (2004).
93. K. Kim, S. Lee, and P. J. Delfyett, Jr., "X-CPA (eXtreme Chirped Pulse Amplification): Beyond the Energy Storage Limit of Semiconductor Gain Media," in *Proceedings CD from Conference on Lasers and Electro-Optics CLEO 2004*, paper CTuY2.
94. P. J. Delfyett, Jr., K. Kim, and B. Resan, "Sub-ps μ J Semiconductor Source - Extreme Chirped Pulse Laser and Amplifier (XCPA)," *patent pending*.

95. J. Bovatsek, L. Shah, A. Arai, and Y. Uehara, “Laser Ablation Threshold and Etch Rate Comparison Between the Ultrafast Yb Fiber-based FCPA Laser and a Ti:Sapphire Laser for Various Materials,” in *Proceedings of the SPIE 5th International Symposium on Laser Precision Microfabrication, 2004.*